Optimal Exoskeleton Design and Effective Human-in-the-Loop Control Frameworks for Rehabilitation Robotics

by

Ahmetcan ERDOĞAN

Submitted to the Graduate School of Sabancı University
in partial fulfillment of the requirements for the degree of
Doctor of Philosophy

Sabanci University

August, 2014

OPTIMAL EXOSKELETON DESIGN AND

EFFECTIVE HUMAN-IN-THE-LOOP CONTROL

FRAMEWORKS FOR REHABILITATION ROBOTICS

APPROVED BY:

Assoc. Prof. Dr. Volkan PATOĞLU
(Dissertation Supervisor) .....

Assoc. Prof. Dr. Güllü Kızıltaş ŞENDUR .....

Assoc. Prof. Dr. Esra ERDEM .....

Assoc. Prof. Dr. Kemalettin ERBATUR .....

Asst. Prof. Dr. Evren SAMUR .....

DATE OF APPROVAL: 06/08/2014

To my most beloved family

Optimal Exoskeleton Design and Effective Human-in-the-Loop Control Frameworks for Rehabilitation Robotics

Ahmetcan Erdoğan

ME, PhD Dissertation, 2014

Thesis Supervisor: Assoc. Prof. Volkan Patoğlu

Keywords: Rehabilitation robotics, design optimization, human-in-the-loop control, multi-lateral control, human subject experiments

Abstract

Robotic devices designed for physical rehabilitation attract much attention, since they decrease the cost of repetitive movement therapies, enable quantitative measurement of the patient progress and promise development of more effective rehabilitation protocols. The goal of this dissertation is to provide systematic frameworks for optimal design of rehabilitation robots and effective delivery of therapeutic exercises.

The design framework is built upon identification and categorization of the design requirements, and satisfaction of them through several design stages. In particular, type selection is performed to ensure imperative design requirements of safety, ergonomy and wearability, optimal dimensional synthesis is undertaken to maximize global kinematic and dynamic performance defined over the singularity-free workspace volume, while workspace optimization is performed to utilize maximum singularity-free device workspace computed via Grassmann line theory. Then, human-in-the-loop controllers that ensure coupled stability of the human-robot system are implemented in the robot task space using appropriate error metrics. The design framework is demonstrated on a forearm-wrist exoskeleton, since forearm and wrist rotations are critical in performing activities of daily living and recovery of these joints is essential for achieving functional independence of patients. In particular, a non-symmetric 3$\underline{\text{R}}$PS-$\underline{\text{R}}$ mechanism is selected as the underlying kinematics type and the performance improvements due to workspace and multi-criteria optimizations are experimentally characterized as 27 % larger workspace volume, 32 % higher position control bandwidth and 17 % increase in kinematic

isotropy when compared to a similar device in the literature. The exoskeleton is also shown to feature high passive back-driveability and accurate stiffness rendering capability, even under open-loop impedance control.

Local controllers to accommodate for each stage of rehabilitation therapies are designed for the forearm-wrist exoskeleton in $\mathbf{SO}(3)$: trajectory tracking controllers are designed for early stages of rehabilitation when severely injured patients are kept passive, impedance controllers are designed to render virtual tunnels implementing forbidden regions in the device workspace and allowing for haptic interactions with virtual environments, and passive contour tracking controllers are implemented to allow for rehabilitation exercises that emphasize coordination and synchronization of multi degrees-of-freedom movements, while leaving the exact timing along the desired contour to the patient. These local controllers are incorporated into a multi-lateral shared controller architecture, which allows for patients to train with online virtual dynamic tasks in collaboration with a therapist. Utilizing this control architecture not only enables the shift of control authority of each agent so that therapists can guide or evaluate movements of patients or share the control with them, but also enables the implementation of remote and group therapies, as well as remote assessments.

The proposed control framework to deliver effective robotic therapies can ensure active involvement of patients through online modification of the task parameters, while simultaneously guaranteeing their safety. In particular, utilizing passive velocity field control and extending it with a method for online generation of velocity fields for parametric curves, temporal, spatial and assistive aspects of a desired task can be seamlessly modified online, while ensuring passivity with respect to externally applied forces. Through human subject experiments, this control framework is shown to be effective in delivering evidence-based rehabilitation therapies, providing assistance as-needed, preventing slacking behavior of patients, and delivering repetitive therapies without exact repetition.

Lastly, to guide design of effective rehabilitation treatment protocols, a set of healthy human subject experiments are conducted in order to identify underlying principles of adaptation mechanism of human motor control system. In these catch-trial based experiments, equivalent transfer functions are utilized during execution of rhythmic dynamic tasks. Statistical evidence suggests that i) force feedback is the dominant factor that guides human adaptation while performing fast rhythmic dynamic tasks rather than the visual feedback and ii) as the effort required to perform the task increases, the rate of adaptation decreases; indicating a fundamental trade-off between task performance and level of force feedback provided.

Rehabilitasyon Robotları için Optimal Dış-İskelet ve Etkin İnsan Etkileşimli Kontrol Çatıları Tasarımı

Ahmetcan Erdoğan

ME, Doktora Tezi, 2014

Tez Danışmanı Doç. Dr. Volkan Patoğlu

Anahtar Kelimeler: Rehabilitasyon robotiği, tasarım eniyileştirmesi, insan etkileşimli kontrol , çok-yönlü kontrol, sağlıklı insan deneyleri.

Özet

Fiziksel rehabilitasyon için tasarlanan robotik sistemler, tekrara dayalı hareketlerin maliyetini azaltmaları, hastaların iyileşmelerini nicel ölçütlerle takip edebilmeleri ve daha etkili rehabilitasyon protokollerine olanak sağlamaları açısından büyük ilgi görmektedirler. Bu tez, rehabilitasyon robotlarının optimal tasarımı ve terapi egzersizlerinin etkili uygulanabilmesi için sistematik çatıların tasarımını amaçlamaktadır.

Tasarım çatısı dizayn gereksinimlerinin belirlenmesi, sınıflandırılması ve bu gereksinimlerin tüm dizayn aşamalarında sağlanması üzerine kurulmuştur. Bilhassa; güvenlik, ergonomi ve giyilebilirlik gibi mecburi gereksinimleri korumak için uygun kinematik tip seçimi, tekilliksiz çalışma alanı üzerinde tanımlanan bütünsel kinematik ve dinamik performansın eniyileştirilmesi için optimal boyutsal sentez ve Grassman satır geometrisi ile hesaplanan tekilliksiz en yüksek çalışma alanı hacmi için çalışma alanı optimizasyonu gerçekleştirilmiştir. Sonrasında, robotun çalışma uzayında düzgün tanımlanmış hata metrikleri üzerine kurulmuş ve insan ve robot sisteminin bağlaşık kararlılığını garanti edebilen insan etkileşimli kontrol tasarımı uygulanmıştır. Ön-kol ve bilek hareketleri, günlük hayat faaliyetlerini yerine getirmek için kritik öneme sahiptirler. Sinirbilimsel sakatlıklardan sonra bu eklemlerin iyileşmesi, hastaların fonksiyonel yeterliliklerini kazanmalarında önem teşkil eder. Bu nedenle, bu tezde öne sürülen optimal tasarım çatısı, vaka incelemesi olarak, bir ön-kol ve bilek dış-iskelet yapısı için uygulanmıştır. Bilhassa sistemin kinematik yapısı olarak bakışımsız 3R$\underline{\text{P}}$S-$\underline{\text{R}}$ cihazı seçilmiştir ve cihazın çalışma alanı ve çoklu kriterli optimizasyonlarından sonraki performansının çalışma alanı hacminde 27%, pozisyon kontrolü bant-genişliğinde 32% ve kinematik izotropide 17% olduğu deneysel olarak karakterize edilmiştir.

Rehabilitasyon terapisinde her etapta kullanılmak üzere ön-kol bilek dış-iskeleti için **SO**(3) uzayında yerel kontrolörler tasarlanmıştır: Rahatsızlığın erken safhalarında kritik durumdaki hastalar gezinge izleme kontrolörleri ile pasif olarak hareket ettirilirken, empedans kontrol uygulamaları sanal duvarlar benzetimi ve sanal gerçeklik ortamlarıyla haptik etkileşimi sağlayabilir. Pasif kontur izleme kontrolör tasarımı ise yüksek serbestlik dereceli hareketlerin senkronizasyon ve koordinasyonuna olanak sağlarken, istek konturun takibindeki tempoyu hastanın belirlemesine izin verir. Ayrıca, yerel kontrolörler üzerinden hastanın terapist ile beraber çevirim içi bir şekilde sanal dinamik görevleri yapmasını sağlayan çok yönlü bir kontrol mimarisi uygulanmıştır. Bu mimari sayesinde, denetim yetkisinin değiştirilmesi ile kontrol otoritesi hasta ile terapist arasında ayarlanabilir ve terapist hastanın gelişimini değerlendirebilir. Bu sayede uzaktan ve grup terapileri ile mesafeli değerlendirme çalışmaları olanaklı olur.

Etkin robotik terapilerin tasarımı için, görev parametrelerinin çevirim içi değişimi ile hastanın aktif olarak egzersizlerde katılım sağlayabildiği ve bunu yaparken hastanın güvenliğini garanti edebilen bir kontrol çatısı sunulmuştur. Bilhassa, pasif hız alanı kontrolün parametrik eğriler üzerinden çevirim içi hız alanı oluşumu ile pekiştirilmesiyle, verilen görevin zamansal, uzaysal ve verilen destek değerleri pürüzsüzce değiştirilebilir ve bunları yaparken dış kuvvetlere karşı sistem pasif kalır. Sağlıklı insan deneyleri ile öne sürülen kontrol çatısının gerektiği kadar destek verebildiği, hastaların kaytarmalarını engellediği ve tekrara dayalı hareketleri tekrara düşmeden iletebildiği delile dayalı olarak gösterilmiştir.

Son olarak, uzun süreli iyileşme protokollerinin etkin bir şekilde tasarlanması için, insan motor kontrol sisteminin ritmik dinamik sistemlerle etkileşiminde adaptasyonunu incelemek adına ani değişimli sağlıklı insan deneyleri yürütülmüştür. Eşdeğer transfer fonksiyonlarından da yararlanılarak elde edilen sonuçlar şu istatistik delillere işaret etmektedir: i) kuvvet geri-beslemesi, görsel geri-beslemeye göre ritmik dinamik bir görevde daha baskındır ii) görevi tamamlamak için gereken efor arttıkça, yeni dinamik sisteme adaptasyon yavaşlar ki bu da görev performansı ile sağlanan haptik geri-besleme oranı arasında temel bir ödünleşim olduğunu gösterir. İnsan motor sisteminin öğrenmesinin sinirbilimsel iyileşmeye benzemesi sayesinde, burada bulunan sonuçlar robotik rehabilitasyon protokollerinin tasarımı için kullanılabilir.

Acknowledgements

It is a great pleasure to extend my gratitude to my thesis advisor Assoc. Prof. Dr. Volkan Patoglu for his guidance, understanding and patience. His technical and editorial advice was essential to the completion of this dissertation and has taught me innumerable lessons and insights on the workings of academic research in general.

I would also like to thank my committee members, Assoc. Prof. Dr. Esra Erdem, Assoc. Prof. Dr. Gullu Kiziltas Sendur, Assoc. Prof. Dr. Kemalettin Erbatur, and Assist. Prof. Dr. Evren Samur for their feedbacks and their valuable time serving as my jurors. I would also like to thank our laboratory specialists Ilker Sevgen, Cuneyt Genc, Mehmet Guler and Suleyman Tutkun.

I would like to acknowledge the financial support provided by Tubitak Grants 107M337, 111M186, 111E116, Marie Curie IRG Rehab-DUET and Sabanci University IRP.

I would sincerely like to thank to my laboratory members B. Celebi, G. Coruhlu, A. Ergin, H. Ertas, E. Hocaoglu, M. Sarac, A.C. Satici, M. Sener, N. Tufekciler, M. Yalcin, R. Unal for their pleasant team-work.

Many thanks to Berk Calli, Yasin Yazicioglu, Utku Seven, Ozan Tokatli, Emrah Dincadam and Erdinc Senol and to all mechatronics laboratory members, whom I wish I had the space to acknowledge in person for their great friendship throughout my doctorate. I would also like to devote my sincere thanks to my lifelong friends .

A special thanks to my family. Words cannot express how grateful I am to my mother-in law, father-in-law, brothers-in-law, my sister, my mother, and father for all of the sacrifices that you've made on my behalf. Finally, I would like to thank my wife, Neslihan. She was always there cheering me up and stood by me through the good times and bad.

Contents

List of Figures

List of Tables

LIST OF SYMBOLS AND ABBREVIATIONS

$\mathbf{F}$	Forward kinematics function
α_i	Values of active prismatic joints
$\bar{\Gamma}$	Upper bound on the magnitude of $\mathbf{\Gamma}$
$\bar{\mathbf{I}}$	Dyadic
$\bar{E}$	Energy of the augmented system
$\bar{pz}_i$	Square root of pz_i parameters
$\bar{v}$	Upper bound on the magnitude of ${}^{C}\mathbf{v}^{EE}$
$\dot{\boldsymbol{\chi}}$	End-effector velocity vector
$\boldsymbol{\epsilon}$	Vector of quaternion
$\mathbf{\Gamma}$	Vector from test point to end-effector
$\boldsymbol{\kappa_0}$, $\boldsymbol{\kappa_1}$	Configurations in the workspace that result in the extreme values
$\boldsymbol{\lambda}$	Vector of rotation in angle axis representation
$\boldsymbol{\rho}$	Column vector of design variables
$\boldsymbol{\tau}$	Joint torques
$\boldsymbol{\varepsilon_i}$	Basis vectors for leg frame
χ	Scaling parameter in contour error direction
ϵ_4	Scalar value of quaternion
κ	Curvature of the curve
$\mathbb{R}^3$	Real coordinate space
$\bar{\mathbf{p}}$	Momentum of the augmented system
$\bar{\mathbf{w}}$	Inverse dynamics necessary to follow the desired velocity field
$\dot{\mathbf{Q}}$	Augmented joint coordinates
$\hat{\mathbf{k}}$	Unit tangent vector
$\hat{\mathbf{n}}$	Unit normal vector
$\mathbf{E}$	Vector from closest point to end-effector
$\mathbf{f_i}$	Basis vectors for frame F

$\mathbf{F}_\mathbf{p}^*$, $\mathbf{F}_\mathbf{t}^*$, $\mathbf{F}_\mathbf{e}^*$ External inputs from the masters and the slave

$\mathbf{F}$ End-effector forces

$\mathbf{n_i}$ Basis vectors of Newtonian frame

$\mathbf{P_i}$ Plücker Vectors

$\mathbf{q}$ Joint space configuration vector

$\mathbf{r}^{\mathbf{a\,b}}$ Position vector from point a to b

$\mathbf{S}(\cdot)$ Skew-symmetric operator

$\mathbf{S}^3$ 3-sphere

$\mathbf{u_i}$ Rotational axes of revolute joints

$\mathbf{w_i}$ Basis vectors for frame W

$\mathbf{x}$ Task space configuration vector

$\bar{\mathbf{q}}$,$\dot{\bar{\mathbf{q}}}$ Augmented configurations and velocities

$\bar{\mathrm{M}}$ Inertia matrix of the augmented system

C Coriolis matrix

J Jacobian matrix

$\mathrm{M_{end}}$ Mass matrix evaluated at task space

$\mathrm{M_i}$ Mass matrices of the masters and the slave

M Inertia matrix

R_d, R_e Desired and actual rotation matrices

S'_R Task space rotation matrix

$\mathrm{S_A}$ Diagonal scaling matrix for maximum acceleration

$\mathrm{S_T}$, $\mathrm{S_J}$ Diagonal scaling matrices for end-effector and joint space forces, respectively

V Velocity field

$\mathrm{x_d}$ Parameterized trajectory

ν Self pacing parameter

ω_d Damped natural frequency of the second order dynamic system

ω_n Natural frequency of the second order dynamic system

ϕ Value of active rotational joint at base

Ψ Projection error

ψ_i Euler angles of the end-effector body formed with 'XYZ' sequence

ρ Speed of task execution in PVFC

σ Control gain of the feedback term in PVFC

τ Rate of adaptation

θ Rotation value in angle axis representation

$\underline{\boldsymbol{\Upsilon}}$ Unit Quaternion

$\underline{\boldsymbol{p}}, \underline{\boldsymbol{q}}$ Orientations in quaternion

$\underline{\boldsymbol{Q_d}}, \underline{\boldsymbol{Q_e}}$ Quaternions associated with desired and actual rotations

$\underline{\mathbf{e_O}}$ Position error in quaternions

$\underline{\sigma}, \overline{\sigma}$ Minimum and maximum singular values of the Jacobian or Mass matrix

υ Sigmoid variable that adjusts the relative weighting of each field

ϖ Dominance factor in multilateral control

ς Damping coefficient in PVFC

Ξ_{i_1} Orientation offset at each connection point

ζ Damping ratio of the second order dynamic system

b, k Damping and stiffness between two objects

C_i Gains in multilateral control

C_{mp}, C_{mt}, C_s Impedance controllers without the inertial terms

G Gain of the first mass

K_1, K_2 Control gains of the closest point algorithm

K_P, K_D Position and derivative gain matrices

L_0, L_∞ Initial and steady state frequencies after catch

L_{ij} Physical distance scalar between spherical joints on the end-effector

m_1, m_2 Mass value of first and second objects

M_F Mass of a fictitious flywheel

p_i Translational values of the end-effector in N

px_i, py_i, pz_i Measure numbers of spherical joint centers in N

q_i Rotation value of the revolute joints

r_i Central point of revolute joints

s^a Arrival point on the new curve

s^d Departure point on the initial curve

s_i Central point of spherical joints

U Potential function in PVFC

v Scaling parameter in tangential direction

$V^{\parallel}$ Tangential vector field

$V^{\perp}$ Normal vector field

W Singularity free workspace volume

$x_1, \dot{x}_1$ Position and velocity of the first object

$x_2, \dot{x}_2, \ddot{x}_2$ Position, velocity and acceleration of the second object

Z_d Desired decoupled impedance matrix

Z_p, Z_t, Z_e Impedances of the masters and the slave

ζ Magnitude of the error vector

${}^{\mathrm{A}}\boldsymbol{\omega}^{\mathrm{B}}$ Angular velocity of B with respect to A

${}^{\mathrm{A}}\mathrm{R}^{\mathrm{B}}$ Rotation matrix from body A to body B

${}^{\mathrm{A}}\mathrm{T}^{\mathrm{B}}$ Transformation matrix from body A to body B

(F) Base frame

(N) Newtonian frame

(R), (S), (T) Leg frames

(W) Wrist frame

SO(3) Special orthogonal group

AII	Average isotropy index
EE	End-effector point
GDI	Global dynamic index
NBI	Normal Boundary Intersection
PL	Paralytic limb
TP	Test point
UL	Uninjured limb

Chapter I

1 Introduction

Stroke remains the leading cause of serious, long-term disability in developed countries according to statistics by World Health Organization, which after the initial injury, mainly results in loss of patient's functional independence and significant decrease of their welfare. Although the mechanisms of stroke recovery depend on multiple factors, studies have shown that physical rehabilitation therapy is more effective when exercises are task specific [1], intense [2], repetitive [3], long term [4] and allow for active involvement of patients [5].

The advantages robotic systems bring to the labor-intensive physical rehabilitation are quite obvious; robots excel at repetitive tasks, therefore they can decrease the physical burden of movement therapies for the therapists while enabling intensified, task specific and safe exercises. Not only they can assist, enforce and evaluate the movement of the patients, these systems store quantitative measurements of each exercise that enables the evaluation of short and long term recovery of the patients. Robot-aided rehabilitation enables novel treatment protocols, since new exercises (e.g. simultaneous change of dynamic parameters of the environment during the exercise) can easily be implemented with the use of virtual environments and haptic feedback which would require modification time and discontinuity in traditional therapies. Therefore, it is desired to utilize

safe and versatile robotic rehabilitation systems which can realize reliable, accurate and effective robot-aided physical rehabilitation therapies.

The goal of this dissertation is to provide systematic frameworks for optimal design of rehabilitation robots and effective delivery of therapeutic exercises. More specifically, this works propose a complete rehabilitation system design that includes four major stages: robotic design, human-in-the-loop control, effective delivery of exercises and human motor control analysis for identifying proper treatment protocols.

Optimal Design of Rehabilitation Exoskeleton

The desired outcome of any rehabilitation protocol would be to have patients able to perform activities of daily living (ADL) and using minimal amount of compensatory motions. Forearm and wrist movements are critical in these activities, and after an injury affecting these joints, recovery of the forearm-wrist is essential for achieving functional independence. Therefore, in order to demonstrate the optimal design framework proposed in this thesis, a rehabilitation system for the quite complex forearm and wrist movements is chosen as a case study.

Any rehabilitation robot should be designed such that two imperative criteria, safety and ergonomy of the patients, can be guaranteed even when the device is not active. To that purpose, a parallel exoskeleton 3R$\underline{\text{P}}$S-$\underline{\text{R}}$ is chosen as the kinematic mechanism which enables passive coincidence with human forearm and wrist joint axes. Choice of this particular mechanism increase each of attachment of each patient due to the translational degree of freedom in forearm direction. Since parallel mechanisms are susceptible to major performance changes based on their dimensions, a multi-criteria dimensional optimization is performed. Task-specific per-

formance metrics and optimized parameters are decided based on the control performance and ease of attachment of the device. Chosen global optimization metrics require determination of a singularity-free workspace for all design configurations that is identified through Grassmann line theory, including the asymmetric configurations of this mechanism. Once the optimal dimensions are decided, a workspace optimization scheme is performed that includes the physical limits of the used joints. Implementation and experimental characterization of the device shows that any rehabilitation system could benefit from such a systematic approach.

Human-in-the-Loop Control of Forearm-Wrist Exoskeleton

The second stage consists of design of local and multilateral controllers for the rehabilitation robot. The imperative requirements of rehabilitation therapies should still be maintained; human-in-the-loop controllers that are implemented for each stage of therapies should be safe and consistent with the workspace of the chosen mechanism which lies in Riemannian manifold $\mathbf{SO}(3)$. These local controllers are implemented based on different phases and intensities of a traditional physical therapy. At early stages where patient is not able to exert necessary forces to achieve the given task, patient passive trajectory tracking controllers can be utilized. As the movement capabilities of patient increases, less stricter controllers are desired which can provide assistance to the patient in varying intensities. Impedance controllers can be utilized for administering virtual walls around the forbidden region of operating space and enabling haptic interaction with virtual environments. Once patients are guaranteed to stay inside the safe zones, assistance can be provided around the desired path via a contour tracking controller that emphasizes the synchronization and

coordination of complex movements rather than exact timing along the path. Among the available contour tracking algorithms, passive velocity field control (PVFC) is of particular interest, since this method not only minimizes the contour error but also does so by rendering the close loop system passive with respect to externally applied forces; enhancing safety by limiting the amount of energy that can be released to the operator, especially in case of an unexpected system failure.

Lastly, a multi-lateral control scheme based on local impedance controllers is utilized for tele-rehabilitation, which could shift the dominance of each master over the slave environment, realizing the implementation of remote or group therapy protocols such as Patient (Master 1)-Patient (Master 2)-Dynamic Virtual Environment (Slave) or Patient (Master 1)-Therapist (Master 2)-Dynamic Virtual Environment (Slave). For example, a patient may start as passive while movements are dictated by the therapist and dominance over the task can be shifted to patient over time.

Effective Delivery Framework for Therapeutic Exercises

The third stage considers the design intervention strategies and exercise methods for effective physical therapy. The overall framework should be capable of implementing desired rehabilitation concepts such as being repetitive and intense, while guaranteeing active participation of the patients during tasks based on activities of daily living. While it is desired to apply repetitive exercises, nature of the human motor control system is contradicting with another specification, that is to keep the involvement of the patient high. Humans are fundamentally "lazy", in particular, in a repetitive task human operators tend to slack; if the task is being done just right, effort provided to it lessens with each repetition, while keeping up

with the task requirements. This provides a challenge for the control implementations, since, it becomes crucial to provide repetitive tasks without repeating the same task. To that purpose, a rehabilitation framework is introduced based on local controllers and gets use of the online generation of velocity fields based on parametric curves, which can seamlessly modify the task parameters such as the pace of the contour tracking, shape of the desired contour and the assistance level on the contour error direction while guaranteeing the safety of the patient utilizing passivity with externally applied forces. Each modification can be triggered concurrently or individually according to the supervision of the therapist and/or some performance criteria that is set specifically for each patient.

Effects of Haptic Feedback in Adaptation of Human Motor Control System

In order to get the most out of a therapy session, one should not only implement the evidence-based conventional therapy concepts, but also have some insights on the underlying mechanisms of human motor control and patient recovery. Modeling patient recovery necessitates many large scale clinical trials; however, due to the high cost of clinical studies, such an approach is not feasible. Considering the fact that motor skill learning of healthy volunteers are in many aspects similar to motor re-learning of patients, results from human motor learning experiments have been widely accepted to provide guidelines to design effective rehabilitation protocols. Hence, systematic studies of human motor control and learning can drive development of advanced therapy protocols for robotic therapy.

Therefore, a healthy subject experiments is conducted which highlights characteristics of the human motor control system in a repetitive dynamic

task. In particular, after over-training subjects with nominal system parameters, the system dynamic is unexpectedly changed with catch trials. Through six experiment Seatings, effects of changing different system parameters are analyzed over the steady state error in frequency and adaptation rate. In two of these seatings, use of equivalent systems for impedance and position transfer functions is introduced. Results provides statistically significant evidence that haptic feedback is the dominant factor while performing fast rhythmic dynamic tasks, rather than the vision feedback. In particular, as the effort required to complete the task increases with increased haptic feedback, the rate of adaptation decreases, indicating a trade-off between task performance and the effort required to perform the task.

1.1 Structure of this Dissertation

Chapter 2 describes the analysis of design optimization and implementation of the 3RPS-R exoskeleton robot. After a comparative literature review of forearm and wrist rehabilitation robots, the chapter reviews the kinematic properties of the human joints and summarizes the design requirements for a rehabilitation robot. Following the type selection, kinematic and singularity analyses are performed, while additional details on Grassmann line theory on a asymmetric 3RPS-R mechanism is given in Appendix A. Multi-criteria dimensional optimization is accompanied by physical characterization of the device, including workspace optimization with the physical limits of the joints. Improvements of performance are quantitatively presented.

Chapter 3 details the implementations of local and multi-lateral controllers for 3RPS-R. For local control, error metric is defined to be compat-

ible with the workspace of the mechanism in **SO**(3), while interpolation, trajectory tracking and impedance control implementations are summarized with experimental validations. Afterwards, PVFC is detailed with a sample implementation on 3RPS-R. For use in tele-rehabilitation, a multilateral control scheme is utilized based on local impedance controllers, that enables the change of dominance of the two master sites over the slave environment throughout the exercise.

Chapter 4 defines the control requirements for delivery of effective rehabilitation exercises, and proposes a control framework that can deliver robust, safe and versatile exercises. Online generation of velocity field for parametric curves is introduced to be utilized for the implementation of slacking prevention and assist-as-needed concepts based on local controllers. In particular, this framework provides a systematic approach that enables the seamless online modification of task parameters while guaranteeing the coupled stability of patient and robot system. Following the experimental validation of a) changing the curve of the desired contour, b) regulating the assistance and/or c) pace of the contour tracking, a user study is provided in order to demonstrate learning taking place in the human motor control system with proposed system.

Chapter 5 introduces healthy subject experiments that identify the rate of adaptation of human motor control system on rhythmic dynamic tasks, in particular, non-rigid oscillating tasks without any positional end-point constraints. The chapter includes experimental method definition and results of each seating as well as a general discussion over the statistical analysis performed for each case.

Chapter 6 concludes the thesis by summarizing the contributions and discussing potential future works.

1.2 Contributions of this Dissertation

- Kinematic type of the forearm-wrist rehabilitation robot is chosen such that it enables passive correspondence of robot axes with center of rotation of human forearm-wrist movements. A computationally efficient kinematic model is derived and singularity analysis of asymmetric 3R$\underline{\text{P}}$S-$\underline{\text{R}}$ mechanism is performed for all configurations using Grassmann line geometry so that largest feasible singularity free workspace volume to calculate the global performance metrics is identified. Multi-criteria dimensional optimization is performed in order to increase the performance of the robot by 17% in terms of kinematic isotropy and 32% in term of position control bandwidth when compared to a similar device in the literature. The workspace of the mechanism is also extended by optimizing over singularity free workspace while considering physical joint limits of the device. This optimization results in 27% larger workspace volume, compared to the same similar device. Once the mechanism is implemented, dynamic and kinematic performance are experimentally characterized and successful achievement of design goals is verified.

- Local and multi-lateral controllers are implemented for the forearm-wrist rehabilitation robot with non-symmetric 3R$\underline{\text{P}}$S-$\underline{\text{R}}$ kinematics. To use appropriate error metrics, the local controllers are implemented in the Riemannian manifold $\mathbf{SO}(3)$. In particular, following controllers are implemented to be used in various stages of rehabilitation therapies: a) Trajectory tracking controllers for patient-passive exercises, b) impedance controllers for enabling dynamic interactions with virtual environments and for administration of virtual tunnels, and c) PVFC for delivering contour tracking exercises that enable

safe interactions with the patients throughout the therapy through inherent coupled stability of the user and the robot. Experimental validation of these controllers are also provided for forearm-wrist exoskeleton.

- To enable tele-rehabilitation, a multi-lateral control architecture is implemented based on local impedance controllers, in which different control authority can be assigned between two master sites (e.g., therapist and patient, or patient and patient) over a slave dynamic environment. This multi-lateral control architecture can be used to implement a self-assist protocol where patients can guide themselves to increase use of their paralyzed limb. The architecture can also be used in a remote setup for remote assessments and/or group therapies.

- A safe and versatile rehabilitation control framework is proposed and implemented based on local controllers. Online generation of velocity fields is introduced that enables the seamless online modification of task parameters so that slacking behavior of human motor control system is prevented and assistance is provided as needed. In particular, shape of the desired curve, contour tracking pace and/or assistance in the contour error direction can be modified during task execution, while guaranteeing coupled stability of the patient-in-the-loop system. It is experimentally demonstrated that the proposed framework is capable of rendering repetitive and intense tasks, while keeping the patients involved throughout the exercises and providing assistance as needed.

- Catch trial based healthy human subject experiments are carried out

to identify the change of adaptation rate on a rhythmic dynamic task, in which participants excite virtual second-order systems at their resonance frequency though a haptic interface. With the introduction of equivalent systems for impedance and position transfer functions to these catch trials, it is shown that the haptic feedback is the dominant factor while performing fast rhythmic dynamic tasks, rather than the visual feedback. Furthermore, statistical evidence suggests that as the effort required to complete the task increases, the rate of adaptation decreases, demonstrating the effort versus performance trade-off for rhythmic dynamic tasks with force feedback.

Chapter II

2 Design of the Forearm-Wrist Exoskeleton

In the literature, several robotic devices have been developed to target forearm and wrist rehabilitation exercises. Since they have less mechanical complexity and they are relatively easier to manufacture, end-effector type mechanisms have been quite popular. One such example is Robotherapist upper-extremity rehabilitation support system [6]. This system is capable of controlling all forearm-wrist rotations utilizing ER actuators for safety [7]. Another end-effector based rehabilitation device, haptic knob, has been proposed by Dovat *et al.* to target combined wrist-hand therapy [8]. Haptic knob is a 2 DoF back-driveable mechanism, with one rotation assigned for wrist movements [9]. The system is extended as ReHapticKnob with improved mechanical properties and sensing functionalities [10, 11]. There also exists rehabilitation systems that use commercial haptic devices with modular additions for the wrist rotations. One such approach is to use HapticMaster [12] with additional gimbal modules for wrist rotations as done in [13, 14]. In order to deal with complex wrist motion without introducing design complexity, some researchers have used lockable mechanisms to evaluate different DoF separately [15, 16, 17]. A recent study has utilized a similar structure to implement various operation modes that are interchangeable with wrist exercises and full arm reaching movements [18, 19]. Implementation of end-effector type mech-

anisms in parallel structure is also available; such as the wrist rehabilitation robot with pneumatic muscles [20, 21]. The design uses a Stewart platform to deliver various rehabilitation protocols. Even though mentioned end-effector based rehabilitation systems are practical and simpler to implement, these devices cannot guarantee targeted joint exercises and measurements since the overall motion at the device end effector is a result of movements of the whole limb.

Exoskeleton type rehabilitation devices are relatively more complex but can be effectively used for the implementation and measurement of targeted joint movements. There exist several upper-extremity rehabilitation systems that include forearm-wrist rotations. However, complexity and required DoF increases since these devices are required to match human joint movements and joints of human upper limb, especially the human shoulder is quite complex. As a result, most of the existing exoskeletons omit one of DoF of the forearm-wrist rotation, most commonly the radial/ulnar deviation. Armin, recently commercialized as Armeo Power [22] and IntelliArm [23, 24] are two exoskeleton type full-arm therapy systems, which allow for forearm supination/pronation as well as the flexion/extension of the wrist. These systems are also equipped with a multi-axes force sensors to collect force/torque data during therapy. The wrist extension module of the MIT-Manus system [25, 26] comprises of an actuated cardan joint coupled to a curved slider and allows for 3 degrees of freedom (DoF) forearm-wrist movements. This device is back-driveable and has been used for measurement purposes [27, 28]. In [29], a two finger assist mechanism is built which includes flexion/extension of wrist and pronation/supination of forearm movement in order to include most of the activities of daily living in controlled exercises. These joints are built with two

serial rotations that are orthogonal to each other and actuated with a servo-motor. Another 2 DoF device at wrist is WOTAS [30] which differentiates itself from other designs with a novel actuation for the forearm pronation/-supination motion. In the literature, various actuation methods have been considered. One popular approach is to use pneumatic muscles for actuation such as done in RUPERT [31, 32] or to use cable driven transmission as in Kinarm [33], a planar device capable of flexion/extension exercises for the forearm and wrist. Other devices have been proposed that utilize the advantages of the exoskeleton structure and can validate full forearm-wrist exercises with 3 DoF. W-EXOS [34, 35, 36] and Exorob [37, 38] are two such examples where authors chose to modularly build a full-arm device while wrist module is separately analyzed. Apart from these two structures, a “soft actuated" exoskeleton has been proposed that uses pneumatic muscle actuators (pMA) with antagonistic pairs [39]. The exoskeleton designed in ESA features a large number of passive links such that self alignment can be achieved [40]. Recently, three DoF serial kinematic chain based two robots are built; Ricewrist-S mechanism which uses capstan drive with electrical motors [41] and IIT robot with direct drive [42, 43] for back-driveability. Other arm exoskeletons that have not been implemented as rehabilitation systems but that are capable of all active forearm-wrist rotations include CADEN-7 [44], L-EXOS [45, 46, 47] and MasterArm [48].

All of the devices mentioned above are implemented using serial kinematic structures, since serial robots are advantageous while targeting for a large workspace as demanded by rehabilitation applications. However, mechanisms with closed kinematic chains, or in other words parallel type mechanisms, result in better actuator utilization, and inherently possess compact designs with high stiffness and control bandwidth and low effec-

tive inertia, making it easier for them to satisfy the transparency requirement of force feedback applications. These mechanisms are also advantageous as measurement devices as they do not superimpose positioning errors. The conceptual design of a wearable, force-feedback, forearm-wrist exoskeleton with a 3UPS-S[1] parallel kinematic structure has been proposed in [49]. This mechanism utilizes human forearm-wrist as a part of its kinematic structure and can support 3 DoF rotations of the forearm and wrist, in an ergonomic fashion. In [50], a cable-driven version of this exoskeleton has also been proposed. RiceWrist, the predecessor of RiceWrist-S, this time in parallel kinematics, is another exoskeleton designed to target physical rehabilitation of forearm-wrist motions [51, 52]. Similarly, 3RPS-R kinematic structured device possesses 4 DoF [53], therefore, all wrist and forearm motions can be independently controlled over their rotational axes. RiceWrist has also been extended to deliver full arm rehabilitation therapy, by synchronized control of this device with the MIME system [51].

Designing an exoskeleton mechanism for therapeutic exercises is challenging due to the prerequisite of robot and human joint axes alignment. This requirement necessitates a type selection that is specific for targeted joints, which emphasizes both maximum joint alignment and minimum manual adjustments required to attach each patient. If the chosen kinematic structure of the mechanism is parallel, then an optimal dimensional synthesis would increase device performance extensively, however, possible singular configurations in the reachable workspace of the mechanism should be investigated. In this chapter, design, analysis and implementation of an optimal parallel forearm-wrist exoskeleton is presented. Cho-

[1]Parallel mechanisms are commonly denoted by using symbols U, R, S, and P, which stand for universal, revolute, spherical, and prismatic joint. Symbols corresponding to actuated joints are underlined in this notation.

sen kinematic structure facilitate self-alignment, ease of attachment and wearability thanks to open ring implementation and non-symmetric joint attachments. A minimal singularity-free workspace volume that can accommodate the range of motion of activities of daily living is identified for all design variables, including non-symmetrical configurations of 3R$\underline{P}$S-$\underline{R}$. Afterwards, task dependent global optimization criteria that are chosen based on possible impedance based human in the loop controller performance are maximized using a multi-criteria optimization method. Furthermore, a workspace optimization including the travel limits of the physical parts are performed and final workspace of the mechanism is shown to be singularity-free. Kinematic and dynamic performance of the device is experimentally characterized in order to validate the efficacy of the exoskeleton.

2.1 Kinematics of Human Lower-Arm and the Forearm-Wrist Exoskeleton

The movement of human wrist is quite complex, since it is capable of lateral flexion and extension motions around the radiocarpal and midcarpal joints axes as well as radial/ulnar deviation motions about an axis that passes through the capitate. Moreover, the whole human wrist is capable of supination and pronation movements about the axis of the forearm. Even though the rotation axes of these motions are subject to small variations as the joints move, simplified kinematics of the human elbow and wrist can be quite faithfully modeled as a 3 DoF kinematic chain that allows supination/pronation of the forearm and flexion/extension and radial/ulnar deviation of the wrist joint. In the simplified kinematic model which is generally used in literature, the axes of rotation for these three motions

coincide at a single point on the wrist. Workspace and torque limits of human forearm and wrist are listed in Table 2.1. Although it is desired that final design of the mechanism can cover as much of the range of motion for each DoF as possible; limits obtained from literature [54, 55, 56] for majority of activities of daily living (ADL) movements can be incorporated to any design step as a worst case workspace volume requirement. Minimum range of motion and minimum torque limits for ADL tasks are provided in parenthesis.

Table 2.1: Workspace and Torque Limits of Human Forearm and Wrist

Joint	**Human Isometric Strength [57]**	**Human Joint Workspace Limits**
Forearm Supination/Pronation	9.1 Nm (0.02 Nm)	Supination: 86° (86°) Pronation: 71° (71°)
Wrist Flexion/Extension	19.8 Nm (0.5 Nm)	Flexion: 73° (45°) Extension: 71° (50°)
Wrist Radial/Ulnar Deviation	20.8 Nm (0.5 Nm)	Radial Dev.: 19° (19°) Ulnar Dev.: 40° (40°)

2.2 Design Requirements for Rehabilitation Robot

Following the terminology of Merlet [58], one can categorize the performance requirements of a mechanism into four distinct groups: Imperative requirements that must be satisfied for any design solution, optimal requirements for which a maximal or minimal value of the index is required, primary requirements which take place in the specifications but can be modified to some extend to ensure a design solution, and secondary re-

quirements which do not appear in the specifications but can be utilized to choose between multiple design solutions.

Ensuring the safety and complying with the ergonomic needs of the human operator are the two imperative design requirements for a rehabilitation robot. Safety is typically enforced by i) providing passive back-driveability under the case of power loss, ii) maintaining singularity free and robust workspace and iii) designing controllers with coupled stability integrated with force/torque limits. Ergonomy of the patient necessitates joint alignment of operator and robot, ease of attachment and wearability. In particular, it is desired that chosen mechanism is comfortable to the user, in a sense that it can enforce the targeted exercises as evenly matched as possible to human joint axes. Moreover, due to the difficulties caused by their impairments, cumbersome attachment procedures to the robot should be refrained; it should be easily adjustable to minimize the manual modifications for each patient.

Optimal requirements are the metrics that are desired to remain at the extremum values in order to obtain the maximum performance from the device. Selection of these values are application dependent and will be detailed in Section 2.5. The primary requirement for a rehabilitation robot, on the other hand, may be selected as the volume index [58], which demonstrates the ratio between the workspace volume and the robot volume. A large workspace volume index is also desirable to reduce the collisions of the device with the operator and the environment. The weight of the device is highly dependent on the selection of the actuators, more than the link lengths; hence, there exists some flexibility on deciding the total mass of the kinematic structure. Finally, the secondary requirements for the device include low backlash, low-friction, and low manufacturing costs.

Friction and backlash are required for good control performance and are mainly influenced by the selection of the actuators and the transmission systems.

In the following chapters, imperative requirements are considered at each step, however, type selection has the highest impact on ease of attachment and self-alignment. Passive back-driveability is obtained during the choice of actuator and transmission types at mechanical implementation of the mechanism. Optimal dimensional synthesis is performed not only to optimize performance of the mechanism under impedance-based human-in-the-loop controllers, but also to facilitate wearability of the mechanism utilizing the non-symmetric design and open ring implementation. Selection of Pareto-optimal design configuration is based on wearability, increased workspace volume and some of the secondary requirements. Prior to implementation, reachable workspace of the mechanism including the physical limitations of the chosen parts is optimized.

2.3 Type Selection

A mechanism that is to be used for rehabilitation therapies should at least accommodate imperative performance requirements that are described in Section 2.2. Ergonomy can be increased in many fragments of the design process but mostly determined by the type selection. To elaborate, a kinematic chain that is suitable to serve as an exoskeleton should have rotation axes of its joints coincident with the rotation axes of human forearm and wrist when the device is worn by an operator. Manual adjustment of these link lengths may result in cumbersome installation and calibration processes. To this end, a type selection is performed that can maximize the joint alignment of user and robot and procure minimum manual adjust-

ments for each patient.

Consequently, in order to span an acceptable portion of the natural human wrist and forearm workspace and to ensure alignment of the axes of rotation of human joints with the controlled DoF of the device such that decoupled actuation and measurement of human joint rotations are possible, a closed kinematic chain based mechanisms, namely a 3RPS-R mechanism, is selected as kinematic structures of the exoskeleton. Even though there has been important advances in the type synthesis of these mechanisms [59, 60, 61], design and analysis of many of even the most basic types of these mechanisms are still open research topics [62]. Being compact and allowing for human arm motions without collisions with the device, 3RPS-R mechanism is one of the most suitable candidate to serve as wearable force feedback device. The 3RPS-R mechanism is of hybrid

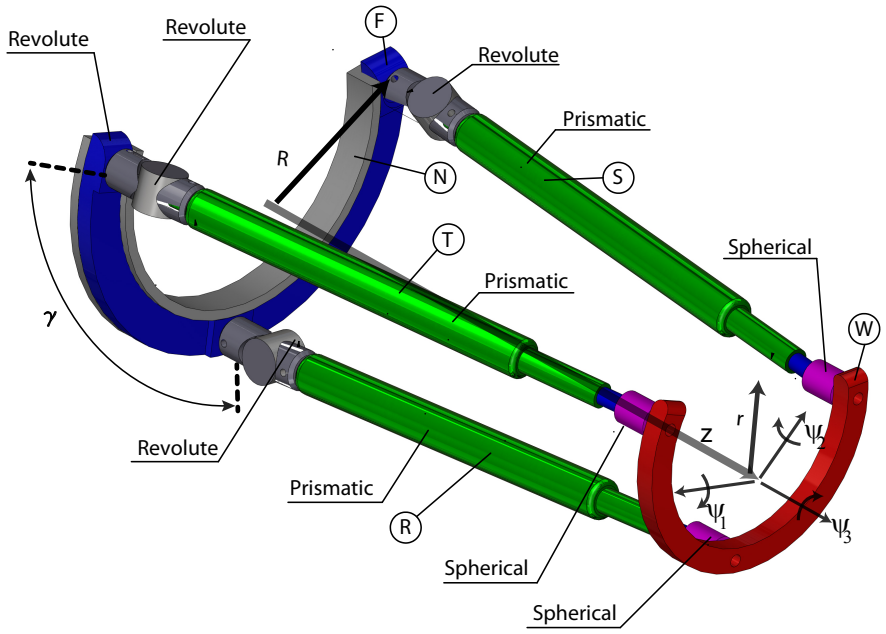

Figure 2.1: Schematic representation of 3RPS-R mechanism in perspective view

kinematic structure and comprises of a 3RPS parallel wrist in series with an actuated revolute (R) joint at the base platform of the wrist, Figure 2.1. The 3RPS platform, first introduced by Lee *et al.* [63], and further analyzed in [64], consists of five bodies: a base platform (F), three extensible links (R), (S), (T), and a moving platform (W). The end-effector held by the operator is rigidly attached to the moving platform W. Extensible links are connected to the base platform via revolute joints whose axes of rotation are oriented along the tangents of (F), while the moving platform is connected to the extensible links by means of spherical joints. The 3RPS-R mechanism is first utilized as an exoskeleton by Gupta *et al.* [65] and adapted as a rehabilitation device in [66].

Translational DoF through forearm rotation axis provided by this particular kinematics can be utilized not only for ease-of-attachment, therefore, eliminating the need of additional adjustments for each user shortening the setup time required to attach the patient to the exoskeleton and allowing more effective time spent on exercises, but also enables the implementation of novel rehabilitation therapy schemes which includes medial forces that pull/push wrist tendons during rotational movement similar to an isotonic exercise [20, 67].

As previously mentioned, performance of parallel structures highly depends on their dimensions, and choice of design variables to maximize the device performance is as important as the chosen optimization criteria. Since translational DoF is employed for ease of attachment and calibration of the device for each patient, radii of base and end-effector platforms would remain as an important performance determinant. For normalized analysis, ratio of radii of these two platforms is chosen as one of the optimization variables. Second design variable is chosen as the joint

placement angle, since this variable not only changes the performance of the mechanism substantially, but also facilitate wearability of robot when base and end-effector platforms are implemented in open ring structures providing wider space to the patient for approaching the robot during attachment. In addition to their obvious effects to kinematic and dynamic performance of exoskeleton, these two variables also play a crucial part in the singularity-free workspace volume of the mechanism.

2.3.1 Configuration Level Kinematic Analysis

3RPS-R mechanism has four DoF, with one independent translational motion in $\mathbf{n_3}$ axis (see Figure 2.2) and three DoF complex rotation in $\mathbb{R}^3$ which resides in a non-Abelian group $\mathbf{SO}(3)$. Any rotation in $\mathbb{R}^3$ can be represented with Euler parameters (unit quaternions) which is the spherical metric on hyper-sphere of dimension three $\mathbf{S}^3$ providing a double cover over $\mathbf{SO}(3)$. This representation results in a more effective handling of composition of rotations, in addition to relatively better numerical stability.

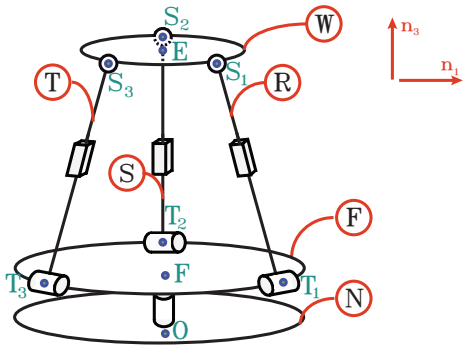

Figure 2.2: Schematic representation of the 3RPS-R mechanism with significant points

In this study, the unit quaternions (Euler parameters) are represented

as

$$\underline{\boldsymbol{\Upsilon}} = [\epsilon_4, \boldsymbol{\epsilon}^T]^T \tag{2.1}$$

where $\epsilon_4 \in \mathbb{R}$ and $\boldsymbol{\epsilon} = \epsilon_1 \, \mathbf{n_1} + \epsilon_2 \, \mathbf{n_2} + \epsilon_3 \, \mathbf{n_3} \in \mathbb{R}^3$ with $\mathbf{n_i}$ representing the basis vectors for Newtonian frame. These parameters can be calculated directly from angle-axis representation (rotating the body about an axis $\boldsymbol{\lambda} \in \mathbb{R}^3$ by an angle of rotation $\theta \in (-\pi, \pi)$) using

$$\epsilon_4 = \cos\left(\frac{\theta}{2}\right), \qquad \boldsymbol{\epsilon} = \sin\left(\frac{\theta}{2}\right)\boldsymbol{\lambda} \tag{2.2}$$

Regardless of the representation of the end-effector rotation, the mapping between actuator (joint) position/orientation values and end-effector configuration is required, namely, the forward kinematics of the device in position level:

$$\mathbf{x} = \Gamma(\mathbf{q}) \tag{2.3}$$

where $\mathbf{x} = [p_3; [\epsilon_4, \boldsymbol{\epsilon}^T]^T]$ is the task-space parameters. p_3 is translation of the end-effector with respect to base with $\mathbf{r^{OE}} = p_1 \, \mathbf{n_1} + p_2 \, \mathbf{n_2} + p_3 \, \mathbf{n_3}$. In particular, $\mathbf{r^{OE}}$ defines the vector from point O, which is a fixed point in Newtonian base, to the point E, the center of end-effector body. Moreover, $\mathbf{q}$ defines the active joint variables $\mathbf{q} = [\alpha_1, \alpha_2, \alpha_3, \phi]^T$ with α_i representing the prismatic joint values at each leg and ϕ the rotation value between base and parallel structure. Basically, with four active joint variables, four DoF at end-effector can be controlled; one of them being the translational movement p_3 and the others represent the orientation of the end-effector. Note that unit quaternions includes the unity constraint equation; $\epsilon_4^2 + \|\boldsymbol{\epsilon}\|_2^2 = 1$. Remaining parameters of end-effector configuration and passive joint values are dependent coordinates which can be calculated through

constraint equations of the device:

$$\mathbf{0_i} = \mathbf{r}^{\mathbf{O\,E}} + \mathbf{r}^{\mathbf{E\,S_i}} - \mathbf{r}^{\mathbf{O\,S_i}} \tag{2.4}$$

where $\mathbf{r}^{\mathbf{E\,S_i}}$ are the vectors from the end-effector center to the spherical joint coordinates for each leg yielding nine scalar equations. These loop equations would naturally sum up to zero vectors since a closed contour is tracked. Although many alternative loops may be chosen for the constraint equation, appropriate designation of these equations and generalized coordinates of the mechanism may simplify forward kinematics extensively. For that purpose, this study follow the methodology similar to the work of Gallardo *et al.* [68], where nine constraint equations are selected such that six measure numbers of $\mathbf{r}^{\mathbf{O\,S_i}}$ vectors can be eliminated. Afterwards, remaining three measure numbers are solved with numerical methods on-line, resulting in more efficient computations with smaller matrix multiplications for calculating the gradient of these zero vectors.

This elimination method eventually yields the relationship between active joint variables $\mathbf{q}$ and spherical joint centers $[px_i, py_i, pz_i]$ and only focuses on the parallel part of the 3R$\underline{\text{P}}$S-$\underline{\text{R}}$ robot with the (F) frame being the base for the analysis. Afterwards, computations between spherical joint centers and end effector coordinates $\mathbf{x}$ as well as the solution of the serial part which consists of a simple rotation ϕ between bodies (N) and (F) and can be performed trivially.

Forward Kinematics with Elimination Method

In particular, modified forward kinematic problem becomes the solution of the generalized coordinates ζ:

$$\zeta = [px_1, py_1, pz_1, px_2, py_2, pz_2, px_3, py_3, pz_3] \tag{2.5}$$

where vectors to each spherical joint centers from origin are defined for $i = 1, 2, 3$:

$$\mathbf{r}^{\mathbf{O\,S_i}} = px_i\,\mathbf{n_1} + py_i\,\mathbf{n_2} + pz_i\,\mathbf{n_3} \tag{2.6}$$

Modified constraint equations used for kinematic solution of the parallel part can be verbally summarized as :

1. Scalar product of the vector on each prismatic link and the rotation axis of the corresponding revolute joint is zero. In other words, revolute joint constrains the motion on its rotation axis for each limb.
2. Length of the vector on the prismatic link is equal to the generalized coordinates α_i for each limb.
3. Length between each spherical joint location is known since the shape and size of the end-effector are determined.

and in mathematical formulation :

1. $\mathbf{r}^{\mathbf{T_i\,S_i}} \cdot \mathbf{u_i} = 0$
2. $\mathbf{r}^{\mathbf{T_i\,S_i}} \cdot \mathbf{r}^{\mathbf{T_i\,S_i}} = (\alpha_i)^2$
3. $\mathbf{r}^{\mathbf{S_i\,S_j}} \cdot \mathbf{r}^{\mathbf{S_i\,S_j}} = L_{ij}$

where $j = 1, 2, 3$ while $j \neq i$, and L_{ij} denotes the physical distance scalar between spherical joints on the end-effector body, $\mathbf{r}^{\mathbf{S_i\,S_j}} = \mathbf{r}^{\mathbf{O\,S_j}} - \mathbf{r}^{\mathbf{O\,S_i}}$ that

can be simply measured from the manufactured part and $\mathbf{r}^{\mathbf{T_i\,S_i}}$ denotes the vector from the revolute joint to the spherical joints.

This intuitive choice of the constraint equations greatly simplifies the solution of the measure values of $\mathbf{r}^{\mathbf{O\,S_i}}$ vectors with respect to active generalized coordinates. First constraint equation $\mathbf{r}^{\mathbf{T_i\,S_i}}\,\mathbf{u_i} = 0$ yields three linear equations in py_i which can be used to eliminate these variables. Second constraint set, $\mathbf{r}^{\mathbf{T_i\,S_i}}\,\mathbf{r}^{\mathbf{T_i\,S_i}} = \alpha_i^2$, can be used to form the three equation sets which yields three quadratic functions.

$$0 = \mathbf{f}(px_i^2, pz_i^2, \alpha_i^2) \tag{2.7}$$

Intermediate parameters can be defined $\bar{pz}_i^2 = pz_i$ which are linear in Eqn. (2.7) and can be solved analytically. Substitution of these solutions to third constraint equation will yield three non-linear equations for each leg. With these three non-linear equations, solution for the position forward kinematic mapping are obtained. In other words, given actuator values $\alpha_1, \alpha_2, \alpha_3$, using a numerical method, px_i generalized coordinates are calculated on-line, where the remaining measure numbers of $\mathbf{r}^{\mathbf{O\,S_i}}$ vectors are already solved linearly.

Once the position of the spherical joint centers are located, determining the configuration of the end-effector body is straightforward. Orientation of a body with respect to a reference frame can be determined if two vectors on the body can be explicitly defined with respect to both frames; body and reference. Let $\mathbf{p}$ and $\mathbf{q}$ vectors be formed such as $\mathbf{p} = \mathbf{r}^{\mathbf{O\,S_1}} - \mathbf{r}^{\mathbf{O\,S_2}}$ and $\mathbf{q} = \mathbf{r}^{\mathbf{O\,S_3}} - \mathbf{r}^{\mathbf{O\,S_2}}$, while $\mathbf{k}$ represents the cross product of these two vectors $\mathbf{k} = \mathbf{p} \times \mathbf{q}$; rotation matrix of the first frame with respect to the second

frame can be formed using [69] :

$$ {}^{F}R_{ij}^{W} = \mathbf{f_i} \, , \, \bar{\mathbf{I}} \, , \, \mathbf{w_j} \tag{2.8} $$

where $\mathbf{f_i}$ and $\mathbf{w_j}$, represents the basis vectors for frame (F) and end-effector reference frame (W), respectively. Here $\bar{\mathbf{I}}$ is a dyadic formed with the formula:

$$ \bar{\mathbf{I}} = \frac{\mathbf{p} \times (\mathbf{qk}) + \mathbf{q} \times (\mathbf{kp}) + \mathbf{k} \times (\mathbf{pq})}{\mathbf{k} \cdot \mathbf{k}} \tag{2.9} $$

Therefore, using spherical joint locations, orientation of the end-effector with respect to the base of the parallel mechanism, (F), is acquired, ${}^{F}R^{E}$. Exploiting the hybrid structure of the mechanism, orientation of the end-effector with respect to Newtonian frame can easily be obtained by ${}^{N}R^{E} = {}^{N}R^{F} \, {}^{F}R^{E}$, where

$$ {}^{N}R^{F} = \begin{bmatrix} cos(\phi) & sin(\phi) & 0 \\ -sin(\phi) & cos(\phi) & 0 \\ 0 & 0 & 1 \end{bmatrix} \tag{2.10} $$

Inverse Kinematics with Elimination Method

Position level inverse kinematics can be required in control algorithms and is defined by the necessary displacement in joint space variables (α_1, α_2, α_3 and ϕ) when the end-effector configuration is provided. Inverse kinematics solutions of the parallel mechanisms are generally easier, and in most cases analytic derivation is possible. Similar to forward kinematics, it is possible to handle the serial part of the 3RPS-R mechanism separately from the parallel structure 3RPS without loss of generality. Starting from the parallel structure and ignoring the rotational DoF. ϕ, the three vector loops in Eqn. (2.4) are used to form nine scaler equations that are linear

in the nine measure numbers of the three $\mathbf{r}^{\mathbf{O}\,\mathbf{S_i}}$ vectors. Afterwards, second constrained function is used to define the quadratic mapping between prismatic joint lengths α_i and these generalized coordinates. In order to complete the inverse kinematics of the hybrid 3R$\underline{\text{P}}$S-$\underline{\text{R}}$ mechanism, mapping between independent and dependent end-effector values should also be acquired. Dependent coordinates are the translation of the end-effector in $\mathbf{n_1}$ and $\mathbf{n_2}$ and the rotation around third principle axis. Finding the p_1 and p_2 measure numbers are trivial using the first constraint equations in which these translational coordinates are linear.

Regarding the last dependent coordinate, it should be emphasized that due to the complex movement of the parallel part and representation of the end-effector rotations, active simple rotation on the serial part ϕ cannot simply be designated as the rotation of the end-effector in third principal axis with respect to Newtonian frame. In particular, end-effector rotation around the third principle axis $\boldsymbol{n_3}$ is the combination of the active joint rotation around the base ϕ, and uncontrolled rotation due to the coupled complex motion generated by the active prismatic joints. Solution of the latter rotation can be calculated using the remaining scaler equation of the first constraint equation. Once this nonlinear equation is solved, orientation of end-effector with respect to F frame is found which can be used for extracting the simple rotational movement required in ϕ.

2.3.2 Motion Level Kinematic Analysis

Exploiting the hybrid structure of the mechanism and using Euler angles for orientation representation of the end-effector, one can obtain simpler solution for dependent coordinates of the end-effector body, p_1, p_2 and ψ_3. Therefore, given three possible p_3, ψ_1 and ψ_2 coordinates, configuration of

the end-effector with kinematic constraints can be defined by the transformation matrix:

$$ {}^{F}T^{E} = \begin{bmatrix} & & & p_1 \\ & {}^{F}R^{E} & & p_2 \\ & & & p_3 \\ 0 & 0 & 0 & 1 \end{bmatrix} \tag{2.11} $$

Note that ${}^{F}R^{E}$ represents the rotation matrix between end-effector and base of the parallel structure. Rotation matrix is formed with Euler angles sequence, 'XYZ', in which ψ_1, ψ_2 and ψ_3 are Euler angles for each axis of rotation, respectively. Active rotational DoF at base ϕ is omitted in singularity analysis without loss of generality, since finding singular positions in 3RPS kinematic chain would also identify workspace characteristics of the 3RPS-R device due to the hybrid nature of the mechanism.

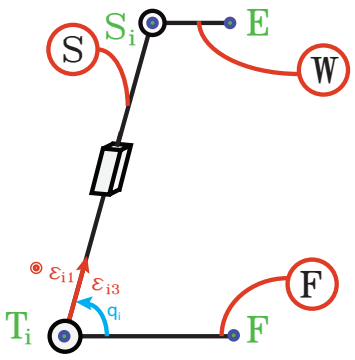

Figure 2.3: Schematic representation of a single leg of 3RPS-R device. q_2 is the passive joint angle between base and second leg, while $\boldsymbol{\varepsilon_1}$ and $\boldsymbol{\varepsilon_3}$ are frame vectors of the second leg formed with respect to the simple rotation of q_2.

In order to identify the Plücker vectors of 3RPS mechanism, loop equation on each leg is written.

$$ \mathbf{0} = \mathbf{r}^{\mathbf{F\,T_2}} + \mathbf{r}^{\mathbf{T_2\,S_2}} - \mathbf{r}^{\mathbf{T\,S_2}} - \boldsymbol{\chi} \tag{2.12} $$

where T_2 and S_2 are the revolute and spherical joint centers of the second leg, respectively, while F and E is the center points of base and end-effector bodies, Figure2.3. χ is the end-effector position which is defined as $\chi = p_1\,\mathbf{f_1} + p_2\,\mathbf{f_2} + p_3\,\mathbf{f_3}$. Taking the time derivative of loop Eqn. (2.12) with respect to base reference frame yields:

$$\mathbf{0} = \frac{{}^{\mathrm{F}}d\,\mathbf{r}^{\mathbf{F}\,\mathbf{T_2}}}{dt} + \frac{{}^{\mathrm{F}}d\,\mathbf{r}^{\mathbf{T_2}\,\mathbf{S_2}}}{dt} - \frac{{}^{\mathrm{F}}d\,\mathbf{r}^{\mathbf{E}\,\mathbf{S_2}}}{dt} - \dot{\chi} \tag{2.13}$$

with

$$\begin{aligned}
\frac{{}^{\mathrm{F}}d\,\mathbf{r}^{\mathbf{F}\,\mathbf{R_2}}}{dt} &= 0 \\
\frac{{}^{\mathrm{F}}d\,\mathbf{r}^{\mathbf{T_2}\,\mathbf{S_2}}}{dt} &= \frac{{}^{\mathrm{F}}d\,(\alpha_2\,\boldsymbol{\varepsilon_3})}{dt} = \dot{\alpha}_2\,\boldsymbol{\varepsilon_3} + \alpha_2\,\frac{{}^{\mathrm{F}}d\,\boldsymbol{\varepsilon_3}}{dt} \\
\alpha_2\,\frac{{}^{\mathrm{F}}d\,\boldsymbol{\varepsilon_3}}{dt} &= \alpha_2\,({}^{\mathrm{F}}\boldsymbol{\omega}^{\mathrm{S}} \times \boldsymbol{\varepsilon_3}) = \alpha_2\,\dot{q}_1\,(\boldsymbol{\varepsilon_1} \times \boldsymbol{\varepsilon_3}) \\
\frac{{}^{\mathrm{F}}d\,\mathbf{r}^{\mathbf{E}\,\mathbf{S_2}}}{dt} &= {}^{\mathrm{F}}\boldsymbol{\omega}^{\mathrm{W}} \times \mathbf{r}^{\mathbf{E}\,\mathbf{S_2}}
\end{aligned} \tag{2.14}$$

where α_2 is the variable for the prismatic link for the S body in Figure 2.3, while ${}^{\mathrm{F}}\boldsymbol{\omega}^{\mathrm{W}}$ is the angular velocity of the end-effector with respect to base. Substituting equations (2.14) into (2.13) and rearranging results:

$$\dot{\alpha}_2\,\boldsymbol{\varepsilon_3} + \alpha_2\,\dot{q}_1\,(\boldsymbol{\varepsilon_1} \times \boldsymbol{\varepsilon_3}) = \dot{\chi} + {}^{\mathrm{F}}\boldsymbol{\omega}^{\mathrm{W}} \times \mathbf{r}^{\mathbf{E}\,\mathbf{S_2}} \tag{2.15}$$

In order to analyze the relationship between prismatic joint angles α_i and end-effector configuration $[\dot{\chi}; {}^{\mathrm{F}}\boldsymbol{\omega}^{\mathrm{W}}]$, six scalar equations are needed which can be obtained by the scaler multiplication of the Eqn. (2.15) with two unit vectors of the same leg, $\boldsymbol{\varepsilon_1}$ and $\boldsymbol{\varepsilon_3}$.

$$\dot{\alpha}_2\,\boldsymbol{\varepsilon_3} \cdot \boldsymbol{\varepsilon_3} + \alpha_2\,\dot{q}_1\,(\boldsymbol{\varepsilon_1} \times \boldsymbol{\varepsilon_3}) \cdot \boldsymbol{\varepsilon_3} = \dot{\chi} \cdot \boldsymbol{\varepsilon_3} + ({}^{\mathrm{F}}\boldsymbol{\omega}^{\mathrm{W}} \times \mathbf{r}^{\mathbf{E}\,\mathbf{S_2}}) \cdot \boldsymbol{\varepsilon_3} \tag{2.16}$$

$$\dot{\alpha_2}\,\boldsymbol{\varepsilon_3}\cdot\boldsymbol{\varepsilon_1}+\alpha_2\,\dot{q_1}\,(\boldsymbol{\varepsilon_1}\times\boldsymbol{\varepsilon_3})\cdot\boldsymbol{\varepsilon_1}=\dot{\boldsymbol{\chi}}\cdot\boldsymbol{\varepsilon_1}+({}^{\mathrm{F}}\boldsymbol{\omega}^{\mathrm{W}}\times\mathbf{r}^{\mathbf{E}\mathbf{S_2}})\cdot\boldsymbol{\varepsilon_1} \quad (2.17)$$

Taken into account the Jacobi identity of cross product, equations (2.16) and (2.17) can be simplified to:

$$\dot{\alpha_2}=\dot{\boldsymbol{\chi}}\cdot\boldsymbol{\varepsilon_3}+{}^{\mathrm{F}}\boldsymbol{\omega}^{\mathrm{W}}\cdot(\mathbf{r}^{\mathbf{E}\mathbf{S_2}}\times\boldsymbol{\varepsilon_3}) \quad (2.18)$$

$$0=\dot{\boldsymbol{\chi}}\cdot\boldsymbol{\varepsilon_1}+{}^{\mathrm{F}}\boldsymbol{\omega}^{\mathrm{W}}\cdot(\mathbf{r}^{\mathbf{E}\mathbf{S_2}}\times\boldsymbol{\varepsilon_1}) \quad (2.19)$$

Note that while Eqn. (2.16) is defining the relation between end-effector configuration and input parameters, Eqn. (2.17) defines the relationship of dependent variables with respect to independent end-effector coordinates. Equations can be grouped in order to form:

$$\begin{bmatrix}\boldsymbol{\varepsilon_3}, & (\mathbf{r}^{\mathbf{E}\mathbf{S_2}}\times\boldsymbol{\varepsilon_3})\\ \boldsymbol{\varepsilon_1}, & (\mathbf{r}^{\mathbf{E}\mathbf{S_2}}\times\boldsymbol{\varepsilon_1})\end{bmatrix}\begin{bmatrix}\dot{\boldsymbol{\chi}}\\ {}^{\mathrm{F}}\boldsymbol{\omega}^{\mathrm{W}}\end{bmatrix}=\begin{bmatrix}\dot{\alpha_2}\\ 0\end{bmatrix} \quad (2.20)$$

Writing Eqn. (2.20) for each leg:

$$\mathrm{J_x}\,\dot{\boldsymbol{\chi}}=\mathrm{J_q}\,\dot{\mathbf{Q}} \quad (2.21)$$

where $\dot{\boldsymbol{\chi}}$ is the end-effector velocities $[\dot{\boldsymbol{\chi}};{}^{\mathrm{F}}\boldsymbol{\omega}^{\mathrm{W}}]$, while $\dot{\mathbf{Q}}$ is the augmented joint coordinates $[\dot{\alpha_i},\mathbf{0}]$. Note that in this equation, end-effector and joint coefficients (Jacobian matrices $\mathrm{J_x}$ and $\mathrm{J_q}=\mathrm{I}$, respectively) are 6×6 matrices which can be defined as full Jacobian matrices including the constraint relations due the deficient rank of three DoF manipulator.

2.4 Singularity Analysis with Grassmann Line-Geometry

In this framework, singularity analysis, which is carried out by utilizing Grassmann line geometry (studied by H. Grassmann (1809-1877)), is incorporated into the design process in two occurrences, during dimensional and workspace optimization procedures. Performance metrics used in dimensional optimization are global metrics, in other words, they are calculated over a predefined workspace which is desired to be singularity-free for all design configurations. Therefore, although singularity analysis in this study follows a similar approach to [70] in which singular configurations of a symmetric 3R$\underline{\text{P}}$S device is analyzed, this requires a more general approach which could also be used for analyzing non-symmetric configurations of 3R$\underline{\text{P}}$S-$\underline{\text{R}}$. Once the optimal dimensions are chosen, the same derivations are performed for the specified optimal design variable and identified singular configurations are used as a constraint in the workspace optimization process. Therefore, we approach the singularity analysis pragmatically, symbolical derivations performed here are only solved for the possible reach of the device, where singular configurations at crooked angles and very large or negative translational movements are not analyzed. For a symmetric mechanism, extensive analysis can be found in [70].

This section focuses on the Grassmann line geometry calculations and defining the Plücker vectors through vector notations for that purpose. For a 6 DoF mechanism this matrix could be derived trivially as the columns of the inverse transpose Jacobian. In particular, six Plücker vectors spans the Jacobian matrix of the mechanism J, which should be full rank in order to avoid singularity. This yields that six Plücker vectors that are defined specifically for the mechanism should be linearly independent [71, 72],

which could be checked with Grassmann set of lines; geometric conditions in order to detect that any subset spanned by n number of lines have a rank lesser than n. Therefore, identification of singularity loci requires the determination of configurations which satisfy Grassmann constraints over six linear varieties with a total of thirteen conditions.

Once it is possible to identify the singular configurations for different design parameters, a singularity free workspace is sought for all these parameter sets in order to identify a volume that at least cover the range for majority of the ADL tasks, where global optimization criteria can be safely computed.

2.4.1 Defining Plücker vectors for 3RPS Mechanism

The full Jacobian matrix J_x contains information on the Plücker vectors of the mechanism. Before advancing any further, a brief summary of Plücker vector definition is needed.

A line can be defined by its six dimensional Plücker vector given two points on the line and a reference point. Let M_1 and M_2 be the two points on the line and $\mathbf{a}$ be the vector defining the position of first point with respect to origin while $\mathbf{b}$ is the vector connecting the two points. Plücker vector is defined by:

$$\mathbf{P_D} = [\mathbf{b}\ (\mathbf{a} \times \mathbf{b})]^T; \tag{2.22}$$

According to this notion, two Plücker vectors for the second leg can be identified through Eqn. (2.20), $\mathbf{P_2}$ and $\mathbf{P_5}$ with $\mathbf{P_2} = [\boldsymbol{\varepsilon_3}, (\mathbf{r}^{\mathbf{E S_2}} \times \boldsymbol{\varepsilon_3})]^T$ and $\mathbf{P_5} = [\boldsymbol{\varepsilon_1}, (\mathbf{r}^{\mathbf{E S_2}} \times \boldsymbol{\varepsilon_1})]^T$. In particular, $\mathbf{P_2}$ defines a Plücker vector which is in the direction of prismatic joint $\boldsymbol{\varepsilon_3}$ and it passes through $\mathbf{r}^{\mathbf{E S_2}}$ while $\mathbf{P_5}$ also passes through same point with the direction of revolute joint $\boldsymbol{\varepsilon_1}$. However, the definition of a line passing through $\mathbf{r}^{\mathbf{E S_2}}$ needs an auxiliary

reference frame which has identical basis vectors with Newtonian frame but with e point as the origin according to the definition of Plücker vectors. In order to define the vectors in Newtonian frame from the base o, a modification on the last term of Eqn. (2.15) is necessary. Using the equality of $\mathbf{r}^{\mathbf{E}\mathbf{S_2}} = \mathbf{r}^{\mathbf{E}\mathbf{O}} + \mathbf{r}^{\mathbf{O}\mathbf{S_2}}$, it can be rewritten as

$$\dot{\alpha}_2\, \boldsymbol{\varepsilon_3} + \alpha_2\, \dot{q}_1\, (\boldsymbol{\varepsilon_1} \times \boldsymbol{\varepsilon_3}) = \dot{\vec{\chi}} + {}^{\mathrm{F}}\boldsymbol{\omega}^{\mathrm{W}} \times \mathbf{r}^{\mathbf{O}\mathbf{S_2}} \tag{2.23}$$

with $\dot{\vec{\chi}}$ defined as $\dot{\vec{\chi}} = \dot{\chi} + {}^{\mathrm{F}}\boldsymbol{\omega}^{\mathrm{W}} \times \mathbf{r}^{\mathbf{E}\mathbf{O}}$. Repeating the same intuitive steps, modified Jacobian matrix rows for the second leg can be obtained as :

$$\begin{bmatrix} \boldsymbol{\varepsilon_3}, & (\mathbf{r}^{\mathbf{O}\mathbf{S_2}} \times \boldsymbol{\varepsilon_3}) \\ \boldsymbol{\varepsilon_1}, & (\mathbf{r}^{\mathbf{O}\mathbf{S_2}} \times \boldsymbol{\varepsilon_1}) \end{bmatrix} \begin{bmatrix} \dot{\vec{\chi}} \\ {}^{\mathrm{F}}\boldsymbol{\omega}^{\mathrm{W}} \end{bmatrix} = \begin{bmatrix} \dot{\alpha}_2 \\ 0 \end{bmatrix} \tag{2.24}$$

Note that $\dot{\vec{\chi}}$ represents the velocity of the end-effector center which is projected to the Newtonian frame and Plücker vectors are defined with respect to the point o with the $\mathbf{r}^{\mathbf{O}\mathbf{S_2}}$ vector as the passing point. With the Plücker vectors for remaining legs defined, $\mathrm{J_x}$ can be written as $\mathrm{J_x} = [\mathbf{P_1}, \mathbf{P_2}, \mathbf{P_3}, \mathbf{P_4}, \mathbf{P_5}, \mathbf{P_6}]^T$. The schematic representation of Plücker vectors on 3R$\underline{\mathrm{P}}$S is given in Figure 2.4. Three of the Plücker vectors are coincident to each actuated prismatic link ($\mathbf{P_1}$, $\mathbf{P_2}$, $\mathbf{P_3}$) and three vectors are parallel to revolute joint directions at base and pass through consequent spherical joint points ($\mathbf{P_4}$, $\mathbf{P_5}$, $\mathbf{P_6}$). They are consistent with the literature where the motion characteristic of a symmetric 3R$\underline{\mathrm{P}}$S mechanism is analyzed with Screw Theory [70, 73].

Using a full rank Plücker vector based on full Jacobian $\mathrm{J_x}$ which inherits not only the relation between generalized speeds and joint variables but also the constraint equations of the system yields a combined Jacobian

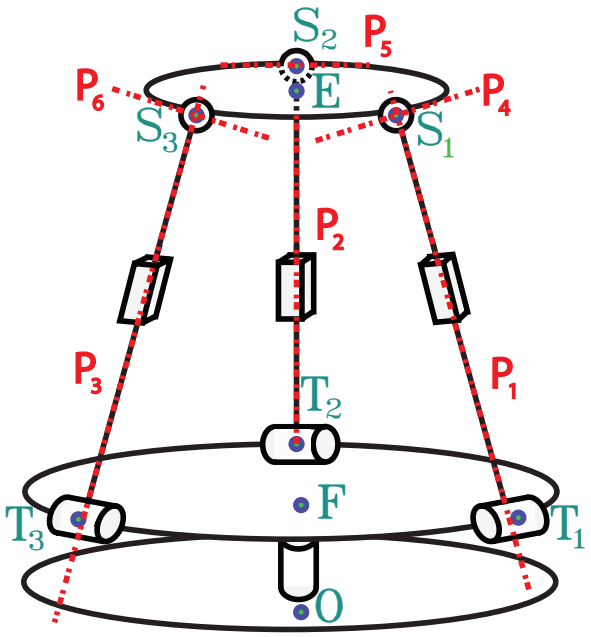

Figure 2.4: Schematic representation of 3RPS-R device with Plücker vectors

matrix in the sense of singularity types. Therefore, as suggested in [74, 75], singularity analysis through these Plücker vectors is necessary and sufficient condition in order to identify all types of singular configurations of the mechanism without any possible identification of the particular type.

2.4.2 Grassmann Geometric Constraints

In order to analyze the linear dependencies of six Plücker vectors, therefore, identify the singularity loci, configurations which satisfies Grassmann geometric constraints over six linear varieties should be determined. For more detailed description of finding singular configurations of parallel mechanisms with Plücker vectors and Grassmann line geometry, readers should also refer to [71, 72]. As previously mentioned, in order to detect

that any subset spanned by n number of lines have a rank lesser than n, configurations which satisfy Grassmann constraints over six linear varieties with thirteen conditions should be identified.

The first variety is the empty set of rank 0. Next one is the point (rank=1) which is corresponding to a line in 3D space. The second variety is called lines (rank=2) and have two possible occurrence; either as a two skewed lines in $\mathfrak{R}^3$ which does not intersect (2a), or a pencil of lines; all lines are in the same plane and intersects at a certain point (2b). The planes (rank=3) can be formed with four different types. A regulus (3a), union of two flat pencils in distinct planes with distinct centers having a line in common (3b), all lines go through a point (3c) and all lines are in a plane(3d). Moreover, varieties of dimension 4 are called congruences which has also four types. Elliptic congruence (4a) is the case when a linear spread is generated by 4 skew lines. Hyperbolic congruence (4b) occurs when all the lines are concurrent with two skew lines. Parabolic congruence (4c) is a one-parameter family of flat pencil, having one line in common which forms a variety. Last type is the degenerate congruence (4d) where a minimum of two lines out of five lines are coplanar and the remaining lines intersect at a point on the plane. Varieties with (rank=5) are called complexes with two types, non-singular complex (5a) is generated by five independent skew lines and singular (or special) complex is defined by all the lines meeting at one given line (5b).

The detailed definition of each variety and their corresponding solutions for 3RPS mechanism are summarized in Table 2.2. Solutions of each singular configuration are provided in Appendix A for further details. Note that definition of singularities according to each variety is defined vector based which could easily be solved with numerical analysis over

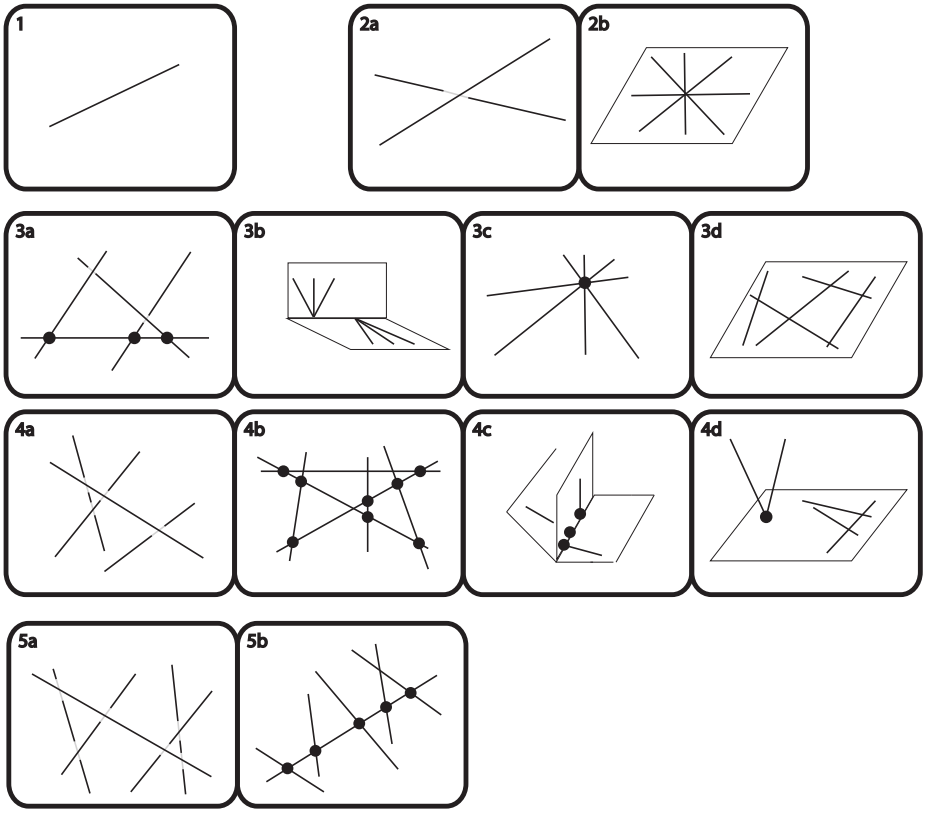

Figure 2.5: Grassmann varieties

the workspace for any set of dimension values. Therefore it can be easily incorporated to the design process at desired steps. In this work, this analysis is utilized for determining a singularity free workspace for all variable sets in dimensional optimization and a case specific analysis for the chosen design configuration through the workspace optimization. Numerical solutions of these calculations would be given in relevant places. However, keeping in mind that for both cases, singular values which are inside our search space are relevant, and in order to sum up the varieties which resides in 120 *mm* to 160 *mm* translational DoF;

- (2b) where end-effector plane is parallel with the plane built by two

leg Plücker vectors [(1 configuration * 3 leg dual combinations) for each translational DoF],

- (4b) where there exists two lines which intersects four Plücker vectors,[(1 configuration * 3 leg dual combinations) for each translational DoF]

- (5a) where intersection of three planes constructed by the Plücker vectors on each leg intersects the end-effector plane,[3 translational values of which one is between desired range for each configuration]

- (5b) where there exists two lines which intersects six Plücker vectors,[(1 configuration * 3 leg dual combinations) for each translational DoF]

Configuration for (2b) is trivial to visualize and solve numerically; a sample singular configuration is given in Figure 2.6. Conditions (4b) and (5b) are either at crooked angles or configurations way out of the desired workspace of the mechanism [70].

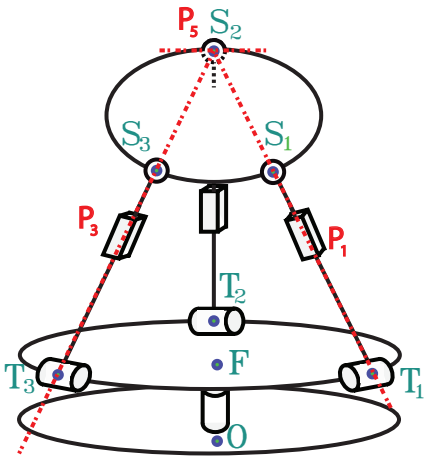

Figure 2.6: Singular 3RPS-R condition under (2b)

Singular points lying between 10 and 160 mm translational movement for all available conditions are marked in Figure2.7 for an asymmetric mechanism, particularly with 105.8° connection angle and 55 mm 121.4 mm top and base platform radii. Singular conditions lying between 120 and 160 mm which is the estimated range of motion of the mechanism in $\mathbf{n_3}$ axis and within the range of motion for rotational DoFs of human are solely based on condition (5a) and pointed out with red markers. It should be noted singular configurations for all conditions are undergone slight modifications based on the connection angles, but most notable change is second set of lines of (5b) condition ($5b_{2i}$) which is only apparent in asymmetric designs such as given example, although they do not impose any restrictions in usable workspace. However, this sub-condition was not geometrically possible in symmetric case [70].

Table 2.2: Singularity Analysis of 3RPS Device with Grassmann Line Geometry

Variety	Name	Condition	Validation	Singular Configurations
1	1	A line degenerates to a point in $\mathfrak{R}^3$	Only Plücker vectors that can degenerate to points are associated with prismatic joints, which means link lengths becomes zero. This is not possible due to the physical design.	None
2	2a	Two skewed lines in $\mathfrak{R}^3$ which does not intersect	Two skew lines (zero-pitch screws) are only dependent on themselves, therefore, this case is not a potential case of an uncertainty.	None
2	2b	Pencil of lines; all lines are in the same plane and intersects at a certain point	Two leg Plücker vectors can form a plane with one constraint vector and a common intersection point can be spotted on this plane.	$\mathbf{P_1}$, $\mathbf{P_3}$ and $\mathbf{P_5}$ lines intersect at s_2 Figure 2.6 and similar configurations for each leg.

Continued on next page

Table 2.2 – continued from previous page

Variety	Name	Condition	Validation	Singular Configurations
3	3a	Three independent lines belonging to a regulus	Every couple of lines intersects at each spherical joint location, therefore fourth line belonging to either of the regulus does not exist [72].	None
3	3b	Two flat pencils having a line in common and lying in distinct planes and with distinct centers	Not possible since only flat pencil can be generated with the condition 2b, where other lines are either coplanar with end-effector (constraint Plücker vectors) or intersecting at the same point (remaining leg vector $\mathbf{P_2}$).	None
3	3c	A minimum of three lines passing through a point	In configurations where condition 2b is valid, a forth line (remaining leg Plücker vector) is always intersecting three lines of planar pencil at a common point..	Same as 2b
3	3d	A minimum of three coplanar and non concurrent lines	Translational movement of the mechanism should be zero, which is not possible.	None
4	4a	A linear spread is generated by 4 skew lines	Similar to 3a, five skew Plücker vectors cannot be identified.	None

Continued on next page

Table 2.2 – continued from previous page

Variety	Name	Condition	Validation	Singular Configurations
4	4b	All four lines are concurrent with two skew lines	Two lines which intersects quadruplets of Plücker vectors (two leg, two constraint vectors) can be identified for each couple of mechanism legs.	For ($\mathbf{P_1}$, $\mathbf{P_4}$, $\mathbf{P_2}$ and $\mathbf{P_5}$) intersects with γ and β; γ is in the direction of $\mathbf{r}^{s_1 s_2}$ and passes through corresponding spherical joint, while β is the intersection of planes spanned by the duple set of Plücker vectors ($\wp_{14}$: $\mathbf{P_1}, \mathbf{P_4}$, $\wp_{25}$: $\mathbf{P_2}, \mathbf{P_5}$). Should be checked for all combinations of four Plücker vectors, ($\mathbf{P_1}$, $\mathbf{P_4}$, $\mathbf{P_3}$ and $\mathbf{P_6}$) and ($\mathbf{P_2}$, $\mathbf{P_5}$, $\mathbf{P_3}$ and $\mathbf{P_6}$).
4	4c	Four lines form among themselves three planes with family of flat pencils, having one line in common.	Similar to 3b, this condition cannot be realized.	None

Continued on next page

Table 2.2 – continued from previous page

Variety	Name	Condition	Validation	Singular Configurations
4	4d	If a minimum of two lines out of five lines are coplanar and the remaining lines intersect at a point on the plane	All possible conditions should be checked. 1)Having five coplanar lines is not possible. 2)Four coplanar lines and one line with a certain point on that plane: This case is identical to 3d, which is not possible. 3)Three coplanar lines and two lines intersecting a point on the plane: Three constraint vectors are coplanar, however, the intersection point for each couple of leg vectors can be on this plane only for zero translation value where end-effector plane is identical with the base plane. This is also valid for coplanar leg vectors and it is not realizable in mechanism. If the two constraint lines and one leg line are chosen as coplanar, for example $\mathbf{P_1}$, $\mathbf{P_4}$ and $\mathbf{P_5}$, two vectors can be found which intersects this plane at the same point ($\mathbf{P_3}$ and $\mathbf{P_6}$ intersecting at s_3). However this case is identical to the condition (2b) in this mechanism.	Identical to either 3d (None) or 2b
5	5a	General complex generated by five independent skew lines	The coplanar lines of a complex meet at a common point.	Check if the intersection of three planes constructed by the Plücker vectors on each leg intersects the end-effector plane.
5	5b	Special complex is generated by five skew lines intersecting with a line.	There exist a line which pass thorough six vectors.	This case can be build over 4b; common lines in 4b could be used as basis and checked if either of them intersects remaining Plücker vectors.

2.4.3 Singularity-Free Workspace Analysis for Non-Symmetric 3RPS Mechanism

Objective functions that are based on kinematic or dynamic properties are more meaningful when they are global representations over the workspace of the device. However, as it is previously mentioned, singular configurations of the mechanism is affected by its dimensions, especially considering the variables chosen in this work; joint placement angle significantly alters the device's behavior. Therefore, prior to any optimization step, a preliminary analysis is performed in this subsection which identifies the limits of the singularity free workspace in which global performance functions can be calculated.

The initial span of parameters that will vary to optimize the performance measures are $\theta = 75°...120°$ for the joint placement angle, and $\eta = 0.25...0.90$ for the ratio of the radii of the two platforms. However, one of the essential design constraints of the mechanism is to cover the functional ROM of the human wrist during ADL, in particular, at least $45°$ for flexion/extension and -40 to 20 for radial/ulnar deviation and it is desired to utilize the optimization procedure at least with this workspace volume. For Figure 2.8 demonstrates singularity free workspace over ψ_1 and ψ_2 between 120 mm and 160 mm translational DoF for a sample of design configurations, which shows that this workspace volume has singular configurations for some of the design parameters.

Analysis of different design configurations points out that singularity free workspace of the mechanism for all design parameters are close to the volume desired by the activities of daily living. However, when the

connection angle of joints are at exactly 90°, singular configurations exists within the outer boundary therefore limiting the continuous workspace grid. Since, a grid based singularity identification is applied, this becomes too much of a risk considering the grid may not be sufficiently detailed to catch other singular configurations within the workspace. Therefore, with also eliminating the first set of ratio of radii of two platforms η, singularity free workspace for remaining design parameters can be identified as shown in Figure 2.9 which yields $\eta'' = 0.30...0.90$ and $\theta'' = 92.5°...120°$ for new parameter space. The final workspace W for optimization becomes the points lying in the safe zone which are marked with red dots, in particular, it represents a singularity free workspace that is identified for all design variables which also can cover the workspace volume for majority of the ADL tasks. Translation DoF is set to 125 mm and serial rotational DoF is kept at initial value for the sake of computational complexity.

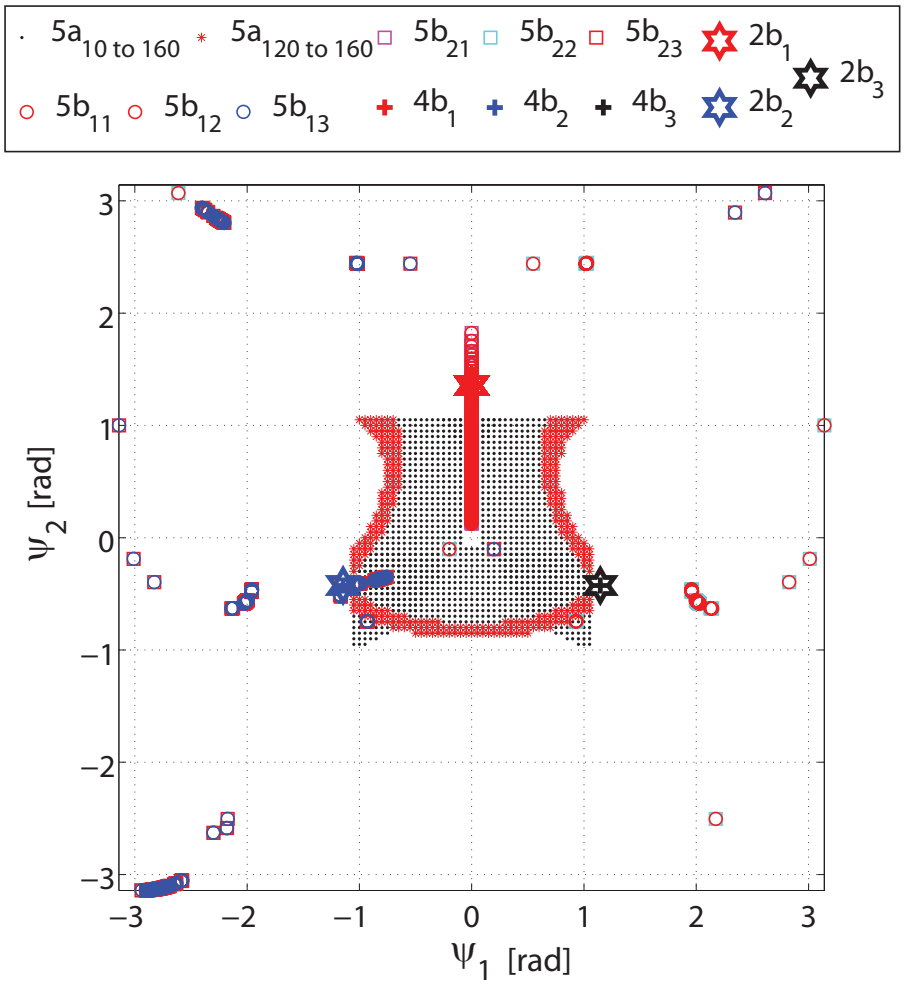

Figure 2.7: Singular 3RPS-R configurations for all conditions between 10 and 160 *mm*

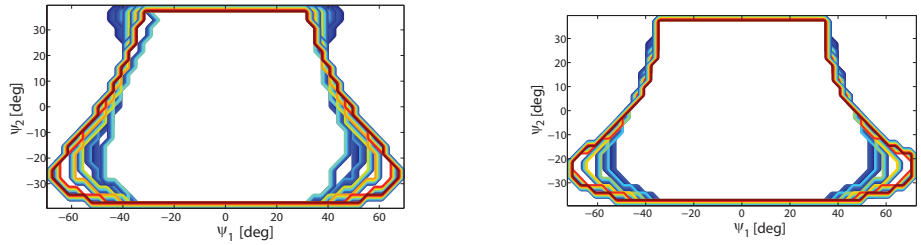

(a) Different joint placement angles over a predefined $\eta = 0.45$

(b) Different ratio of radii of two platforms at a predefined $\gamma = 105°$

Figure 2.8: Singular configurations for different design configurations.

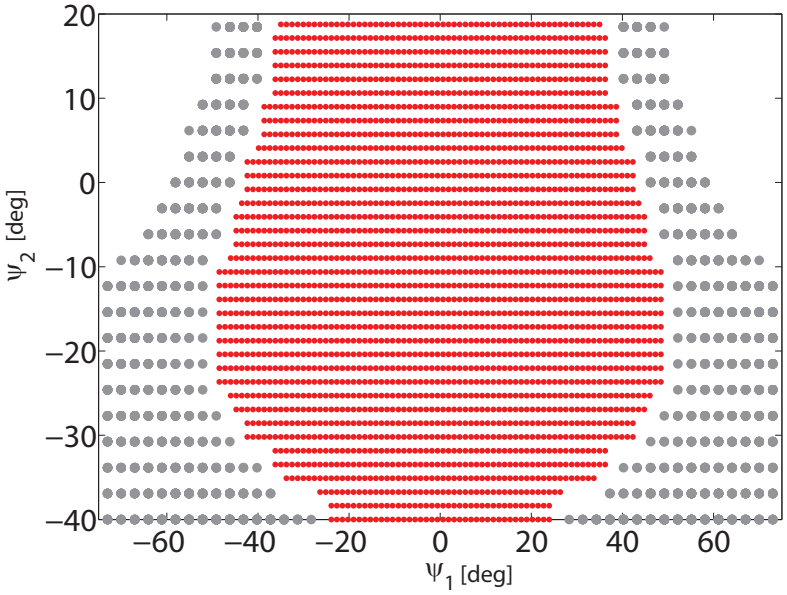

Figure 2.9: Singularity-free workspace that is used in multi-criteria dimensional optimization.

2.5 Optimal Dimensional Synthesis

Dimensions of the parallel mechanisms change the performance of the device drastically, necessitating an optimization procedure for increased efficiency [76, 77, 78]. These studies determine the set of non-dominated solutions by characterizing the trade-off between actuator utilization and dynamic performance of the 3RPS-R wrist exoskeleton and suggest dimensions of the mechanism to achieve an "optimal" solution [79]. Selecting the performance measures for the optimization is crucial and highly application-oriented. Hence, the choice of the optimization measures should be well established in accordance to the optimal requirements in Section 2.2.

2.5.1 Determination of Performance Criteria

The proposed mechanism is designed specifically for active forearm and wrist rehabilitation exercises primarily along the flexion/extension and abduction/adduction and secondarily along pronation/supination DoF. Therefore, it is natural to maximize the actuator utilization along these DoF. Considering the device is designed to function with human hand in the loop, imposing worst-case kinematic isotropy measures as performance criteria would be too conservative. Consequently, a sensible performance measure to optimize in order to maximize actuator utilization is the average kinematic isotropy index (AII). Kinematic based performance metrics based on isotropy index such as AII are useful to represent important characteristics of the robot, however, limited information on the behavior of the robot under control implementation can be obtained without the dynamical properties. In particular, high mass values are shown to be detrimental to control performance, in not only the stiffness bandwidth

of the device [80], but applications based on tele-operation [81]. Therefore, in order to increase the control performance, Global Dynamic Index (GDI) is chosen for the second performance metric which penalizes the biggest eigenvalue of mass matrix. Since these two performance metrics are not only essential and dependent to each other, which necessitates a multi criteria optimization that concurrently tackles the problem, but also global measurements, in a sense that they are calculated over a predefined workspace which should be chosen to be singularity-free for all parameters sets as shown in sub-section2.4.3.

2.5.2 Scaling of Jacobian and Mass Matrix

The kinetostatic performance of the robot is characterized by four by four matrix which demonstrates the relationship between input and output generalized velocities for 3RPS-R device. Let J_x be defined as:

$$J_x = \begin{bmatrix} W_{4x4} & V_{4x2} \\ T_{2x4} & U_{2x2} \end{bmatrix} \tag{2.25}$$

Then:

$$\begin{bmatrix} \dot{p}_3 \\ \omega_1 \\ \omega_2 \\ \omega_3 \end{bmatrix} = J_{4x4} * \begin{bmatrix} \dot{\alpha}_1 \\ \dot{\alpha}_2 \\ \dot{\alpha}_3 \\ \dot{\alpha}_4 \end{bmatrix} \tag{2.26}$$

where,

$$J_{4x4} = W_{4x4} + V_{4x2}\, U_{2x2}^{-1}\, T_{2x4} \tag{2.27}$$

However, before advancing further, it should be noted that 3RPS-R device has a Jacobian matrix with mixed physical units and measures based on condition number of the Jacobian matrix is of little practical significance

in the presence of non-uniform physical units [82, 83]. For that purpose, several normalization methods have been proposed such as characteristic length [84] or natural length [85]. Despite all these techniques, a task-space based normalization method is chosen [86, 87, 82], since it provides a systematical way to incorporate additional design goals into the optimization procedure utilizing the required end-effector forces into the normalization procedure. In order to summarize, task and joint space forces are represented as their maximum values:

$$\boldsymbol{\tau} = \mathrm{J}^{\mathrm{T}}\mathbf{F} \tag{2.28}$$

$$\mathbf{F} = \mathrm{S}'_{\mathrm{R}}\,\mathrm{S}'_{\mathrm{T}}\,\Delta\mathbf{F} \tag{2.29}$$

$$\boldsymbol{\tau} = \mathrm{S}_{\mathrm{J}}\,\Delta\boldsymbol{\tau} \tag{2.30}$$

$$\mathrm{S}_{\mathrm{T}} = \mathrm{S}'_{\mathrm{R}}\,\mathrm{S}'_{\mathrm{T}} \tag{2.31}$$

$$\hat{\mathrm{J}} = \mathrm{S}^{\mathrm{T}}\,\mathrm{J}\,\mathrm{S}_{\mathrm{J}}^{-1} \tag{2.32}$$

where S'_{T} and S_{J} are diagonal scaling matrices with maximum values for end-effector and joint space forces, respectively, while S'_{R} is a task space rotation matrix which is used to rotate axis of desired force ellipse if the end-effector vectors are not aligned to the origin frame, which is in this case equals to identity matrix. Finally $\hat{\mathrm{J}}$ becomes the normalized Jacobian matrix.

As mentioned previously, this approach enables the incorporation of some primary and secondary requirements into the optimization procedure. In particular, maximum force and torque values can be chosen for the focused human joint and the used kinematic structure, since the mechanism would be optimal when it can ensure the enforced normalization values. This also means that changing these parameters would change the

outcomes of the optimization procedure provided in this work, which in itself, makes this method a general approach for different applications.

In this particular case, the end effector force scaling matrix is derived with the help of isometric strength of human from Table 2.1 (symmetric torque outputs for flexion/extension and radial/ulnar deviation 20 Nm, and 10 Nm for forearm pronation/supination), with slight modifications. Taking into account the hybrid kinematics structure of the robot, forearm rotations that are mostly caused with the rotation at the serial part are deliberately limited in kinematic analysis. Moreover, flexion/extension movement is slightly favored over radial/ulnar deviation in normalization, based on the higher RoM at this rotation in human movements. The remaining maximum translational force can be set arbitrarily, since it will be mostly used as a passive element and chosen to be 30 N, which is around the maximum translational force seen at the end-effector when all motors are at their continuous maximum. The torque maximums, S_J is set to identity matrix for parallel mechanism, since identical motors would be used for actuation. Torque value for the serial part is chosen arbitrarily within the implementable region. Considering that normalization of any scaling matrix is possible without loss of generality [87], both matrices can be rewritten as:

$$S_T = \text{diag}[0.03, 23\ mm, 20\ mm, 5\ mm] \tag{2.33}$$

$$S_J = \text{diag}[1, 1, 1, 400\ mm] \tag{2.34}$$

For the scaling of the mass matrix, a similar approach can be applied:

$$\mathbf{F} = \mathrm{M}_{\mathrm{end}}\,\ddot{\mathbf{x}} \tag{2.35}$$

$$\mathrm{S}_{\mathrm{T}}\,\Delta\mathbf{F} = \mathrm{M}_{\mathrm{end}}\,\mathrm{S}_{\mathrm{A}}\,\Delta\,\mathbf{a} \tag{2.36}$$

$$\hat{\mathrm{M}}_{\mathrm{end}} = \mathrm{S}_{\mathrm{T}}^{-1}\,\mathrm{M}_{\mathrm{end}}\,\mathrm{S}_{\mathrm{A}} \tag{2.37}$$

where S_{A} are diagonal scaling matrix for maximum acceleration of the end-effector, $\mathrm{M}_{\mathrm{end}} = \mathrm{J}^{-\mathrm{T}}\,\mathrm{M}\,\mathrm{J}^{\mathrm{T}}$ represents the mass matrix observed at end-effector space and $\hat{\mathrm{M}}_{\mathrm{end}}$ is the normalized mass matrix. While maximum force requirements are kept as same as the kinematic normalization, maximum acceleration values are set such that:

- Acceleration of the seldom used translational DoF is set to be particularly slow than the rotational axes movements,
- Movement against the gravitational force (radial/ulnar deviation) is slower than flexion/extension and,
- Maximum acceleration of the forearm rotation is higher than the other rotations, since moment of rotation during this movement is significantly higher than the other axes due to the rotation of the whole parallel structure with this DoF.

$$\mathrm{S}_{\mathrm{A}} = \mathrm{diag}[1\ mm/s^2, 1\ rad/s^2, 0.5\ rad/s^2, 4\ rad/s^2] \tag{2.38}$$

2.5.3 Solving Dimensional Optimization

With the normalized Jacobian and Mass metric, objective functions AII and GDI can be given as:

$$\mathcal{AII} = avg_{\boldsymbol{\kappa}_0,\boldsymbol{\kappa}_1 \in W} \frac{\underline{\sigma}(\hat{\mathrm{J}}(\boldsymbol{\rho},\boldsymbol{\kappa}_0))}{\overline{\sigma}(\hat{\mathrm{J}}(\boldsymbol{\rho},\boldsymbol{\kappa}_1))} \tag{2.39}$$

$$\mathcal{GDI} = min_{\boldsymbol{\kappa_0},\boldsymbol{\kappa_1}\in W}\frac{1}{1+\overline{\sigma}(\hat{\mathrm{M}}_{\mathrm{end}}(\boldsymbol{\rho},\boldsymbol{\kappa_1}))} \tag{2.40}$$

$\underline{\sigma}$ and $\overline{\sigma}$ are the minimum and maximum singular values of the Jacobian or Mass matrix, $\boldsymbol{\kappa_0}$ and $\boldsymbol{\kappa_1}$ are the configurations in the workspace that result in the extreme values, $\boldsymbol{\rho}$ is the column matrix of design variables. Finally W is the singularity free workspace for the design variable sets which is calculated in subsection 2.4.3.

The negative null form of the multi-objective optimization problem can be stated as

$$\begin{aligned} max\ \ & \mathbf{F}(\boldsymbol{\rho},\boldsymbol{\beta},\boldsymbol{\kappa}_0,\boldsymbol{\kappa}_1) \\ & \mathbf{G}(\boldsymbol{\rho},\boldsymbol{\beta}) \leq 0 \\ & \mathbf{H}(\boldsymbol{\rho},\boldsymbol{\beta}) = 0 \\ & \boldsymbol{\alpha}_l < \boldsymbol{\alpha} < \boldsymbol{\alpha}_u \end{aligned} \tag{2.41}$$

where **F** represents the column matrix of objective functions that depend on the design variables $\boldsymbol{\rho}$ and parameters $\boldsymbol{\beta}$. Symbols **G** and **H** represent the inequality and equality constraint functions that also depend on design variables and parameters. Finally, $\boldsymbol{\alpha}_l$ and $\boldsymbol{\alpha}_u$ correspond to the lower and upper bounds of the design variables, respectively. The 3R$\underline{\text{P}}$S-$\underline{\text{R}}$ mechanism has two parameters $\beta_1 = R$ and $\beta_2 = W$, where R is the radius of the fixed platform and selected as 121.4 mm, complying with statistical data on human joint sizes and based on manufacturing issues.

The column matrix of objective functions **F** is given as

$$\mathbf{F_{Rehab}} = \begin{bmatrix} max\,\mathcal{AII} \\ min\,\mathcal{GDI} \end{bmatrix}$$

while the inequality and equality constraints **G** and **H** are imposed during kinematic analysis to ensure the closed kinematic chain for the 3R$\underline{\text{P}}$S-$\underline{\text{R}}$

platform.

Optimization of AII and GDI needs to be simultaneous, since both objective functions have opposing behavior over the search space. For this multi-criteria optimization, Normal Boundary Intersection (NBI) is chosen [88] which is a gradient based framework that is computationally efficient, applicable to any set of performance indices, and extendable to include any number of design criteria that is required by the application. NBI approach attacks the geometric problem directly by solving for single-objective constrained subproblems to obtain uniformly distributed points on the hyper-surface. For that purpose the minimum of each objective function, so-called *shadow points* must be specified. These are the single criterion optimum of each objective function. The single criterion objective functions for AII and GDI performance metrics are non-convex, which implies that gradient-based searches will most probably get stuck in local optima. Therefore, a brute-force search is conducted in both the workspace and parameter space. Although, it is computationally expensive to go through this search to obtain the shadow points, this is only done once unlike the weighted sum methods where the procedure needs to be repeated for each weight assignment. The functions to be optimized can be visualized by graphing them in as surfaces in $\mathbb{R}^3$, Figure 2.10, which confirms an apparent trade-off between AII and GDI. In particular, as the mechanism becomes more symmetric and/or bigger, AII gets better while GDI of the mechanism gets worse.

2.5.4 Selection of the Optimal Design

The trade-off between AII and GDI is also obvious in the Pareto-front curve given in Figure 2.11. All the points lying on the curve are non-dominated

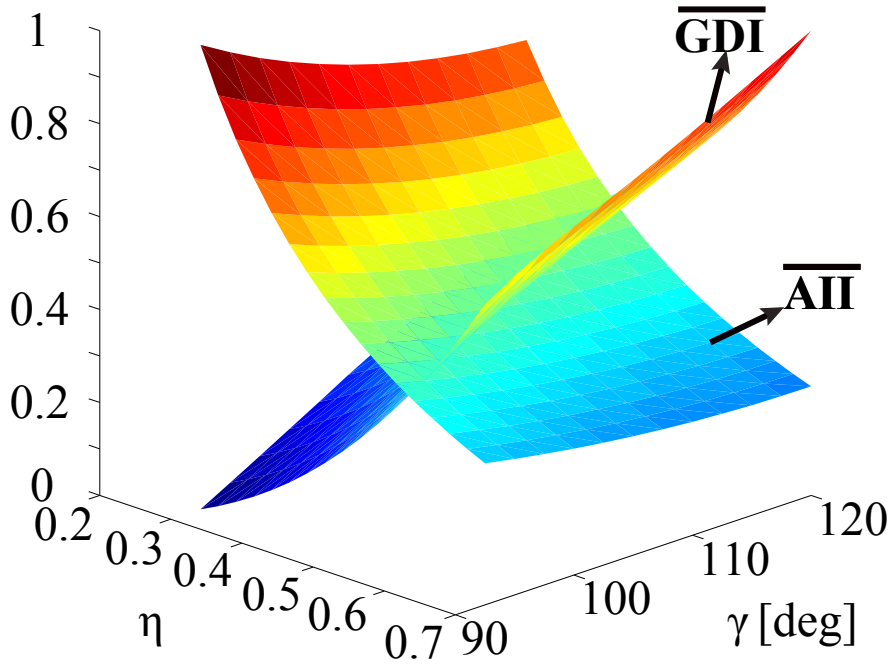

Figure 2.10: Objective functions

solutions of the multi-criteria optimization problem which makes every one of them a possible design candidate. However, since only one design can be implemented, additional sensible constraints have to be imposed to choose from these candidates. One of the prominent primary objectives is volume index that needs to be selected as high as possible to ensure the robot does not use up too much space as compared to its workspace. This constraint is sometimes called the footprint area constraint. Imposing this constraint by not choosing those points that yield a radii ratio of less than 60%, approximately half of the points in the Pareto-front are eliminated. Moreover, a design which highly favors any metric to the other one are not desired since both of performance metrics are of equal importance. This criterion indicates the elimination of solutions in the

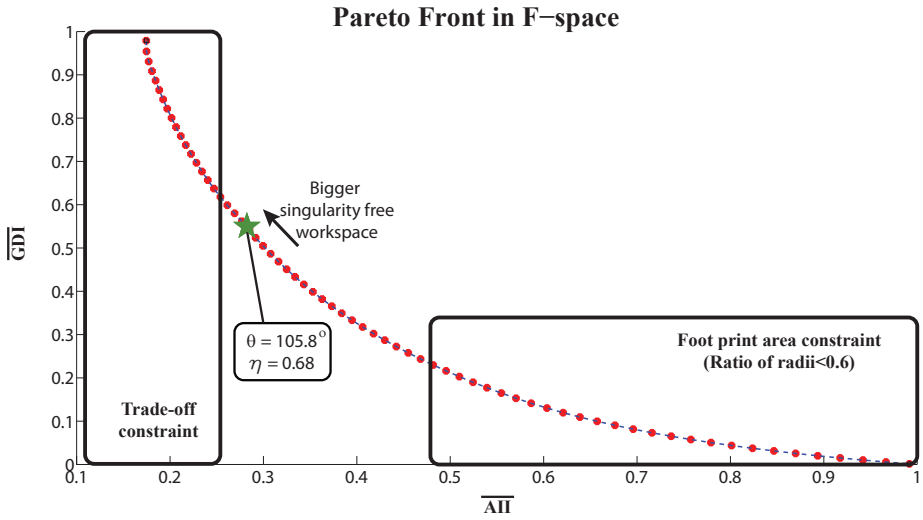

Figure 2.11: Pareto solution of the given multi-criteria optimization.

neighborhood of the shadow points. The final selection is then made among the remaining points in the Pareto-curve by considering the singularity free workspace volume and ease-of-manufacturing issues. One of the many advantages of the multi-objective optimization is the capability of finding as many optimal points on the Pareto as needed. This advantage is exploited in implementation of the selected design, hence, mechanical design has its own challenges and some of these Pareto points are harder to materialize. As a result, although, any of the remaining Pareto points can be chosen for design configuration, marked solution in Figure 2.11 which corresponds to $\theta = 105.8°$, and the ratio of the radii of the two platforms, $\eta = 0.68$ is chosen to merely satisfy some hardware manufacturing advantages. With base platform fixed to a radius of 121.4 mm, final design parameter, radius of the wrist platform, is calculated as 82.5 mm.

2.6 Implementation and Characterization

Design of the rehabilitation device is performed in parallel to performance criteria for a rehabilitation device summarized in Section 2.2. While most of these requirements are enhanced through the theoretical design of the exoskeleton, some design requirements needs careful elaborations in mechanical implementation process, which, this section summarizes. However, as it is mostly the case, a part which is highly advantageous in one of the design requirements may be the bottleneck in another one. The most influential case in this design is the choice of spherical joint used in implementation, which provides very smooth motion with no backlash, despite containing a limited swing angle.

Therefore, the mechanism can still be improved in terms of its workspace even after the dimensional optimization is performed. By changing the attachment orientation between spherical joints and end-effector, inherent physical limit of the spherical joints over the mechanism workspace may be reduced. Workspace optimization may include different performance metrics such as one of the two DoF or the total volume covered. However, the final choice of dimensions and outcomes of workspace optimization should not endanger the safety of the device which requires that final workspace of the mechanism stay in-between singularity free region which can be calculated specifically for the chosen optimal design by the symbolical derivations defined in Section 2.4.

Once these choices are made and the device is physically completed, characterization of the actual device performance is fundamental to establish the validity of the design and discover whether or not there are any shortcomings. To this end, the device has been tested on several such criteria.

2.6.1 Physical Implementation

First implementation detail is based on the choice of actuator and transmission system, since this step has the highest impact on the mechanism performance. To ensure high back-driveability, direct-drive linear motors are chosen to provide linear motion at the prismatic joints, while the base platform is actuated with a DC motor through capstan drive according to the higher power requirements of the forearm rotation. To implement the joints of the mechanism, micro-precision spherical rolling joints are utilized to connect the moving platform to the linear actuators, while commercial ball bearings are used as the passive revolute joints near base. In order to make the device easier to wear and increase ergonomy, it is decided to open the upper side of the base ring, which is realized with the help of THK HCR curved slides. Furthermore, specially designed stainless steel parts with emptied inside and reinforced with honeycomb structure are produced which provide reliable but lightweight design. Results of the workspace optimization are validated with custom wrist part manufacture as shown in Figure 2.12. With these modifications, improvements on flexion-extension RoM, robustness and wearability are satisfied.

As far as the implementation details are concerned, the forward and inverse kinematics of the 3RPS-R mechanism are solved using numerical integration [89]. Since, the encoders situated on the actuators are only capable of position measurement, angular velocities are estimated using Euler approximation with a nonlinear estimator based on the adaptive identification method [90], in an effort to reduce the numerical noise. Implementation of the controller is realized on a desktop computer equipped with an I/O card running Quarc 2.0 and Matlab. Controllers are programmed in C for real-time implementation and the sampling frequency

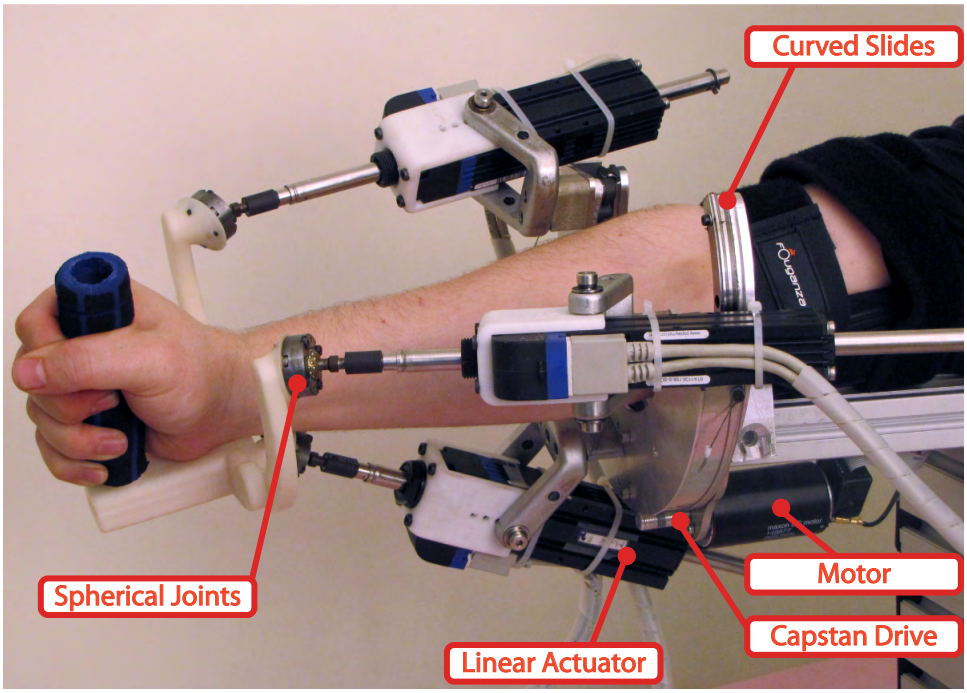

Figure 2.12: The prototype of the 3RPS-R exoskeleton

is set to 1 kHz.

2.6.2 Workspace Optimization Considering Joint Limits

Spherical joints of the device are implemented by micro-precision spherical rolling joints which are very smooth with no backlash, however, they have a limited angular travel capabilities which limits the reach of the device in physical implementation. It is possible to increase the usable workspace of the 3RPS-R mechanism by properly offsetting attachment orientations of the spherical joints. Since the determination of these orientations is not trivial for non-symmetric mechanisms with a non-symmetric workspace, optimization is performed for the 3RPS-R mechanism with 105.8° joint placement that is designed to match the non-symmetric task space of the human wrist.

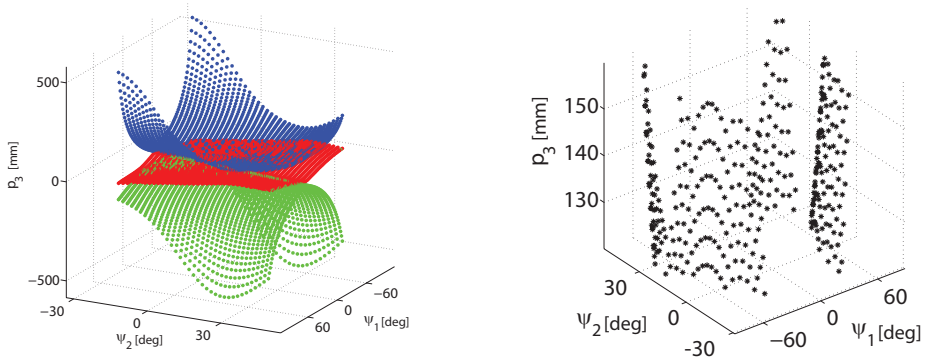

(a) Singularity curves for the device (5a). (b) Parameter space of the solution set.

Figure 2.13: Singularity curves for the final device (5a) between 120 and 160 *mm*

In order to guarantee that final design has no singular configurations in its reachable workspace, singularity analysis is included into the optimization procedure as a constraint. For this design configuration, singular translational DoF calculated with (5a) for ψ_1 and ψ_2 limited between human workspace limits as given in Table 2.1 are shown in Figure 2.13a. Taking into account that achievable translational DoF (120 to 160 *mm*) caused by the mechanical limits, we can acquire singular configurations that are relevant to the optimization process, Figure 2.13b.

To form the optimization problem, let angles Ξ_{i_1}, Ξ_{i_2} and Ξ_{i_3} define the orientation offset at each connection point s_i in Euler angles representation for $i = 1, 2, 3$ as depicted in Figure 2.14. Here, Ξ_{i_1} are measured around axes that are parallel to the first body axis $\mathbf{e_1}$ of end-effector body, while Ξ_{i_2} are measured around complementary axes which are parallel to the second body axis $\mathbf{e_2}$ of the end-effector body. All orientation angles are taken as positive when measured counter clockwise. These definitions lead to nine design variables to be selected to optimize the device workspace. However, it is possible to decrease the dimension of the search space considerably

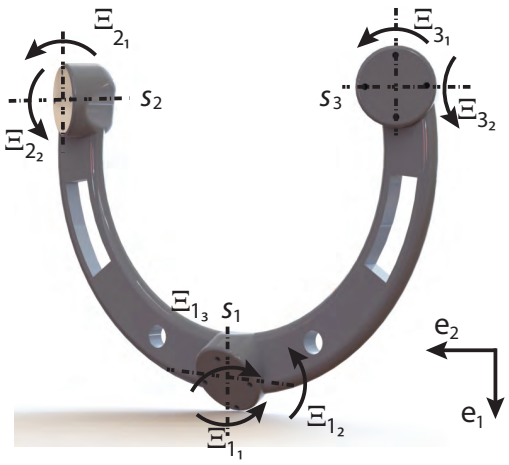

Figure 2.14: The moving platform of 3RPS-R with offsets at the connection points. Offset angles are marked on the figure.

by noting the design requirements for wrist rehabilitation. In particular, since the range of motion (RoM) for the flexion/extension movements is desired to be symmetric, Ξ_{1_1} and Ξ_{1_3} can be set to zero. Similarly, since it should be possible to utilize the device on both the right and the left arm of the patients, orientations at connection points s_2 and s_3 should be mirror imaged. As a result, the optimization can be performed over four design variables instead of nine. This dimensional reduction is significant as the optimization takes place on the finely discretized workspace. A brute force search is conducted for the four design variables over a finely discretized workspace of the abduction/adduction and flexion/extension DoF. The translational of the mechanism is set to a typical operating point, while pronation/supination rotation is kept constant, since this rotation is only due to the serial part of the hybrid 3RPS-R mechanism. At each discrete point in the workspace, inverse kinematics of the parallel device is invoked to calculate the angular travel at the spherical joints and to check if the physical limits are violated.

Constrained optimization is carried out in a serial fashion, in partic-

ular, once the angular travel of the admissible grid points are calculated in the brute-force search, an elimination process is carried out according to the singularity free zone. Afterwards, two objectives functions considered as the outcome of the optimization, the first objective function is the workspace volume attained, while the maximum RoM along the flexion/extension DoF is considered as the second objective function. Normalization and aggregation of the cost functions are not required, since there exits no trade-off between them.

In other words, for each parameter set, natural physical limitations of spherical rolling joints are used as hard-stops in order to keep the movement of robot within the singularity-free zone while obtaining the maximum volume index and flexion/extension span. Result of the constraint optimization problem indicates that the offset orientations that yield the largest workspace volume also maximize RoM along the flexion/extension DoF, while satisfying the abduction/adduction RoM and singularity constraint. The optimal offset angle are calculated as $\Xi_{1_2} = 35°$, $\Xi_{2_1} = 10°$, $\Xi_{2_2} = 30°$ and $\Xi_{2_3} = 20°$, respectively.

For validation, the workspace of the 3R$\underline{\text{P}}$S-$\underline{\text{R}}$ mechanism before and after the optimization are compared in Figure 2.15. Singular configurations for optimal offset angles are also marked. It can be immediately observed from the figure that, proper offsetting at the connection points results in a four fold increase in the mechanism workspace, as well as two fold increase in the RoM along the flexion/extension and abduction/adduction DoF, while staying withing the feasible space.

If the spherical joints that have higher swing capabilities are chosen in the implementation, it is possible to obtain further increased singularity-free workspace volume as shown with red dots in Figure 2.15.

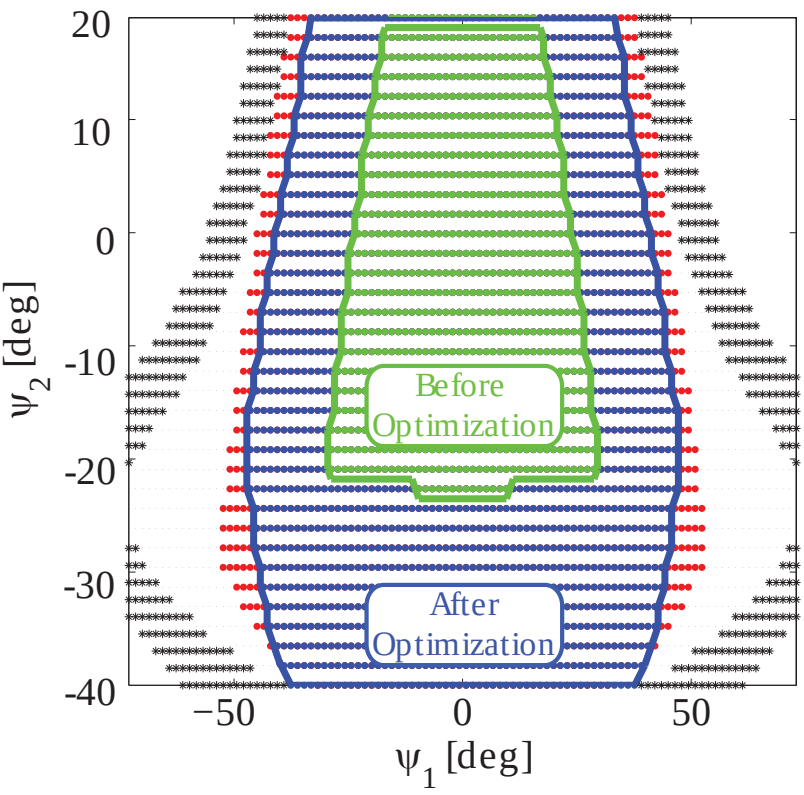

Figure 2.15: Workspace of the 3RPS-R mechanism before and after the optimization

2.6.3 Characterization

One of the most important characteristics for any force-feedback device is its bandwidth. The parallel kinematic structure of the 3RPS-R mechanism can achieve high stiffness with low apparent inertia, and along with the direct drive actuation a relatively high bandwidth is expected. To measure the bandwidth of the 3RPS-R prototype, its Bode magnitude plot is experimentally determined under closed-loop position control as presented in Figure 2.16. From this Bode plot, the closed-loop position bandwidth of the device is measured to be 80 *Hz*.

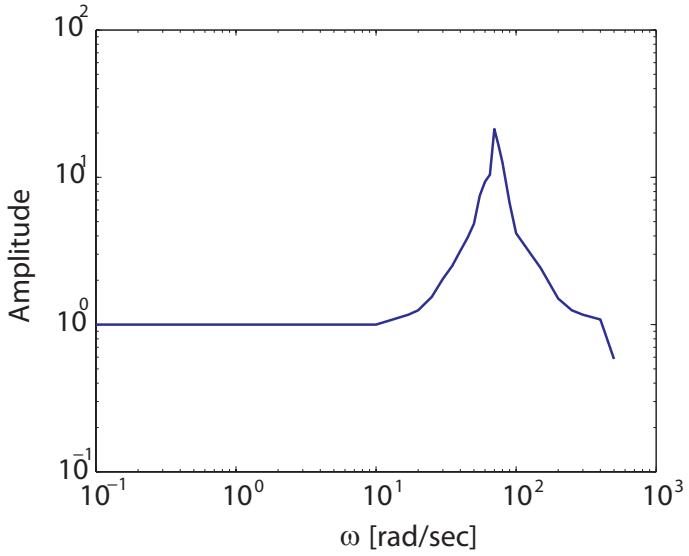

Figure 2.16: Bode magnitude diagram for the 3RPS-R exoskeleton under closed loop position control

The peak instantaneous and peak continuous force the mechanism can provide are expected to cover an acceptable portion of force/torque limits of a patient. The forearm-wrist exoskeleton is actuated by three direct-drive linear motors and one DC motor, whose maximum instantaneous forces/-torques are 52 N and 2.5 Nm, respectively. The maximum continuous forces/torques are given by 12 N and 0.184 Nm. Since there is a 24.5 capstan ratio associated with the DC motor, its corresponding values are scaled by that ratio. The mapped end-effector maximal values are then found to be: (Continuous) $\tau_{\psi_1} = 2.175\ Nm, \tau_{\psi_2} = 1.51\ Nm, \tau_{\psi_3} = 4.5\ Nm, F_z = 33.04\ N$; (Instantaneous) $\tau_{\psi_1} = 9.43\,Nm, \tau_{\psi_2} = 6.56\,Nm, \tau_{\psi_3} = 55.86\,Nm, F_z = 149.1\,N$.

To instill safety precautions, the mechanism is desired to be easily moved both in forward and backward directions along each degree of freedom, even when the controllers are turned-off. This back-driveability requirement has been addressed in design by preferring direct-drive actuation, such that the only burden to be overcome by the operator during

slow motions is due to the Coulomb friction. Low Coulomb friction values are desired to achieve back-driveability as well as to ensure good performance using model based controllers. The experiments to measure the back-driveability of the mechanism concluded that the minimum forces/-torques in the end-effector coordinates with which the associated degree of freedom can be moved are as follows: $F_z = 2.1\ N, \tau_{\psi_1} = 2 \times 10^{-3}\ Nm, \tau_{\psi_2} = 1e^{-3}\ Nm, \tau_{\psi_3} = 0.1\ Nm$.

An ideal force-feedback device is desired to withstand human applied forces with very high stiffness and be capable of displaying a full range of impedances down to the minimum value human can perceive. The performance of the exoskeleton under closed loop control is strongly affected by the apparent inertia of the device. The inertia of the device results in parasitic effects on the displayed impedances and deteriorate the transparency of force-feedback. Hence, independent of the control algorithm used, it is beneficial to decrease the inertia of the exoskeleton. Since the inertia matrix is dependent upon the configuration of the robot, average constant apparent inertia matrix of the device is estimated by commanding the robot to trace a complex trajectory and averaging the inertia matrices calculated throughout all these configurations. The singular values of this inertia matrix, characterizing the "presence" of the robot at each degree of freedom, are determined respectively as: $\sigma_{\psi_3} = 48587\ kgmm^2$, $\sigma_{\psi_2} = 216.3\ kgmm^2$, $\sigma_{\psi_1} = 140.6\ kgmm^2$, $\sigma_z = 2.4\ kg$.

Another widely accepted metric to characterize the performance of force feedback devices is the highest stiffness value (stiffest virtual wall) that can be stably rendered without introducing artificial damping. The stability limit for stiffness rendering is experimentally determined through controlling the impedance of the mechanism and introducing higher and

higher stiffness values until the system goes unstable. The instability is observed to occur at a value of $k = 2.114 \times 10^4\ N/m$ along the z-direction; while the rotational stiffness values are measured as $\psi_1 = 65\psi_2 = 60\psi_3 > 100\ Nm$.

Although the dynamic performances mentioned so far are important for the mechanism, for a rehabilitation device, the range of motion of the mechanism may be the most valuable criteria. The reason is that, after an injury, the human wrist loses its original range of motion (RoM) which can only be regained by proper exercises. If the mechanism does not cover a large portion of this RoM, then it is impossible to prescribe those motions. As a result, the space spanned by the mechanism has to be tested and ensured to conform with typical human kinematics presented in Table 2.1. For the 3RPS-R mechanism, the movement along the z-direction is only activated to adjust the mechanism such that proper arm length for any given patient is achieved. Therefore, the critical degrees of freedom are ψ_1 and ψ_2, since ψ_3 can already cover the whole rotational workspace of the human forearm along its medial axis. These essential degrees of freedom are tested by a controlled discovery experiment at a predefined translational and pronation/supination values. The results are then compared with simulation results as presented in Figure 2.17.

A summary of the characterization results for the 3RPS-R exoskeleton prototype is given in Table 2.3.

2.7 Discussion

In this chapter, a systematical design process for a forearm and wrist rehabilitation robot is presented, while keeping faithful to the design requirements of such a mechanism throughout the process, especially complying

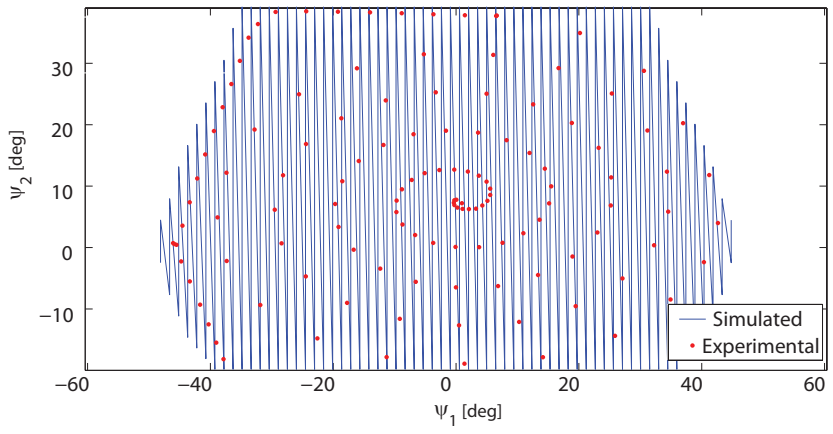

Figure 2.17: Verification of the orientation (ψ_1 vs. ψ_2) workspace of the 3RPS-R platform of the forearm-wrist exoskeleton

with the imperative ones that are safety and ergonomy of the user as one would expect in this application.

2.7.1 Type Selection

Type selection contributes for the most part of the ergonomic use, firstly by the choice of 3RPS-R parallel structure which provides passive coincidence between user and robot joint axes. Moreover, this particular kinematics provides translational DoF through forearm rotation axis that not only can be utilized for ease-of-attachment therefore eliminating the need of additional adjustments for each user, but also enables the implementation of novel rehabilitation therapy schemes which includes medial forces that pull/push wrist tendons during rotational movement similar to an isotonic exercise [20, 67].

Although it is simplified as a rotational DoF in majority of the wrist rehabilitation research, kinematics of the wrist rotations are quite complex, in particular, the two axes of rotation do not necessarily appear to be mutually perpendicular and translation may occur along these rota-

Table 2.3: Experimental characterization of the 3RPS-R forearm-wrist exoskeleton

Criterion	ψ_1	ψ_2	ψ_3	z	3RPS-R
Peak Inst. Force	9.43 [Nm]	6.56[Nm]	55.86 [Nm]	149.1 [N]	–
Peak Cont. Force	2.175 [Nm]	1.51 [Nm]	4.5 [Nm]	34.42 [N]	–
Inertia Matrix Singular Values	140.6[kg-mm^2]	216.3 [kg-mm^2]	48587 [kg-mm^2]	2.4 [kg]	–
Back-driveability	2 $\times 10^{-3}$ [Nm]	1 $\times 10^{-3}$ [Nm]	0.12 [Nm]	2.1 [N]	–
Virtual Wall Rendering	65 [Nm]	60 [Nm]	>100 [Nm]	2.114 $\times 10^4 [N/m]$	–
Workspace Coverage	-47 to 47 [deg]	-20 to 40 [deg]	-90 to 90 [deg]	125 to 160 [mm]	–
Position Bandwidth	–	–	–	–	80 Hz

tional axes as shown in literature [91]. Therefore, using a pure rotational movement for administering flexion/extension and radial/ulnar deviation exercises may result in discomfort, necessitating soft couplings between the operator and the end-effector. The chosen kinematic chain, however, provides an additional advantage; the translational movement in the longitudinal axis of the forearm. To elaborate, a simplified simulation similar to the work done by Esmaeili *et al.* [92] is performed. Utilizing a similar structure for wrist biomechanics, resultant error vector between E_{hand} and E_{exo} can give kinematic mismatch value under the exact amount of actuation of human flexion/extension, radial/ulnar deviation movements and Ψ_1, Psi_2 rotations of exoskeleton. The offset value between two axes of rotation in hand kinematics Λ is varied between -16 to 16 mm range, in which 3RPS-R chain with optimized translational value decreases the

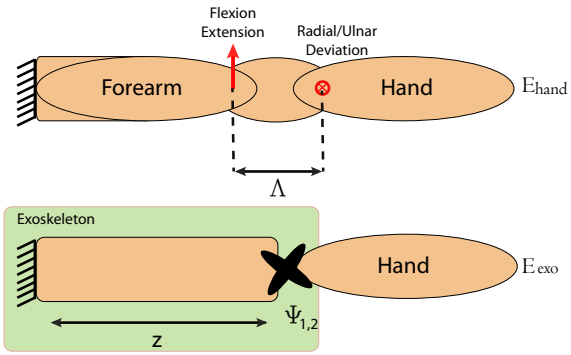

Figure 2.18: Functional diagram of the wrist and exoskeleton. Joint offset Λ is typically between -16 and 16 mm.

kinematic mismatch at the end-effector 71 ∓ 7 % with respect to a universal joint implementation, which result in the same amount of mismatch as the offset value. Resultant error vector between exoskeleton end-effector and simplified human model is given in Figure 2.19.

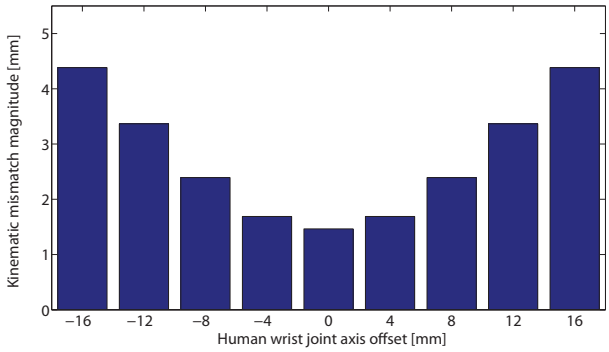

Figure 2.19: Kinematic mismatch magnitude at the end-effector during different offset between rotational axes of flexion/extension and radial/ulnar deviation.

2.7.2 Optimal Dimensional Synthesis

Afterwards, dimensional synthesis of the mechanism is performed which aims to increase the performance of the device during human-in-the-loop controls. In this multi-criteria optimization, optimized parameters is as important as the cost functions chosen, especially joint connection angle determination makes the process more complicated as the system becomes asymmetric for most of the parameter range. This necessitates additional singularity analysis, which in the end showed that making the system asymmetric not only alters the singular configurations drastically, but also results in additional singular configurations based on the Grassmann conditions which are not geometrically possible in symmetric case, regardless of the fact that these points lie in the unreachable workspace of the mechanical implementation. However, making the final design asymmetric while using open ring structure for base and end-effector, wearability of the device is eventually improved.

The choice of the optimization metrics, on the other hand, is majorly based on the final performance of the device in control implementations. One of the prominent characteristics of such a device is its actuator utilization and stiffness that is emphasized in increased isotropy index though AII. Moreover, decreasing GDI further benefit the controller performances through the elimination of the deteriorating affects of the device mass as well as increasing stiffness rendering bandwidth [80] which would be useful during the implementation of the therapeutic exercises and with applications based on tele-operation [81].

It should be noted that optimization procedure implemented in this chapter is a general tool, which can be used for different mechanisms at varying haptic tasks. Moreover, it enables a quantitative yet subjective

comparison, since, changing emphasis in normalization matrices as well as optimal objective functions would alter the results. However, for the given task and chosen kinematic structure, it is believed that simulation and experimental characterization results would provide evidence to the necessity of such an optimization for improved mechanical performance.

In other words, the emphasis in this framework is not on the magnitude of improvements with the chosen performance metrics or normalization matrices, but the necessity of such fore-thoughtful procedure in design steps.

2.7.3 Characterization

Experimental characterization of the device shows that final mechanism is capable of implementing a broad range of haptic tasks with its high bandwidth and low end-effector inertia. Coupled with the results of high force output at the end-effector, it can be argued that optimization metrics chosen for this tasks and improvements in these directions are more than adequate, while the device is capable of rendering stiff and accurate impedances even under open loop impedance controller. This also partially justifies proposed approach in the procedure which emphasizes the choice of design goals based on possible control implementations.

2.7.4 Comparison with RiceWrist

The chosen kinematic structure enables a unique perspective with the ability to compare the outcomes of this systematical optimization with respect to the previous implementations of RiceWrist in literature. However, the optimization procedure summarized above is built upon a different base radius due to manufacturing concerns, which in result would alter the

fairness of a direct comparison, especially in dimensional optimization. In order to tackle that, same optimization procedure is performed based on the parameters of RiceWrist, where, it is shown that using the same normalization matrices in subsection 2.5.3, the corresponding point for the enhanced RiceWrist [51] is sub-optimal, in particular, it has a normalized $\bar{\text{AII}}$ value of 0.4342, about 17% worse than normal to the Pareto curve in this axis. It has a normalized $\bar{\text{GDI}}$ value of 0.3987 about 32% worse than normal to the Pareto curve in GDI axis as shown in Figure 2.20.

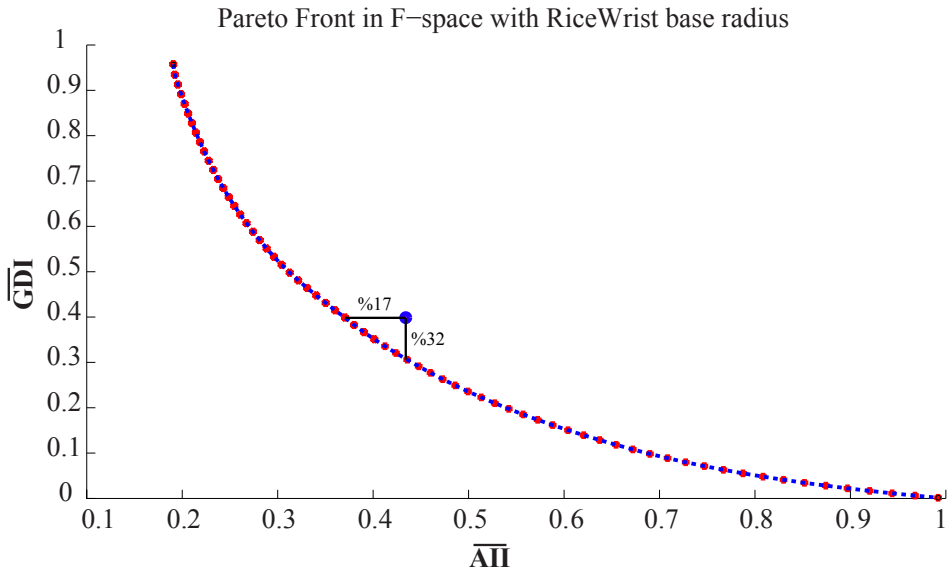

Figure 2.20: Pareto-front curve of $\mathcal{A}\bar{\mathcal{I}}\mathcal{I}$ vs $\mathcal{G}\bar{\mathcal{D}}\mathcal{I}$

Regarding the workspace coverage of both mechanisms, a simpler comparison can be performed based on two rotational DoFs in parallel structure. Compared to enhanced Ricewrist [93] version which also incorporates spherical rolling joints, range of motion in flexion/extension is increased %127 while both mechanisms are able to cover the active range of motion of human operator for radial/ulnar deviation.

The choice of this particular mechanical structure enables a direct com-

parison with a previously presented RiceWrist, therefore emphasizing the need of incorporating performance requirements into the design process. Modifications over the similar kinematic structure can be summarized as:

- Dimensional optimization in order to increase the efficiency of the device in actuator utilization and control bandwidth.
- Workspace optimization with physical limits of joints included.
- Computationally efficient kinematic model derivation and singularity analysis with Grassmann line geometry in order to exhibit the robustness of the mechanism.
- Improved ergonomy and ability to be worn with minimal assist via optimal non-symmetric design and unclosed base.
- Implementation with control performance and rehabilitation requirements in mind, in particular, by using linear actuators as prismatic joints to ensure high back-driveability and actuator stiffness while incorporating spherical rolling joints for limited but singularity free workspace.
- Derivation of the dynamic model and implementation of model-based controllers such as task space impedance controller with gravity compensation.
- Extensive dynamic and kinematic performance characterization in order to validate the outcomes of optimizations.

Finally, a controller implementation for any device should be consistent with the natural end-effector space of the mechanism. In case of forearm and wrist rehabilitation, it is consisting of three consequent/concurrent

complex rotations which can be faithfully represented as **SO**(3). Previous literature on pointing tasks with forearm and wrist movements shows that for small orientations a projection to R^3 may be viable but deviations start to occur for larger and more complex rotations.

Chapter II

3 Human-in-the-Loop Control of Forearm-Wrist Exoskeleton

For the ultimate goal of “hospitals without borders", controllers implemented on a rehabilitation protocol should consider both the local control schemes for single robot interacting with the patient and controllers for multiple robots interacting with each other and the patient. Multiple robot control would enable tele-rehabilitation, where different operation modes would give rise to remote diagnosis, group therapies and bimanual exercises. Local controllers on each site; however, should be designed separately. This section starts with the summarization of these local rehabilitation controller implementation. Second subsection focuses on the multi-site controller design.

3.1 Local Control

Human forearm-wrist facilitate a complex motion of the hand. In particular, neglecting the small deviations of the axes of rotation during the movement, the simplified kinematics of the human forearm and wrist can be quite faithfully modeled as a three DoF kinematic chain that allows supination/pronation of the forearm, flexion/extension and ulnar/radial deviation of the wrist joint with a coinciding axes of rotation. Hence, unlike the reaching-type translational movements in the three dimensional

Euclidian space, the the rotations of the forearm and the wrist can be more properly studied in a 3-dimensional manifold, $\mathbf{SO}(3)$.

Implementation of the controllers for wrist rehabilitation therapies focuses on different aspects of recovery and finally aiming functional improvements in the patient's life. One of the techniques implemented is range of motion exercise in which the therapist determines the desired orientations and asks the patient to move his/her wrist between these two orientations. The therapist supervises over the rehabilitation trial and gives assistance if the patient is unable to accomplish the given task. In order to implement such therapies in robot assisted rehabilitation, interpolation between these desired orientations is needed and linear interpolation does not guarantee smooth motion in $\mathbf{SO}(3)$. After a proper timed trajectory is created between these orientations, assistance should be provided to the patient in different intensities. In early phases of rehabilitation, patients are unable to exert enough forces to complete the given task, therefore, a position controller can be used for passive motion along the desired path. In order to implement the position control law, however, an error metric should be defined with proper rotational representation.

Any rotation in $\mathbb{R}^3$ can be represented with Euler parameters (unit quaternions) which lie on a hyper-sphere of dimension three $\mathbf{S}^3$. This representation is more effective in handling composition of rotations, in addition to its relatively better numerical stability. Because of these advantages, quaternion rotations are widely used in robotics analysis [94]. Lack of representation singularities while using Euler parameters encourages researchers to also utilize quaternion rotations for controls. In the literature, definition of orientation error within the unit quaternion space as well as implementation of position and impedance controls using Euler

parameters have been addressed [95, 96]. In [97, 98], physically consistent stiffness matrices for impedance control are derived from energy functions, thanks to consistent representation of rotations over the task geometry.

This enables the implementation of a common method of providing assistance, that is to administer virtual tunnels to avoid undesired regions in the workspace using impedance control. With virtual tunnels, patients are allowed to move freely as long as they do not violate the bounds defining forbidden regions. However, since virtual tunnels provide only spatial assistance, they cannot assist patients along the contour or ensure that the desired motion is traced within a pre-determined amount of time. Thus, virtual tunnels are commonly augmented with a moving window. With moving windows, the pace of the patient along the contour is regulated so that the patient is not allowed to fall behind a margin of the predefined timing [99, 100, 101]. However, evidence exist in motor learning literature that virtual tunnels may have negative efficacy on human learning as the participants become dependent on existence of such assistance to complete the task [102]. In particular, patients may start to depend on the border of the virtual walls and/or the moving window to help them complete the task. For more adept assist-as-needed implementations, utilization of time-optimal trajectories calculated for point-to-point reaching movements together with adaptive control techniques that penalize the deviation from that optimal trajectory has been proposed [103]. Such controllers allow more freedom in choosing the movement path compared to virtual tunnel approaches, these methods are still- based on trajectory tracking. It should be noted that multi degrees of freedom therapeutic exercises are contour following tasks where coordination and synchronization between various degrees of freedom are imperative, while exact timing along the path is

not critical. Unfortunately, use of assist-as-needed protocols which rely on minimization of trajectory tracking error cannot guarantee that patients are always on the pre-determined path due to the radial reduction phenomena [104, 105]. Moreover, the discrepancy between tracking error and contour error becomes more critical when humans are in the loop. For instance, if the patient slows his/her progress on the desired contour, the reference point calculated by time parametrization of the trajectory tracking controller continues to advance regardless of the patient's progress, resulting in a significant deviation from the trajectory, causing possibly large contour errors.

Among the available contour tracking algorithms, passive velocity field control (PVFC) is of particular interest, since this method not only minimizes the contour error but also does so by rendering the close loop system passive with respect to externally applied forces. PVFC concept has been first proposed as a part of a smart exercise protocol in [106] and further analyzed in [107, 108]. Later, PVFC has been adapted to bilateral control [109, 110]. In [111], the controller has been further extended to include shaping of the potential energy of the closed loop system dynamics as well as its kinetic energy. Finally, in [112], a PVFC controller that operates solely on joint positions has been proposed, alleviating the need for velocity measurements. We have previously analyzed passive velocity field control for robotic rehabilitation [77] and proposed an online velocity field generation algorithm that relies on fewer state variables [113].

In PVFC, the task to be performed and speed of the task are decoupled from each other. In particular, the task is embedded in a predefined velocity field while the speed depends on the instantaneous energy of the closed loop system. For example, for human-in-the-loop contour following tasks,

a predefined velocity field encodes the path to be followed, while the initial energy of the system and the work done by the human operator on the system dictates the speed of motion. PVFC mimics the dynamics of a flywheel; hence cannot generate energy, but can store and release energy supplied to it. As a consequence, the controller renders the close-loop system passive with respect to externally applied forces. This is one of the unique features of PVFC approach, as classical passivity-based robot control laws [114, 115, 116] cannot guarantee passivity when external forces are considered as the input. Passivity with respect to external forces is crucial in human-machine interaction, since it enhances safety by limiting the amount of energy that can be released to the operator, especially in case of an unexpected system failure.

3.1.1 Timed Trajectory Generation and Position Control in SO(3)

One of the major protocols in wrist rehabilitation involves orientation exercises, in which therapist specifies a target orientation for the patient to reach. During traditional rehabilitation, the therapist guides the patient to the target orientation in a proper way, by suppressing undesired deviations form a smooth path and by providing assistance as needed. In robot-assisted rehabilitation, a smooth path between the current orientation and target orientation must be constructed through interpolation. Once such a path is determined, assistance can be provided to the patient in the form of virtual tunnels (forbidden regions on the orientation space) and force fields along the desired path.

In this work, SLERP (Spherical Linear Interpolation) is utilized to form the desired path between given orientations of forearm-wrist. In particular, since the metric topology on the space of rotations is topologically different

from the usual topology on $\mathbb{R}^3$, the shortest path between two orientations is not simply the linear interpolation between the coordinates of the local chart that locally maps $\mathbf{SO}(3)$ to $\mathbb{R}^3$. Instead, as the topology of $\mathbf{SO}(3)$ is the quotient topology of $\mathbf{S}^3$ with the equivalence relation that identifies the two antipodal points as equivalent, the shortest path between two orientations is a great arc – or a *geodesic* on the three sphere. As a result, a walk along the shortest path, on the $\mathbf{SO}(3)$ manifold, between the two orientations can be properly achieved using SLERP. When Euler parameters are used to interpolate between two rotations, this geodesic lies on a 4-dimensional unit sphere [117].

The workspace of 3RPS-R is the product space $W = \mathrm{R}\times \mathbf{SO}(3)$. Casting aside the translational degree of freedom for the moment, suppose two orientations of the end-effector, $p, q \in \mathbf{S}^3$ are given. Let $h \in [0, 1]$. Then the spherical linear interpolation is equivalently given by the following formula:

$$SLERP(\underline{\boldsymbol{p}}, \underline{\boldsymbol{q}}, h) = \underline{\boldsymbol{p}}(\underline{\boldsymbol{p}}^* \underline{\boldsymbol{q}})^h \tag{3.1}$$

$$SLERP(\underline{\boldsymbol{p}}, \underline{\boldsymbol{q}}, h) = (\underline{\boldsymbol{p}}\underline{\boldsymbol{q}}^*)^{1-h} \underline{\boldsymbol{q}} \tag{3.2}$$

$$SLERP(\underline{\boldsymbol{p}}, \underline{\boldsymbol{q}}, h) = (\underline{\boldsymbol{q}}\underline{\boldsymbol{p}}^*)^h \underline{\boldsymbol{p}} \tag{3.3}$$

$$SLERP(\underline{\boldsymbol{p}}, \underline{\boldsymbol{q}}, h) = \underline{\boldsymbol{q}}(\underline{\boldsymbol{q}}^* \underline{\boldsymbol{p}})^{1-h} \tag{3.4}$$

The fact that SLERP yields a great arc interpolation on $\mathbf{SO}(3)$ is far from obvious. It can be proven considering the fact that a curve is a great arc if and only if the second derivative vector is parallel and opposite in direction to the position vector of the curve. Not only does SLERP produce minimum distance curves between two points in $\mathbf{SO}(3)$, but also those curves have constant speed. This follows from the fact that minimum distance curves

are geodesics on the underlying manifold which can be proven to have constant speed.

After the construction of the desired path based on pre-defined points, a position controller should be designed on $\mathbf{SO}(3)$, therefore necessitating a quaternion based error metric, in order to ensure that patient tracks the given path correctly. For that purpose, let $\underline{Q_d} = \{\epsilon_{4d}, \boldsymbol{\epsilon}_d\}$ and $\underline{Q_e} = \{\epsilon_{4e}, \boldsymbol{\epsilon}_e\}$ represent the quaternions associated with R_d and R_e, respectively. The subscripts d and e stand for desired and actual values, respectively. The orientation error can be described by the rotation matrix $\mathrm{R}_d\mathrm{R}_e^T$, which yields the identity map when the the two frames are aligned. Using quaternion algebra, the orientation error may also be expressed in terms of the quaternion $\Delta\underline{Q} = \{\Delta\eta, \Delta\xi\}$, where

$$\Delta\underline{Q} = \underline{Q_d}\,\underline{Q_e}^{-1} \tag{3.5}$$

$\Delta\underline{Q} = \{1, \mathbf{0}\}$ holds if and only if R_e and R_d are aligned. Therefore, the orientation error can be defined as

$$\underline{\mathbf{e_O}} = \Delta\boldsymbol{\epsilon} = \epsilon_{4e}\,\boldsymbol{\epsilon}_{4d} - \epsilon_{4d}\boldsymbol{\epsilon}_{4e} - \mathbf{S}(\boldsymbol{\epsilon}_{4d})\boldsymbol{\epsilon}_{4e} \tag{3.6}$$

where the skew-symmetric operator $\mathbf{S}(\cdot)$ has been used. It should be kept in mind that ϵ_{4e} and $\boldsymbol{\epsilon}_e$ cannot be actually measured. Thus, they must be derived from the rotation matrix R_e which is available from the manipulator kinematics.

When the position error metric is defined as in Eqn. (3.6), a PD control is used in task space with a control force given as

$$\mathbf{F} = K_D\,\boldsymbol{\Delta\omega} + K_P\,\underline{\mathbf{e_O}} \tag{3.7}$$

where $\Delta\omega = \omega_d - \omega_e$ is the angular velocity error vector, while K_D and K_P are the derivative and position gain matrices, respectively. Desired orientations are given by the therapists and quaternion parameters for these points are recorded. Afterwards, an online generation of the path between these orientations is validated with the help of SLERP algorithm.

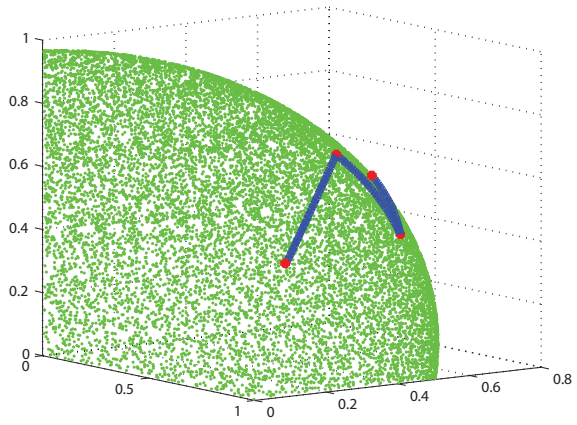

Figure 3.1: SLERP finds the shortest path between any two quaternion on the unit sphere.

In order to visualize the desired orientations of the end-effector, a unit vector is rotated with interpolated values and these points are plotted in Figure 3.1. Smooth motion between desired orientation points (shown with red asterisks) can be observed on the unit sphere (green dots).

After desired position of the end-effector is calculated, a task space position controller is implemented. To implement the controller the position error as well as the angular velocity difference are utilized as proposed in [94, 97]. Convergence of the end effector frame with desired frame is shown with four quaternion parameters in Figure 3.2 with a root mean square (RMS) tracking error value for $\underline{\mathbf{e_O}}$ (Eqn. (3.6)) is $[0.0035, 0.0061, 0.0057]^T$ rad and the percentage of RMS value with respect to the maximum position

value is [%0.0208, %0.0530, %0.0306].

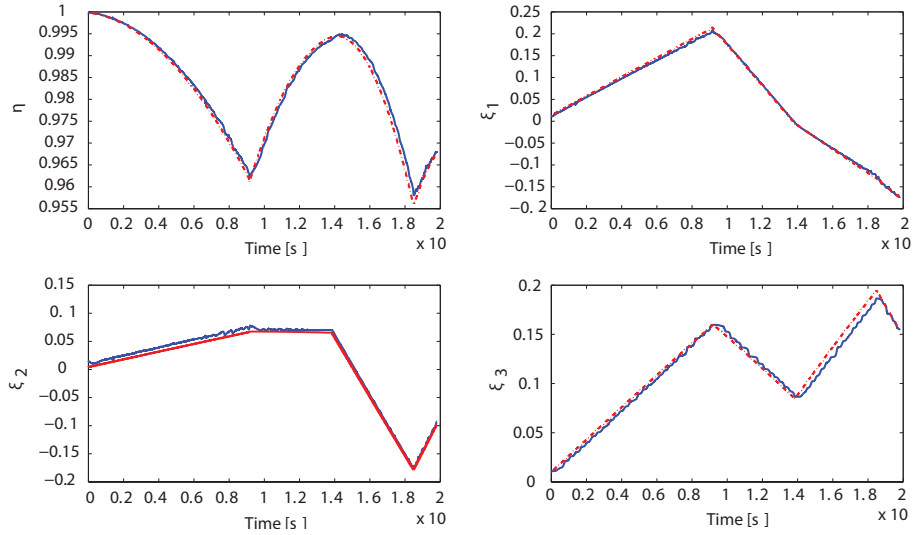

Figure 3.2: Actual end-effector orientation and the reference values

3.1.2 Impedance Control in SO(3)

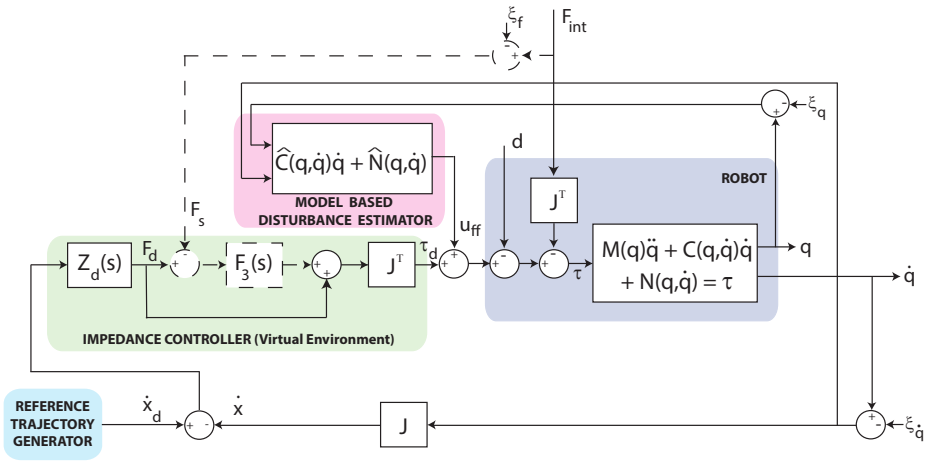

Figure 3.3: Block diagram of the impedance control algorithm

Figure 3.3 presents the block diagram of a generic impedance controller. The impedance controller typically works in the task space, since assigning impedances in joint space is rather counter-intuitive. Keeping in mind

that the encoders sense the joint coordinates, implementation of the controller in the task space necessitates the knowledge of the mapping (the Jacobian, J) from joint forces/torques to end-effector forces/torques for the mechanism under consideration. To faithfully assign desired decoupled impedance values Z_d along each separate DoF of the device, model-based dynamics cancellation is utilized. The equations of motion is derived using Kane's method with nominal plant parameters. However, uncertainties associated with the plant parameters render it implausible to exactly cancel the system dynamics. Thus, the best effort towards that goal is pursued by using the nominal plant parameters represented by $\left(\hat{\mathrm{C}}(\mathbf{q}, \dot{\mathbf{q}}), \hat{\mathrm{N}}(\mathbf{q}, \dot{\mathbf{q}})\right)$, standing for Coriolis/centripetal and gravity terms, in Figure 3.3. Once the desired impedances along each DoF are multiplied by the corresponding position/velocity error, the desired end effector forces/torques are obtained. The error between the desired and the actual force to implement the force control scheme is only possible with force sensors; however, these sensors are expensive and relatively hard to integrate in rehabilitation applications. As a result, open-loop impedance control is implemented and the force controller term $F_3(s)$ is taken to be zero. For the 3R$\underline{\mathrm{P}}$S-$\underline{\mathrm{R}}$ forearm-wrist rehabilitation robot, haptic rendering of the forces arising from interactions with the virtual environment can be best displayed utilizing an impedance controller. To render physically meaningful impedances, the control must be implemented in the task-space, which lives in $\mathbf{SO}(3)$. Geometrically consistent impedances in $\mathbf{SO}(3)$ can only be rendered, if the orientation error is defined properly [118, 119].

Using the error metric defined in Eqn. (3.6) and relative angular velocity, a rotational impedance can be generated resulting a torque value τ:

$$\tau_{\mathbf{d}} = \mathbf{J}^{\mathbf{T}} \left(\mathrm{D}_o \, \Delta\boldsymbol{\omega} + \mathrm{K}'_o \, \mathbf{e_O}\right) \tag{3.8}$$

where $\mathbf{J^T}$ is the transpose of the analytical Jacobian matrix and $K'_o = 2\mathbf{E}^T(\eta_{DE}, \xi_{\mathbf{DE}}K_o)$ is the stiffness matrix derived from energy arguments [98]. Note that the above equations are valid for open-loop implementation of impedance controller, that is, when force feedback is not available during the implementation. An open-loop impedance controller is preferred since addition of force sensors into rehabilitation devices is of high cost and challenging. Moreover, thanks to the highly-back-driveable, low impedance design of the wrist rehabilitation robot, parasitic effects of device dynamics on the rendered impedance can be kept at a negligible level.

In order to demonstrate the haptic rendering performance of the mechanism under open loop impedance control, an experiment is conducted which renders a constant impedance (to be more specific, the stiffness) is rendered with 3R$\underline{\text{P}}$S-$\underline{\text{R}}$ around $\mathbf{n_1}$ and $\mathbf{n_2}$ axes, as shown in Figure 3.4 and 3.5, respectively. A moment is created with different loads located 70 mm away from the center of rotation, resulting in forces that varies up till 0.8 Nm torque about the both axes. The torsional stiffness for all principal axes are set to be 1 Nm/rad. RMS error value of the rendered impedance values are calculated to be %0.6 and %0.5 verifying the fidelity of the rendered impedance. The parameter uncertainties in the plant model are the source of small steady state errors observed in the plots.

3.1.3 Passive Velocity Field Control Implementation

Given a smooth path between the current and target configurations, virtual tunnels may be employed in order to restrict large deviations of the patient from the desired path. However, for patients with limited ability to control their limbs, further assistance is required to ensure their completion of the path following task. The way that such assistance is provided is a crucial

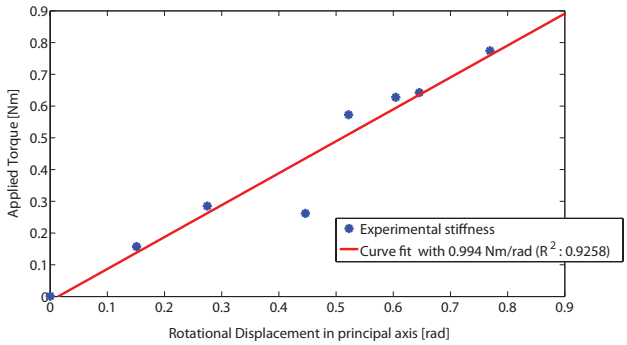

Figure 3.4: Impedance values for the rotations around the principal axis covering radial/ulnar deviation

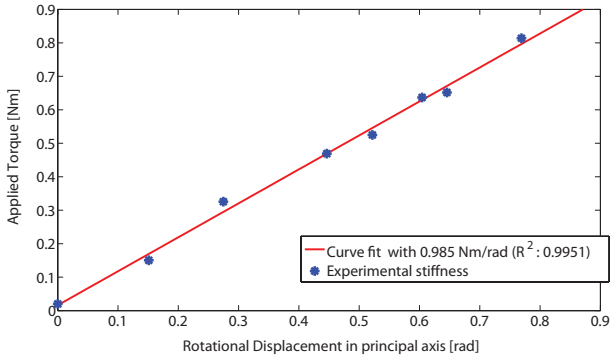

Figure 3.5: Impedance values for the rotations around the principal axis covering flexion/extension

aspect of robot-assisted therapy that strongly affects its efficacy.

Use of PVFC in rehabilitation robotics is advantageous in various ways: First of all, the control law ensures passivity with respect to external torque inputs, an asset no other passivity-based controllers with trajectory tracking objective can achieve. Indeed, this property of the control law ensures no harm be done on the patient should a given trajectory cannot be tracked. Specifically, given the dynamics of the manipulator defined in task space as

$$\mathrm{M}(\mathbf{q})\ddot{\mathbf{q}} + \mathrm{C}(\mathbf{q}, \dot{\mathbf{q}})\dot{\mathbf{q}} = \boldsymbol{\tau} + \boldsymbol{\tau}_e \tag{3.9}$$

where $\mathrm{M}(\mathbf{q}) \in \mathbb{R}^{n \times n}$ is the inertia matrix, $\mathrm{C}(\mathbf{q}, \dot{\mathbf{q}}) \in \mathbb{R}^{n \times n}$ is the Coriolis matrix, $\boldsymbol{\tau}$ represents control forces, and potential forces are embedded in the external force $\boldsymbol{\tau}_e$, PVFC renders the controlled manipulator as a dynamic nonlinear impedance that can store and release the energy supplied to it. Thanks to this property, the control law guarantees passivity with respect to the supply rate $s(\tau_e, \dot{q}) = \boldsymbol{\tau}_e{}^T \dot{\mathbf{q}}$, that is, it ensures passivity with respect to external force inputs $\boldsymbol{\tau}_e$, implying

$$\int_0^t \boldsymbol{\tau}_e{}^T \dot{\mathbf{q}}\, d\tau \geq -c^2 \tag{3.10}$$

where c is some real number.

Secondly, the control law minimizes the "contour error" rather than the more conventional trajectory error. Minimizing the contour error, defined as the closest path (in the proper space) from the actual position of the manipulator to the desired contour, is advantageous since such a control technique guarantees minimal deviations from the desired path, while trajectory error based controllers can largely deviate from the path as the trajectory tracking error is dictated by time parametrization [120]. In

particular, the desired task and the speed of task execution are decoupled in PVFC. For instance, for a contour following task, the desired path is encoded into the velocity field, so that for each location of the robot end-effector, a proper reference trajectory can be calculated, while the controller ensures that the velocity of the robotic manipulator converges to a scaled multiple of this desired velocity in the absence of external forces: Formally, the controller guarantees that for any initial condition $(\mathbf{q}(\mathbf{0}), \dot{\mathbf{q}}(\mathbf{0}))$, there exists a constant $\rho > 0$ s.t.

$$\lim_{t \to \infty} \dot{\mathbf{q}}(t) - \rho \mathrm{V}(\mathbf{q}(t)) = 0. \tag{3.11}$$

when $\boldsymbol{\tau}_e \equiv 0$. Note that the parameter ρ dictates the speed of task execution and can be positive or negative.

Finally, in the PVFC architecture, the amount of assistance can be adjusted and same path can be traced forward and backwards, and at different speeds by simply tuning the controller parameters. Specifically, the magnitude of ρ is governed by the instantaneous energy of the system; hence, can be adjusted either by changing the initial conditions of the system or through external forces doing (possibly negative) work on the system. This implies, for contour following tasks, the desired path can be traced forwards and backwards, and at different speeds by simply tuning the instantaneous energy of the system through controlled variables.

Given a desired velocity field, the control specifications are satisfied by introduction of an extra state, which may be interpreted as the velocity of a fictitious flywheel of mass M_F that augments the original system as an extra energy storage element. Then the kinetic energy function for the

augmented system is defined as

$$\bar{k}(\bar{\mathbf{q}}, \dot{\bar{\mathbf{q}}}) = \frac{1}{2}\dot{\bar{\mathbf{q}}}^T \bar{\mathrm{M}}(\bar{\mathbf{q}})\dot{\bar{\mathbf{q}}}. \tag{3.12}$$

where $\bar{\mathrm{M}}$ denotes the inertia matrix of the augmented system, $\bar{\mathbf{q}}$ and $\dot{\bar{\mathbf{q}}}$ represent the augmented configurations and velocities, respectively. The desired velocity field is also extended to encompass the extra state such that when it (or a multiple of it) is exactly tracked, the kinetic energy of the augmented system remains constant, that is

$$\bar{k}(\bar{\mathbf{q}}, \bar{\mathbf{V}}(\bar{\mathbf{q}})) = \frac{1}{2}\bar{\mathrm{V}}(\bar{\mathbf{q}})^T \bar{\mathrm{M}}(\bar{\mathbf{q}})\bar{\mathrm{V}}(\bar{\mathbf{q}}) = \bar{E} > 0 \tag{3.13}$$

Given an augmented velocity field, the skew-symmetric control law is calculated using two terms which are analogous to feed-forward dynamic compensation and a feedback term forces the error dynamics to converge as

$$\bar{\boldsymbol{\tau}}(\bar{\mathbf{q}}, \dot{\bar{\mathbf{q}}}) = \underbrace{\frac{1}{2\bar{E}}(\bar{\mathbf{w}}\bar{\mathbf{P}}^{\mathbf{T}} - \bar{\mathbf{P}}\bar{\mathbf{w}}^{\mathbf{T}})}_{\text{skew symmetric}}\dot{\bar{\mathbf{q}}} + \sigma \underbrace{(\bar{\mathbf{P}}\bar{\mathbf{p}}^{\mathbf{T}} - \bar{\mathbf{p}}\bar{\mathbf{P}}^{\mathbf{T}})}_{\text{skew symmetric}}\dot{\bar{\mathbf{q}}} \tag{3.14}$$

where $\sigma \in \mathbb{R}$ in Eqn. (3.14) is a control gain, not necessarily positive, which determines the convergence rate and the sense in which the desired velocity field will be followed. In Eqn. (3.14), $\bar{p}$ denotes the momentum of the augmented system, while $\bar{P}$ is the desired momentum of the augmented system. The symbol $\bar{w}$ represents the inverse dynamics necessary to follow

the desired velocity field. Mathematically,

$$\bar{\mathbf{p}}(\bar{\mathbf{q}}, \dot{\bar{\mathbf{q}}}) = \bar{\mathrm{M}}(\bar{\mathbf{q}})\dot{\bar{\mathbf{q}}} \tag{3.15}$$

$$\bar{\mathrm{P}}(\bar{\mathbf{q}}) = \bar{\mathrm{M}}(\bar{\mathbf{q}})\bar{\mathbf{V}}(\bar{\mathbf{q}}) \tag{3.16}$$

$$\bar{w}(\bar{\mathbf{q}}, \dot{\bar{\mathbf{q}}}) = \bar{\mathrm{M}}(\bar{\mathbf{q}})\dot{\bar{\mathbf{V}}}(\bar{\mathbf{q}}) + \bar{\mathrm{C}}(\bar{\mathbf{q}}, \dot{\bar{\mathbf{q}}})\bar{\mathbf{V}}(\bar{\mathbf{q}}) \tag{3.17}$$

In [107], it has been proven that the skew symmetric control law coupled with the skew symmetry property of the robotic manipulators renders the closed-loop system passive with respect to external force inputs and regulates the error dynamics to zero (exponentially) in the absence of external forces. Moreover, it has been shown that the total energy in the system defined by Eqn. (3.12) remains constant (as long as no work is done on the system by external forces) and the rate at which the parameterized trajectory progresses is determined by the instantaneous energy of the system. The reader is referred to [107, 108, 121] for stability proofs, robustness analysis and detailed convergence characteristics of PVFC.

During physical implementations of the controller, the energy level may vary due to inevitable dissipative forces, such as friction in the joints. Under such circumstances, a nominal rate at which the parameterized trajectory progresses may be dictated by adding an exogenous signal to $\bar{\tau}$ as

$$\tau_{forced} = \varsigma\, \bar{\mathbf{P}}\left(r - \frac{\bar{\mathbf{P}}^T\, \dot{\bar{\mathbf{q}}}}{2\bar{E}}\right), \quad \varsigma > 0 \tag{3.18}$$

where ς is a damping coefficient. It can be shown that τ_{forced} causes the velocity $\dot{\bar{q}}$ to converge to $r\bar{\mathrm{V}}$.

Construction of Velocity Field in SO(3)

Even though existence of a velocity field encoding the task is a crucial part of PVFC, determination of such a velocity field is not a trivial matter. One effective method attacks the velocity field generation problem from a controls perspective and designs controllers for online generation of the vector field [121]. In particular, in [121] Li *et al.* has proposed a technique for encoding velocity fields for parametric curve tracking, based on state suspension and self-pacing. The approach is similar to use of navigation functions for path planning [122] and is implemented by introducing two new states (curve parametrization τ and its time derivative $\dot{\tau}$) to the system dynamics (called suspension) and controlling these states using properly defined error functions and potential fields. To ensure good tracking performance, $\dot{\tau}$ is continually adjusted with respect to the rate of convergence (self-pacing).

In particular, let the desired orientation trajectory be represented by parameterized trajectory $x_d : \mathcal{I} \to \mathcal{G}$ where $\mathcal{I} \in \mathbb{R}$. The workspace of 3R$\underline{\text{P}}$S-$\underline{\text{R}}$ is **SO**(3), with each element q identified with a 3×3 real orthogonal matrix with determinant one. T_q **SO**(3) can be identified with $\{q\,\omega : \omega \in \mathbf{so}(3)\}$ where **so**(3) is the space of 3×3 skew symmetric matrices. Then an error function can be defined by

$$E(q, x_d) = q x_d^{-1}(\tau) = q x_d^{T}(\tau) \tag{3.19}$$

where $x_d : \mathcal{I} \to \mathbf{SO}(3)$ is the parameterized trajectory. Following [123], a potential function over **SO**(3) is then defined as follows. Let $P \in \mathbb{R}^{3\times3}$ be a symmetric matrix with distinct eigenvalues $\lambda_1 < \lambda_2 < \lambda_3$ and $(\lambda_1 + \lambda_2)(\lambda_1 +$

$\lambda_3)(\lambda_3 + \lambda_2) \neq 0$. Then:

$$U(E) = \frac{1}{\lambda'} trace\,[\mathrm{P}\,(\mathrm{I} - \mathrm{E})] \tag{3.20}$$

where $\lambda' = \lambda_2 + \lambda_3 - \lambda_1$ and I is the 3×3 identity matrix defined a potential function U in $\mathbf{SO}(3)$ and $\mathrm{E} \in \mathbf{SO}(3)$ is a critical point of $U(\cdot)$. Furthermore, $\mathrm{E} = \mathrm{I}$ is the only critical point of U at which U has a positive definite Hessian, that is, U has a minimum [124].

Note that, since $\mathrm{x_d}(\tau) \in \mathbf{SO}(3)$, there exists $\Omega : \mathcal{I} \rightarrow \mathbf{so}(3)$ so that

$$\frac{d}{d\tau}\mathrm{x_d}(\tau) = \mathrm{x_d}(\tau)\Omega(\tau) \tag{3.21}$$

Then, following [121], the desired velocity field $V : \mathbf{SO}(3) \times \mathcal{I} \rightarrow T\mathbf{SO}(3) \times T\mathcal{I}$ can be derived as:

$$\mathrm{V}(\bar{\mathrm{q}}) = \gamma_1(\bar{q}) \begin{pmatrix} \mathrm{E}(\bar{\mathrm{q}})\mathrm{x_d}(\tau)\Omega(\tau) \\ 1 \end{pmatrix} - \gamma_2(\bar{q}) \begin{pmatrix} \frac{1}{2\lambda'}(\mathrm{EPE} - \mathrm{P})\mathrm{x_d}(\tau) \\ 0 \end{pmatrix} \tag{3.22}$$

$$= \gamma_1(\bar{\mathrm{q}}) \begin{pmatrix} \mathrm{q}\Omega(\tau) \\ 1 \end{pmatrix} - \frac{\gamma_2(\bar{q})}{2\lambda'} \begin{pmatrix} \mathrm{q}\left[\mathrm{x_d}(\tau)^{\mathrm{T}}\mathrm{Pq} - \mathrm{q}^{\mathrm{T}}\mathrm{Px_d}(\tau)\right] \\ 0 \end{pmatrix} \tag{3.23}$$

Note that the speed of progression of the desired parameterized contour relative to the rate of convergence is determined by the relative magnitudes of $\gamma_1(\bar{q})$. *Self-pacing* exploits this relationship to yield better contour following characteristics. In particular, $\gamma_1(\bar{q})$ and $\gamma_2(\bar{q})$ are made to depend on the potential function $U(E(q, \tau))$ which measures the deviation of the current configuration from the desired location, so that when $U(E)$ is large, the velocity field prioritizes decreasing the tracing error. Consequently, when the tracking error is large, the desired trajectory x_d would progress

Figure 3.6: Left figure presents the flight simulator, in which the movements of the plane is coupled to the rotations of the 3RPS-R end-effector. Right figure depicts cross section of tunnel on which virtual walls and velocity field are depicted schematically.

at a slower speed. For instance, $\gamma_1(\bar{q})$, $\gamma_2(\bar{q})$ can be chosen as:

$$\gamma_1(\bar{q}) = \exp\left(-\nu\, U(\mathrm{E}(\mathrm{q}, \beta))\right) \tag{3.24}$$

$$\gamma_2(\bar{q}) = 2 - \exp\left(-\nu\, U(\mathrm{E}(\mathrm{q}, \beta))\right) \tag{3.25}$$

where $\nu > 0$ is the self-pacing parameter such that as ν increases, the emphasis on eliminating contour following error is also increased.

Coupling with Virtual Reality

Virtual environment simulations with force-feedback are integrated in rehabilitation protocols not only for more engaging therapies, but also for ensured safety and ease modification of task parameters. Furthermore, force-feedback is indispensable for immersion and to have meaningful interactions with the virtual environment.

For the 3RPS-R forearm-wrist rehabilitation robot, a flight simulator is implemented for visual representation (see Figure 3.6). The plane is

coupled to the end-effector of 3R$\underline{\text{P}}$S-$\underline{\text{R}}$ and possesses the same metric space with the task space of the mechanism, that is, yaw-pitch-roll motions of the end-effector are mapped to same rotations of the plane. The task is to move the plane through a curved tunnel with a predetermined forward speed.

Force feedback is provided to the patient through implementation of a virtual tunnel coinciding with the visual representation of the tunnel and through PVFC guiding the patient within virtual tunnel. In particular, virtual tunnel defines forbidden regions in the workspace, by rendering a high stiffness "virtual wall" in the ϵ-neighborhood of the desired path. The virtual wall is implemented as cubic-damped spring using task space impedance control with orientation error metric. For patients with limited ability to control their limbs, PVFC is implemented inside the virtual tunnel to assist patient with completion of the task. In particular, a parameterized representation of the centerline defining the tunnel is used to construct the frame of the curve, which governs the desired orientation along the tunnel. Then, a velocity field in $\mathbf{SO}(3)$ is constructed using suspension and self-pacing as discussed previously.

Type and power of the assistance may be customized with control parameters of the coupling controller (3.14), and exogenous signal (4.10), as well as velocity field generation parameters (equations (3.24) and (3.25).

Experiment Results

Implementation of the controller is realized with the help of a desktop computer equipped with an I/O card running Quarc 2.0 on Matlab. Controllers are programmed in C for real-time implementation and the sampling frequency is set to 500 Hz. Since only position measurements are available

via the encoders situated on the actuators, velocities are calculated using a nonlinear estimator based on the adaptive identification method, in an effort to reduce the numerical noise due to differentiation.

PVFC has been implemented for the 3RPS-R exoskeleton to minimize the "contour error" defined in **SO**(3). For simplicity, the desired path is parameterized by two sinusoids along ψ_1 and ψ_2 axes. This path does not impose any rotation about ψ_3. The initial conditions of the mechanism was intentionally offset from the desired configuration. Figure 3.7 presents contour tracking performance of the controller. Noting that when $\psi_3 = 0$, gravity field creates a moment in the positive ψ_2 direction, the tracking performance is quite satisfactory along both ψ_1 and ψ_2 axes. Slight overshoot can be observed on the ψ_2 axes due to unmodeled dynamics in the feed-forward gravity compensation.

Figure 3.8 depicts the convergence characteristics and the total kinetic energy of the controlled system. The convergence is measured using the metric defined on **SO**(3), as given in equation 3.20. Exponential decay of the error metric can be observed within the first few instants of the experiment, while the convergence metric is kept near zero throughout the experiment. The kinetic energy of the augmented system is observed to decrease marginally due to friction inherent to the system. However, the rate of this decrease is low. If desired, extra energy can be introduced to the system via a feed-forward force. In this demonstration, no exogenous force is applied to the system.

3.2 Multilateral Control

The forearm-wrist exoskeleton can also be adapted as a part of a rehabilitation system that implements the multi-lateral shared control concept

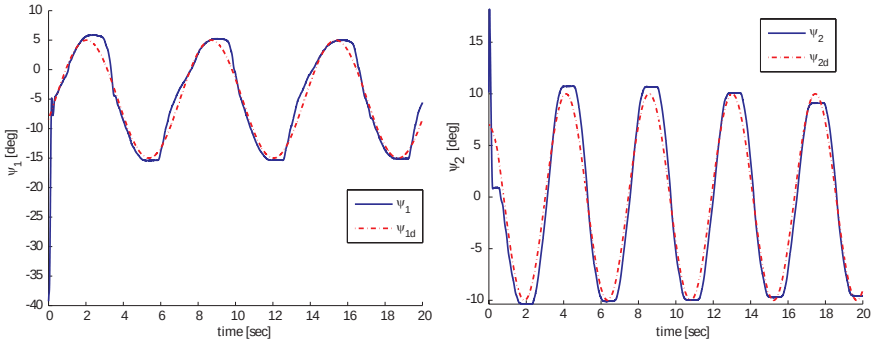

Figure 3.7: Path following under PVFC

for rehabilitation. The multi-lateral shared control architecture allows for multiple agents (patients and therapists or patient using both limbs, paralytic limb (PL) and uninjured limb (UL)) to simultaneously interact while performing a (virtual) therapeutic task [125]. Through a dominance factor, different control authority could be assigned to each agent such that patient can guide himself or the therapist can guide the patient. The goal of a multilateral rehabilitation system is to implement a control architecture so that multiple agents (for example both limbs of a patient; PL, UL and a dynamic virtual reality) can work collaboratively to achieve certain therapeutic tasks; for instance, to perform manipulation tasks in a dynamic virtual environment. Since the paralytic limb of the patient is deprived of the necessary neuromuscular activity to overcome even a resistive task; let alone a dynamic one, uninjured limb should start off as the dominant factor in the collaborative task. As recovery of the patient takes place, the power distribution should gradually revert and the PL should be able to cope with the task. Note that this method is different than other bimanual therapy studies that depend on the mirror image concepts and provide a non-significant level of improvement in the literature [126, 127, 128, 129, 130].

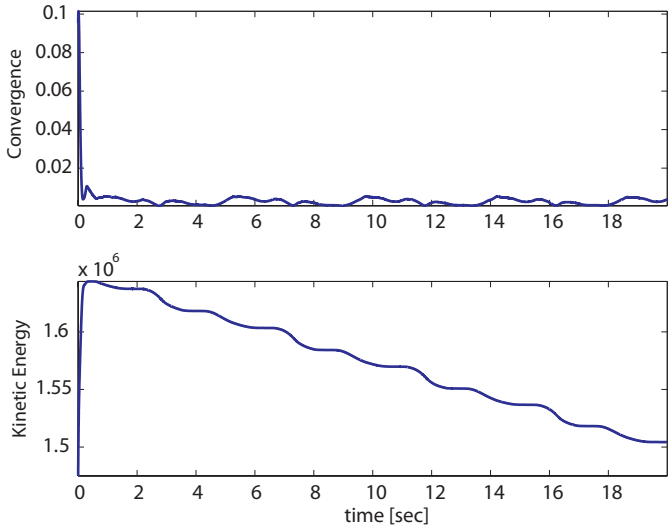

Figure 3.8: Convergence metric and kinetic energy of the augmented system

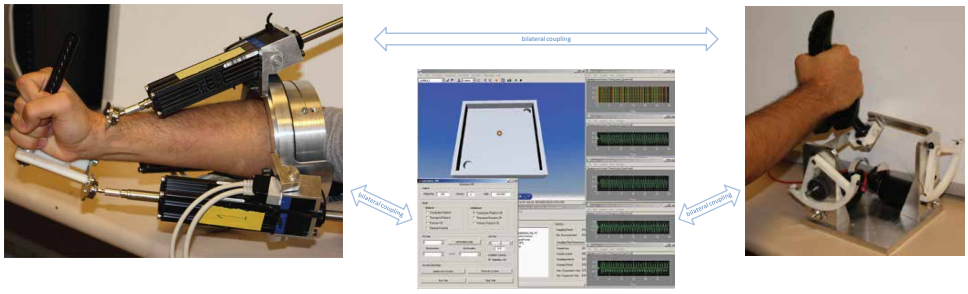

Figure 3.9: The forearm-wrist rehabilitation system

The virtual task should be modeled and executed as a dynamic simulation. Regarding the controller design, stability (through passivity) should be guaranteed rather than rendering perfect transparency of forces. Since all of the controllers are proposed to be implemented and run on the same computer, stability deterioration due to time delays introduced by the communication channels can be kept negligibility small.

3.2.1 Multi-lateral Controller for Dual-User Bilateral Tele-operation

The dual-user bilateral tele-operation concept [125] extends upon the traditional bilateral tele-operation techniques, in that, it uses a distribution parameter ϖ, so called the dominance factor, that dictates the degree of contribution of each master over the slave. In agreement with the literature, small signal linearization is implemented and the operators and the environment are modeled to possess linear and time-invariant dynamics about the equilibrium configurations. The operators and the environment are also assumed to be passive. The stability of the overall system is guaranteed ensuring passivity of the controllers, since the observability conditions are satisfied. In the discussion to follow, the subscripts p and

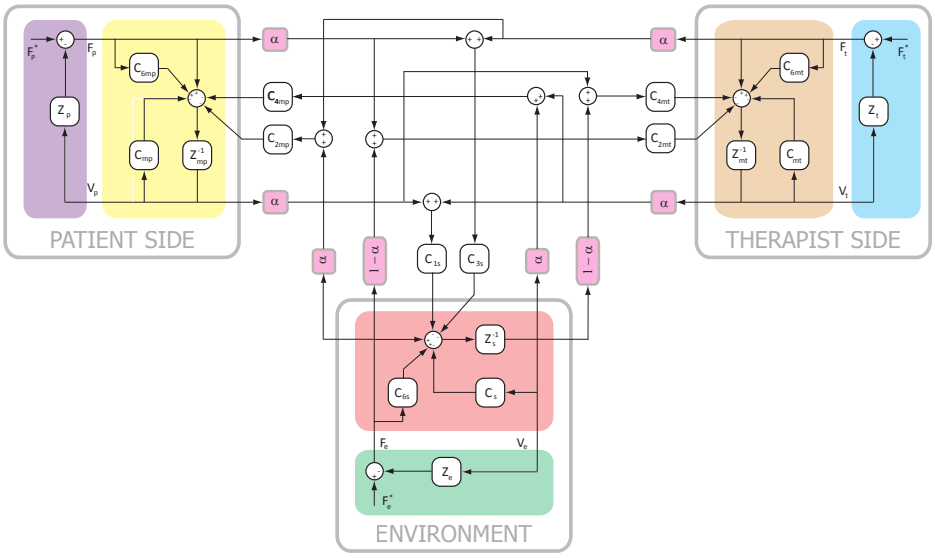

Figure 3.10: Block diagram of the multi-lateral tele-operation controller

t represent the patient and the therapist, respectively. The slave environ-

ment is denoted by the subscript e. Following relations hold for the system

$$\mathbf{F_p} = \mathbf{F_p^*} - Z_p \mathbf{V_p} \tag{3.26}$$

$$\mathbf{F_t} = \mathbf{F_t^*} - Z_t \mathbf{V_t} \tag{3.27}$$

$$\mathbf{F_e} = \mathbf{F_e^*} + Z_e \mathbf{V_e} \tag{3.28}$$

where $\mathbf{F_p^*}$, $\mathbf{F_t^*}$, and $\mathbf{F_e^*}$ denote the external inputs from the two operators and the slave, respectively. The external slave input will be taken to be zero, as rehabilitation task is a passive dynamic simulation. The symbols Z_p, Z_t, and Z_e denote the impedances of the masters, the slave and the virtual environment, following the LTI model convention. Utilizing the local controller introduced in the previous subsection, the masters are bestown linear dynamics which can be modeled as with the control inputs $\mathbf{F_{ctrl}}$, a combination of the local controllers and the communication channel controllers given in Figure 3.10

$$\mathrm{M_p}\dot{\mathbf{V}}_\mathbf{p} = \mathbf{F_p} + \mathbf{F_{ctrl}^p} \qquad \mathbf{F_{ctrl}^p} = -C_p \mathbf{V_p} + C_{6_p}\mathbf{F_p} - C_{4_p}\mathbf{V_p^d} - C_{2_p}\mathbf{F_p^d} \tag{3.29}$$

$$\mathrm{M_t}\dot{\mathbf{V}}_\mathbf{t} = \mathbf{F_t} + \mathbf{F_{ctrl}^t} \qquad \mathbf{F_{ctrl}^t} = -C_t \mathbf{V_t} + C_{6_t}\mathbf{F_t} - C_{4_t}\mathbf{V_t^d} - C_{2_t}\mathbf{F_t^d} \tag{3.30}$$

$$\mathrm{M_s}\dot{\mathbf{V}}_\mathbf{e} = -\mathbf{F_e} + \mathbf{F_{ctrl}^e} \qquad \mathbf{F_{ctrl}^s} = -C_s \mathbf{V_e} + C_5\mathbf{F_e} + C_1\mathbf{V_e^d} + C_3\mathbf{F_e^d} \tag{3.31}$$

where the superscript, d denotes the corresponding desired signal. Local controllers C_{mp}, C_{mt}, C_s are the impedance controllers without the inertial terms, since it is not practical to obtain noise-free acceleration signals without introducing additional sensors. To achieve good transparency the communication channel gains are selected as $C_{1s} = C_s$, $C_{4_{mp}} = -C_{m_p}$, and $C_{4_{m_t}} = -C_{m_t}$.

The effect of the dominance factor ω is obviated with the following

velocity and force definitions:

$$\mathbf{V_p^d} = \varpi\mathbf{V_e} + (1-\varpi)\mathbf{V_t} \qquad \mathbf{F_p^d} = \varpi\mathbf{F_e} + (1-\varpi)\mathbf{F_t} \tag{3.32}$$

$$\mathbf{V_t^d} = (1-\varpi)\mathbf{V_e} + \varpi\mathbf{V_p} \qquad \mathbf{F_t^d} = (1-\varpi)\mathbf{F_e} + \varpi\mathbf{F_p} \tag{3.33}$$

$$\mathbf{V_e^d} = \varpi\mathbf{V_p} + (1-\varpi)\mathbf{V_t} \qquad \mathbf{F_e^d} = \varpi\mathbf{F_p} + (1-\varpi)\mathbf{F_t} \tag{3.34}$$

To elucidate the primary aim of the application, consider what is expected to happen when the dominance factor ϖ is zero. Then $\mathbf{V_t^d} = \mathbf{V_e}$, $\mathbf{F_t^d} = \mathbf{F_e}$ and $\mathbf{V_e^d} = \mathbf{V_t}$, $\mathbf{F_e^d} = \mathbf{F_t}$. Assuming the second operator to be the therapist, the resistance offered by the environment is overcome solely by the therapist in this case. Similarly, when $\varpi = 1$, all the effort is burdened on the patient. In between the two values, the load is split between the therapist and the patient. The lower the dominance factor, the lower the effort exerted by the patient.

3.2.2 Experimental Results

An experiment is conducted using the rehabilitation system depicted in Figure 3.9. The virtual task is to direct a ball into the two holes diagonally placed at the two corners of the table. The task is to be fulfilled collaboratively by the patient and the therapist. The therapist uses the two DoF force-feedback joystick whose axes are made to coincide with those of 3R$\underline{\text{P}}$S-$\underline{\text{R}}$ and the table in the virtual environment. The joystick is locally impedance controlled and coupled to the virtual task and the therapist through the multi-lateral control architecture. The arm of the patient is placed in the 3R$\underline{\text{P}}$S-$\underline{\text{R}}$ exoskeleton whose two relevant DoF are coupled to the joystick and the virtual environment, while the remaining two DoF are set-point position controlled to restrict undesired movements. In particular, the medial axis rotation of the forearm is constrained by the motor,

while the linear motion along the z-axis is first adjusted according to the arm length of the user, and is then constrained by the linear actuators. The rest of the DoF are locally impedance controlled and are coupled to the virtual task and the therapist through the multi-lateral control architecture. In

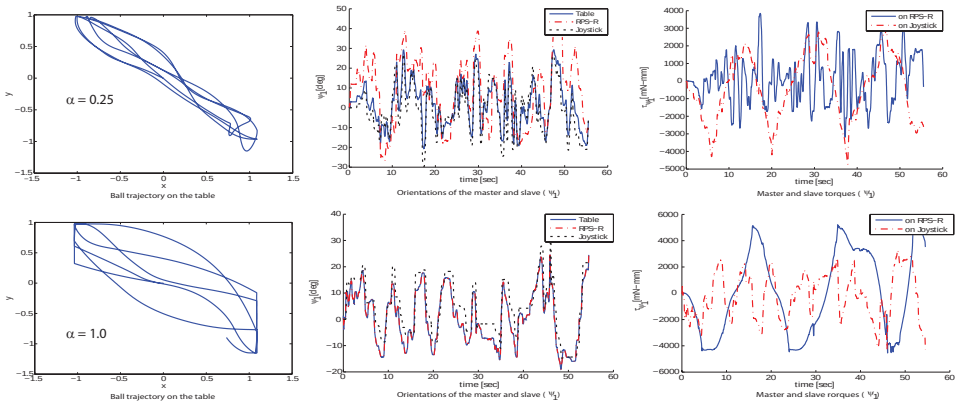

Figure 3.11: Experimental multi-lateral control performance for different control authorities. Ball trajectory, orientation of table and torques applied are provided for $\varpi = 0.25$ (Top column) and $\varpi = 1$ (Bottom Column)

Figure 3.11, the top row and bottom row present the experimental results for $\varpi = 0.25$ and $\varpi = 1.0$, respectively.The first column of figures depict the trajectory of the ball on the table. From these plots, it can be observed that $\varpi = 1.0$ produces a smoother ball movement than that of $\varpi = 0.25$. The reason is that when ϖ is not 0 or 1, commands given by the patient and the therapist may conflict resulting in such hesitant ball trajectories.

The second column of figures represent the orientation of the table, 3RPS-R, and the joystick about their first axis. Observe that when $\varpi = 1.0$, the table exactly follows 3RPS-R. The joystick, being coupled to these two systems, follows this trajectory imposed by the patient with some error. This distinction is not so clear when $\varpi = 0.25$, since both the therapist and the patient can command their own trajectories. However, observe that since $\varpi = 0.25$ implies that the therapist is thrice more dominant than the

patient, and the table follows the joystick more closely than the 3R$\underline{P}$S-$\underline{R}$.

The last column of figures are total torques applied on the 3R$\underline{P}$S-$\underline{R}$ and the joystick about the first axis. The increased frequency of the oscillations when $\varpi = 0.25$ is in parallel with the non-smoothness of the ball trajectories shown in the top figures. This is due to the fact that both users are able to affect the orientation of the table and may impose motions conflicting each other, leading to more frequent changes of applied torque direction to compensate for errors with respect to their desired ball trajectories. When $\varpi = 1.0$, there remains only one master, who can command the ball without experiencing any coupling forces from the other master, and as a result no such high frequency torque fluctuations are observed.

Chapter IV

4 Effective Delivery Framework for Therapeutic Exercises

Once design and implementation of controllers for the mechanism is completed, a framework that incorporates these building blocks and determines the structure of the session (e.g. repetition number, assistance level, speed of the task, type of exercise...) should be defined. The proposed framework for robotic rehabilitation should not only enable the changes supervised by the therapist, but also deliver the basic outlines of a traditional therapy session without endangering the safety of the patient. In particular, the exercise sessions should be repetitive and intense; assistance should be provided to the patient just enough to make the task completable so that active involvement of the patient should always be encouraged. Furthermore, using the activities of the daily living makes it easier to port the recovery obtained in laboratory environments to real-life applications. It should also be noted that coordination and synchronization of multiple DoF system is more essential than the exact timing along the desired path, therefore, a therapy routine resembles more of a contour tracking task.

Providing a rehabilitation framework that inherits all these qualities is not trivial, especially despite some of human motor control properties which are beneficial in our daily lives but could hinder the outcomes

of therapeutic exercises. One major challenge is prevention of slacking, specifically, the continuous decrease in the levels of muscle activation during repetitive motions as the movement error becomes small. Although it can be beneficial for implementations of orthosis since it enables a more effective coupling between the user and the robot, controllers should be designed in a way that patient cannot rely on the robot to complete task in order to achieve active participation of the patients in rehabilitation exercises. Modeling of this slacking property along with some compensation techniques have presented in the literature. In [131], authors have proposed using a reducing force term with a time constant implemented through an adaptive controller to provide assistance as needed. In this controller, the assistance force decays as the error in task execution becomes small. With the help of this forgetting factor, overall controller architecture enables compensation against the slacking characteristics of human motor control; letting the patient 'take over' most of the physical effort required to complete the movement. Motivated by the findings of this experiment, several computational models of slacking have been proposed in [132].

Preliminary experiments have been conducted in [133] to implement the minimum assistance concept in rehabilitation. In these experiments, the chosen pattern of assistance has been shown to display a less-than-linear increase for small errors, thus facilitating the emergence of active un-aided control at the end of training; for large errors, that are likely to occur at the beginning of training, the assistance grows more than linearly in order to speed up the learning process. Moreover, difficulty of the given task is increased if the performance of the patient is adequate. Difficulty is adjusted through the frequency of the given movement. In [134], authors have also incorporated an adaptive gain value for the force fields which

reduces the gain if the previous checkpoints are successfully accomplished in a trajectory tracking exercise.

Unlike these ad-hoc methods, PVFC controller tackles the problem more systematically and can compensate for slacking without sacrificing the passivity of the controller. With PVFC, the complexity of the given task can be changed based on not only the frequency of the movement but the energy of the overall system or the velocity field generated over the desired contour can be modified to result in more difficult tasks [113]. Measuring the performance of the patient online rather than between trials or at check points can be achieved trivially with the closest point algorithm presented in [113]. Moreover, PVFC can accomplish slacking prevention passively, a property that cannot be assured with any of the ad-hoc compensation methods.

4.1 Online Velocity Field Generation of Parametric Curves

In this subsection, passive velocity field generation for parametric curves is summarized. Even though existence of a velocity field encoding the task is a crucial part of PVFC, determination of such a velocity field is not a trivial matter. In most of the previous studies simple contours, such as lines and circles, are used so that the contour error can be calculated analytically [135, 136]. In [137], generation of velocity fields for generic parametric surfaces is studied and a method for off-line calculation of velocity fields using pre-selected grids is proposed.

Alternative methods attack the velocity field generation problem from a controls perspective and design controllers for online generation of the vector field [121], as previously utilized for 3RPS-R device in Chapter II. In particular, in [121] Li *et al.* has proposed a technique for encoding

velocity fields on the configuration manifold for parametric curve tracking, based on state suspension and self-pacing. The approach is similar to use of navigation functions for path planning [122] and is implemented by introducing two new states (curve parametrization τ and its time derivative $\dot{\tau}$) to the system dynamics (called suspension) and controlling these states using properly defined error functions and potential fields. To ensure good tracking performance, $\dot{\tau}$ is continually adjusted with respect to the rate of convergence (self-pacing).

In this subsection, an alternative approach to online generation of velocity fields for parametric curves is presented. In particular, utilizing a feedback stabilized closest point tracking algorithm for real-time determination of the contour error [138, 139, 140] is proposed and for online construction of the velocity field. This algorithm is similar to the state suspension approach in [121], since it also uses a feedback controller. The uniformly asymptotically stable controller updates the location of closest point on the curve to continually track the end-effector of the robot. However, this approach is different in in various ways: First of all, the configuration error is calculated directly at the task space. The controller introduces only a single new state, the variable that parameterizes the curve, and updates this state without any need for pre-determined error and potential functions. Since the implementation of controller simply requires evaluation of a point on the curve and its unit tangent, the approach is computationally efficient. Furthermore, thanks to its feedback-stabilized core, the algorithm is immune to initialization errors, and robust against drift and numerical noise. Additionally, the algorithm is generalizable to generate vector fields for parametric surfaces, allowing tasks in which end-effector motion needs to be restricted to move on a surface (instead of

a curve) be implemented with the PVFC approach.

4.1.1 Real-Time Determination of the Contour Error

The core idea of the closest point tracking algorithm is demonstrated on a smooth planar curve depicted in Figure 4.1. Let s be the path length parameter and $\mathbf{f}(s)$ represent the parametric curve C. At any parameter value s, the curve $\mathbf{f}(s)$ maps to a point in space. Let $\hat{\mathbf{f}}_s(s)$ denote the unit tangent vector at s. Then, the unit normal $\hat{\mathbf{n}}(s)$ at s can be calculated by taking the cross product of the unit tangent vector with the unit vector $\hat{\mathbf{k}}$, which points out of the plane. The algorithm is founded on the fact

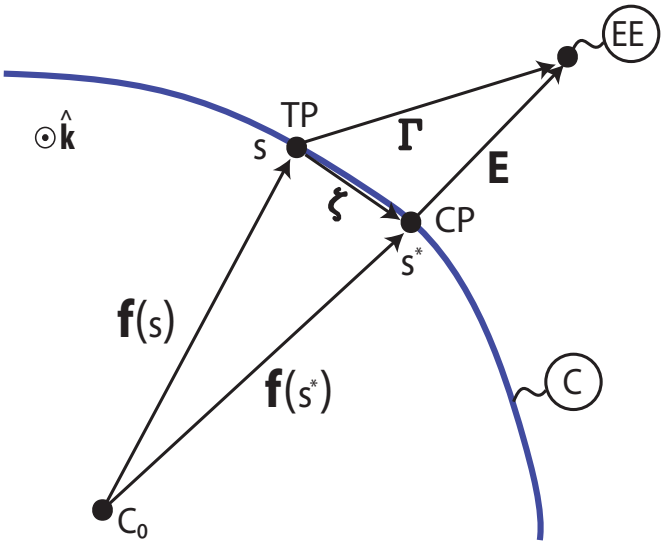

Figure 4.1: Feedback-stabilized closest point tracking algorithm

that the vector $\mathbf{E}$ connecting the closest point to the end-effector (EE) is perpendicular to the surface tangent at the closest point. Convergence is achieved utilizing a feedback controller that checks for this condition at each instant of time and continually updates the location of a test point (TP) until it converges to the closest point. In particular, given a test point on the parametric curve, the algorithm forms the vector $\mathbf{\Gamma}$ initiating at

test point and extending to the end-effector. The projection error Ψ is calculated by projecting the $\mathbf{\Gamma}$ vector on the unit tangent vector evaluated at the test point. Then, the controller updates the location of the test point by determining its speed of movement along the curve, that is, by setting $\dot{s}_{TP}$, to drive the magnitude of the error vector ζ to zero. More formally, the following theorem can be stated for a 'nice' rigid convex regular parametric curve C parameterized by its path length s. A curve is defined as 'nice' if unit normals evaluated at any two different points on the the curve are not collinear. Let ϵ be a small positive constant, κ represent curvature, $\bar{\Gamma}$ and $\bar{v}$ be upper bounds on magnitude of $\mathbf{\Gamma}$ and ${}^{C}\mathbf{v}^{EE}$ vectors, respectively. $(.)^{*}$ denotes quantities evaluated at the closest point. All the vectors are represented by boldface while standard fonts are used for their magnitudes.

Theorem 1 *If the image of the mapping* $\mathbf{f}(s) : [0, l] \rightarrow \Re^2$ *defines a 'nice' rigid convex regular parametric curve C, EE is in the Voronoi region of C, EE is in continuous relative motion* ${}^{C}\mathbf{v}^{EE}$ *with respect to C, and the controller gains satisfy* $K_1 > \frac{2\bar{\Gamma}\bar{v}}{\epsilon^2}$ *and* $K_2 > \frac{E\kappa^*}{E\kappa^*+1}$*, then the controller*

$$\dot{s} = K_1 \, \psi^s \; + \; (K_2 + 1) \, \mathrm{sign}(\psi^s) \, \left(\mathbf{f}_s \cdot {}^{C}\mathbf{v}^{EE} \right) \tag{4.1}$$

renders the closest point of C to EE uniformly exponentially stable over the whole curve C.

Proof 1 *The proof is based on a control Lyapunov function*

$$V = \left(\mathbf{\Gamma} \cdot \mathbf{\Gamma} - \mathbf{E} \cdot \mathbf{E} \right) / 2 \tag{4.2}$$

Continuity of the Lyapunov function V follows from the convexity of the curve C and continuity of the relative motion. Positive definiteness of the Lyapunov

function follows from the fact that $\zeta^2 \leq V$*, while decrescency of the Lyapunov function follows from the niceness of the curve resulting in the inequality* $V \leq \rho\zeta^2$*, where* ρ *is a positive constant. To prove global uniform asymptotical stability of the algorithm, the negative definiteness of the time derivative of the control Lyapunov function and invariance over the curve are shown. Uniform exponential convergence is proven by showing that the time derivative of the control Lyapunov function is upper bounded by a negative definite function of the error state* ζ*. Differentiating the vectors in the reference frame C, the time derivative of V is given by*

$$\dot{V} = (\mathbf{\Gamma} - \mathbf{E}) \cdot {}^{C}\mathbf{v}^{EE} - \mathbf{\Gamma} \cdot \mathbf{f}_s \, \dot{s} \tag{4.3}$$

Defining $\Psi^s \triangleq \mathbf{\Gamma} \cdot \mathbf{f}_s$*, the term* $\Psi^s \dot{s}$ *defines the controls while the remaining disturbance term along the tangent and normal directions can be expressed as*

$$(\mathbf{\Gamma} - \mathbf{E}) \cdot {}^{C}\mathbf{v}^{EE} = [\, (\mathbf{\Gamma} \cdot \hat{\mathbf{n}} - E)\ \hat{\mathbf{n}} \ + \ \psi^s \ \mathbf{f}_s \,] \cdot {}^{C}\mathbf{v}^{EE} \tag{4.4}$$

Using feed-forward and feedback controls (update rules) as $\dot{s} = \dot{s}_{ff} + \dot{s}_{fb}$*, the system can be regulated to* $\zeta = 0$*. In particular, the tangential component of the disturbance can be canceled with the feed-forward control input* $\dot{s}_{ff} = \text{sign}(\psi^s) \left(\mathbf{f}_s \cdot {}^{C}\mathbf{v}^{EE} \right)$*, while the normal component can be dominated with the feedback controllers. The feedback controllers are designed as follows: Let* ε *denote a small positive number.*

- *If* $\psi^s > \varepsilon$*, then a feedback term in the from of* $\dot{s}_{fb_1} = K_1 \psi^s$ *dominates the disturbance if* $K_1 > \frac{2\bar{\Gamma}\bar{v}}{\varepsilon^2}$*. With such a controller, it can be shown that* $\dot{V} < -\beta_1 \, \zeta^2$*, where* β_1 *is a positive constant.*

- *If* $\psi^s < \varepsilon$*, then a small signal analysis can be conducted. Noting that* $\hat{\mathbf{n}}_s = -\kappa \, \mathbf{f}_s$ *for a planar curve, the first order approximation for the disturbance*

about $\zeta = 0$ can be derived as

$$(\psi^s - E)\,\hat{\mathbf{n}} \cdot {}^C\mathbf{v}^{EE} \approx -E\kappa^* \triangle s \left(\mathbf{f}_{s^*} \cdot {}^C\mathbf{v}^{EE}\right) \tag{4.5}$$

where $\triangle s \triangleq s - s^*$. Similarly, a first order approximation of ψ^s can be calculated as

$$\psi^s \approx [E\kappa^* + 1] \triangle s \tag{4.6}$$

Then a feedback term in the from of $\dot{s}_{fb_2} = K_2 \,\mathrm{sign}(\psi^s) \left(\mathbf{f}_s \cdot {}^C\mathbf{v}^{EE}\right)$ can be used to dominate the disturbance if $K_2 > \frac{E\kappa^*}{E\kappa^*+1}$. With such a controller, it can be shown that $\dot{V} < -\beta_2\,\zeta^2$, where β_2 is a positive constant.

Since the above stated conditions can be shown to hold over the whole curve C, global uniform asymptotic stability can be claimed.

Remark 1: To avoid the discontinuity in controls causing chatter in the response, sign(ψ^s) function can be approximated by *tanh*(ψ^s).

Remark 2: If the simplified controller $\dot{s} = K_1\,\psi^s$ is used, then global uniform practical stability can be claimed since convergence to an arbitrarily small ball $\mathbb{B}_\varepsilon$ can be archived by proper selection of the controller gain K_1.

Remark 3: The results can be trivially generalized to parameterizations other than the path length parametrization.

Remark 4: The algorithm can be generalized to convex surface patches by utilizing the same control Lyapunov function V, but by using two variables u, v parameterizing the surface instead of the path length parameter s parameterizing the curve. See [138, 140] for details.

In [140], the above stated results have been extended to surface to surface tracking. Uniform asymptotical stability of the algorithm implies robustness against numerical noise and more importantly against initialization

errors on the path. Under some mild assumptions on convexity, the global convergence of the algorithm can be guaranteed, rendering any initialization on the parametric curve as an acceptable one. Requiring a few function evaluations, simple vector operations and an integrator, the algorithm is computationally efficient and easy to implement.

Operating on the projection errors, the controller can update location of the closest point to continually track the end-effector on a simple contour. However, often the desired contour is more complex than a simple 'nice' convex curve. Luckily, such complex parametric curves can be formed by tiling several curves together. While working with tiled-together contours, the determination of the relevant curve that is closest to the end-effector is required. To handle such cases, the closest point tracking algorithm has been extended to handle tiled-together curves [140]. To determine the relevant curve, a switching controller is used, where the mode switches are triggered and the proper state initializations are handled via a finite state machine. The finite state machine governing the discrete behavior of the controller is formed offline based on the Voronoi regions of the object's features and their connectivity. The finite state machine performs a feature-based tracking similar to the algorithms derived for polyhedral collision detection [141] and [142].

Even though the determination of the Voronoi regions of a complex object can be computationally expensive, the real-time performance of the algorithm is not affected since this computation is performed off-line and only once during the geometric modeling of the path.

Global convergence of the algorithm requires the each curve patch to have a unique extremum; hence, the path should be divided into strictly convex (concave) and nice curve patches. If this condition is not satisfied,

then convergence will still take place, but for initializations of TP that are "sufficiently close" to (within the region of attraction of) CP. Note that local uniform asymptotic convergence implies that even for non-convex curves, the algorithm is still immune to initialization errors, but region of attraction may not cover the whole curve patch.

4.1.2 Online Formation of the Velocity Field

A desired velocity field embeds the desired contour following task by assigning a reference velocity at every point in the manipulators' task space. In PVFC, the velocity field is used to decouple the speed of task from the task itself. In particular, with a properly designed velocity filed, the robot converges to the desired contour in a manner that is best suited for its current location independent of its speed.

The velocity field that encodes a desired contour can be constructed through a weighted superposition of two vector fields: a tangential vector field $V^{\parallel}$ and a normal vector field $V^{\perp}$. In particular, given such two fields, a velocity field V that smoothly converges to the desired contour can be calculated using sigmoidal type weight functions as

$$V = -\frac{2}{1+e^{-\upsilon E}}\, V^{\perp} + \left(\frac{2}{1+e^{-\upsilon E}} - 1\right) V^{\parallel} \tag{4.7}$$

where E represents the contour error and υ is the sigmoid variable that adjusts the relative weighting of each field with respect to E.

In general, calculation of proper tangential and normal vector fields to encode a path for any configuration of the robot end-effector is a challenging task, mainly because determination of the closest point on a generic curve is not trivial. However, equipped with the closest point tracking algorithm presented in subsection 4.1.1 that determines the parameter of

the closest point s^* on a parametric curve $\mathbf{f}(s)$, such vectors can be simply calculated as

$$V^{\parallel} = v\,\mathbf{f_s}(s^*) \tag{4.8}$$

$$V^{\perp} = \chi\,(\mathbf{r}^{C_oEE} - \mathbf{f}(s^*)) \tag{4.9}$$

where v and χ are scaling parameters.

Figure 4.2 presents the tangential and normal vector fields calculated at every configuration of the robot end-effector using the closest point tracking algorithm presented in subsection 4.1.1.

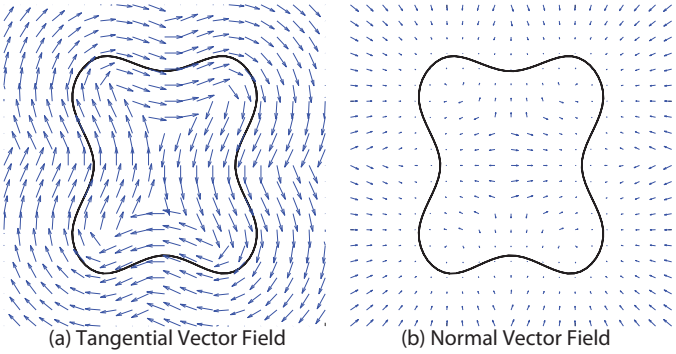

Figure 4.2: Tangential and normal vector fields

Figure 4.3 presents the desired velocity field calculated using the sigmoidal weighted sum of tangential and normal vector fields. Note that calculation of the velocity field at every position of the end-effector is not necessary for PVFC, since a reference velocity can be calculated online given the actual position of the end-effector. Here, Figures 4.2 and 4.3 are constructed off-line, only to allow for visualization of the vector fields.

Extension of this velocity field generation methodology to path tracking in 3D is trivial and equations (4.8) and (4.9) are still valid for forming the velocity field. Furthermore, extension to surface tracking can be achieved utilizing the same perpendicular component of the field, while tangential

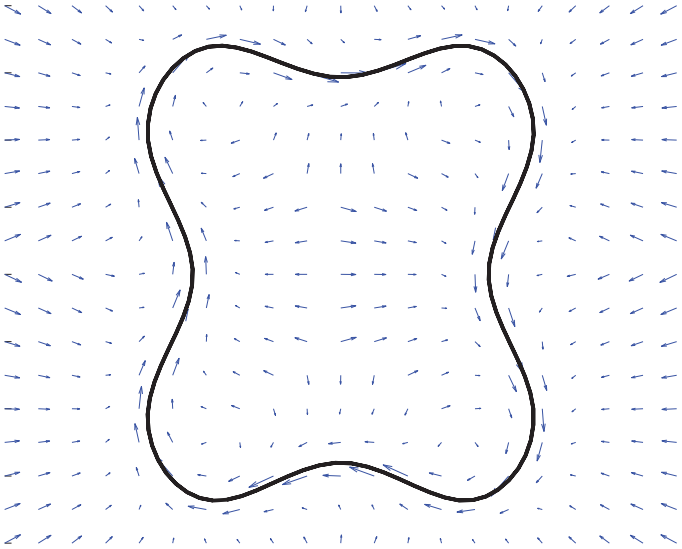

Figure 4.3: Weighted sum of tangential and normal vector fields

component is formed with projection of Γ vector on the tangential plane.

4.2 Methods for Slacking Prevention

Within the proposed control framework, slacking prevention can be implemented through three different methods: (i) by changing the shape of the desired contour, (ii) by regulating the assistance acting towards the desired contour, and (iii) by modifying the speed of the task. Thanks to the separability property of the controller, these slacking prevention schemes can be implemented individually or concurrently. Whenever the contour tracking error metric, typically calculated based on the integration of the instantaneous contour error E within a window, becomes lower than a predefined threshold, the preferred modification method(s) can be triggered in order to increase the task difficulty. Note that the aim of this thesis is to provide the framework that enables implementation of slacking prevention with guaranteed interaction stability and task continuity. The decision on the use of proper method or combination of the available methods is

left to the expertise of the therapist, to be customized based on the needs of the patient.

4.2.1 Changing the Shape of the Desired Contour

The desired contours are parametrized and formed by Non-Uniform Rational B-Spline (NURBS) curves. These parametric curves are powerful yet easy to use tools which can be utilized to design exercise paths that define customized rehabilitation tasks for each patient. Complexity of the contour following task can easily be modified by changing the control points or knot sets defining the curve, without breaking continuity of the contour. Thanks to the local support property of NURBS curves, a curve can be modified locally without changing its shape in a global manner.

The smoothness of movement and safety precautions require that the transition between the curves should be at least C^1 continuous, so that the tangential component of the velocity field is free of abrupt changes. Continuous change of contours can be achieved by generating a curve patch between the desired parameters on the original contour and the target contour, while imposing a differentiability constraint at the boundaries.

When a contour change is triggered due to the decrease of the error metric down to a pre-determined threshold, the complexity of the target curve can be increased by various techniques ranging from a simple increase of the relative distance between of control points to more advanced methods based on curvature modulation.

Note that neither the continuity of contour following task and smoothness of the assistance provided throughout the task, nor the coupled stability of the overall robot-patient system are compromised with the introduction of the curve patch or modulation of the shape of the target

curve. Therefore, it provides a unique and systematic method in literature to continuously modulate the contour shape for slacking prevention.

4.2.2 Regulating the Assistance Guiding towards the Contour

The amount of assistance provided to guide the patient towards the target contour can be modified based on the performance of the patient to prevent slacking behavior. Since the level of assistance is coupled to the amount of energy available within the system, the perpendicular vector field can be modulated by adjusting the scaling parameter χ (in Eqn. (4.9)) normalized by the square root of the instantaneous energy of the system.

In particular, if the performance of the patient is observed to stay above a predefined threshold, the assistance due to the perpendicular vector field can be scaled down by decreasing the scalar parameter χ normalized by the instantaneous velocity. Assistance modification has been proposed in the literature through the use of forgetting factors or utilization assistance levels, such as more-than/less-then linear approaches. However, these ad-hoc methods cannot ensure coupled stability, while implementation of assistance modification with PVFC is guaranteed not to jeopardize passivity; hence, ensures coupled stability.

4.2.3 Modifying the Speed along the Contour

During most of the conventional rehabilitation exercises, the pace of the task is left to the control of the patient, so that the patient can assume a natural and comfortable speed for the task. However, in order to prevent slacking of the patient, speed of the movement on the desired contour can be regulated. In PVFC, the pace of the task is determined by the total energy present in the system. This energy is due to the initial conditions and the

work done by the external forces, that is, the energy provided/subtracted by the patient and disturbance forces acting on the system. However, the speed of the contour following task can also be controlled by regulating the total energy of the system by the actuators through an exogenous control term appended to the original PVFC controller in Eqn. (3.14) as

$$\tau_{\text{forced}} = \varsigma \, \bar{\mathrm{P}} \left(\mathrm{r} - \frac{\bar{\mathrm{P}}^T \, \dot{\bar{q}}}{2\bar{\mathrm{E}}} \right), \quad \varsigma > 0 \tag{4.10}$$

where ς is a damping coefficient and r is the speed coefficient; addition of this extra term τ_{forced} causes the velocity $\dot{\bar{\mathrm{q}}}$ to converge to $r\bar{\mathrm{V}}$.

With this exogenous control law in place, if the error metric becomes lower than the predefined threshold, the pace of the exercise can be increased to prevent slacking, by introducing energy to the system through positive work done by the actuators. This method is similar to changing the frequency of the motion as the patient performance increases [133]. However, in our case, the speed of the task can be modified instantaneously at any desired section of the curve. This feature enables a large portfolio of rehabilitation protocols to be realized when compared to changing the frequency of the motion at each movement repetition.

4.3 Implementation and Verification of Slacking Prevention Method

We have implemented the proposed slacking prevention schemes on a physical setup to test the feasibility and coupled stability of the approaches. The experimental setup consists of a two degrees of freedom planar haptic interface equipped with a six axes F/T sensor as shown in Figure 4.4. The haptic interface is controlled with PVFC in real-time with a sampling frequency of 1 kHz through a desktop computer equipped with a PCI I/O

card.

In order to demonstrate passivity of the controller while implementing each of the proposed slacking prevention methods, the kinetic energy of the augmented system is compared with the energy entered to the system through the work done by the external forces, by the user and/or the speed regulator term of the controller (Eqn. (4.10)). External forces applied by the user F_h are measured with the force sensor attached at the end-effector of the mechanism so that work done by user E_h can be calculated as

$$E_h = \int_0^t F_h^T \dot{x}\, d\tau \tag{4.11}$$

Note that force sensor is used only for validation of the passivity of the

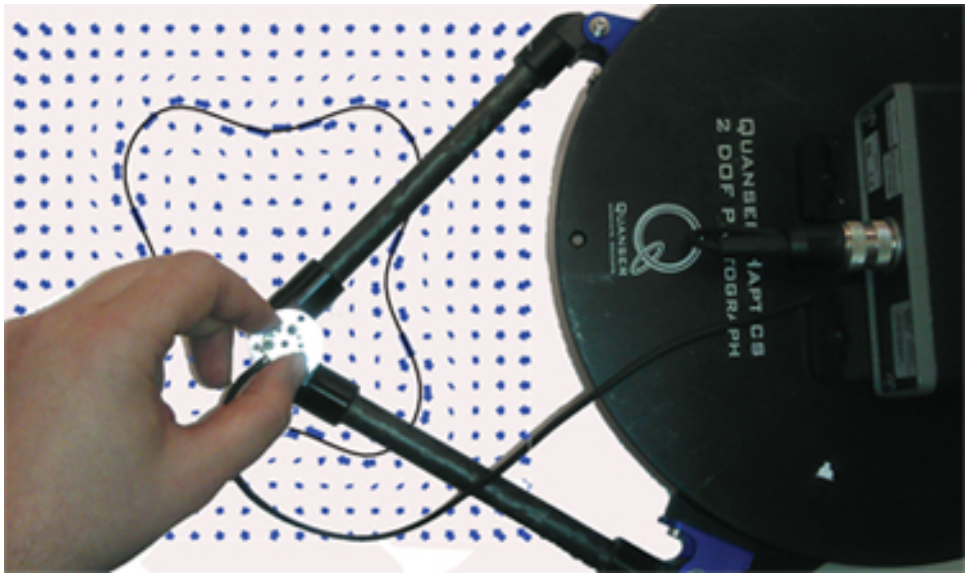

Figure 4.4: Force sensor equipped planar two DoF haptic interface under PVFC is employed to track closed contours.

controller and is not required to implement PVFC. End-effector velocities can be calculated from joint rotations through motion level kinematic relations: $\dot{x} = J\,\dot{q}$.

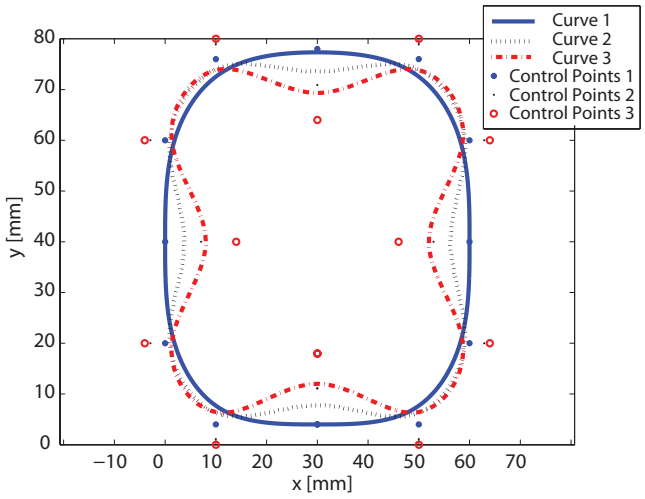

Figure 4.5: Three curves with simple, mild and hard difficulty levels

4.3.1 Changing the Shape of the Desired Contour

In this experiment, three curves with increasing complexity are created using the SISL NURBS library of SINTEF, as shown in Figure 4.5. In Figure 4.5, Curve 1 is the simplest path, Curve 2 offers mild difficulty, while Curve 3 is the hardest path, based on their curvature profiles. An equal circumference constraint is enforced for these curves such that the performance metric based on integration of instantaneous contour error E serves as a fair means of comparison of performance even while performing on different contours. Even though modifications of the contours can be performed online thanks to the the local support property of NURBS curves, in general, keeping the path length constant requires alterations that reach beyond the local modifications. Hence, the curves in Figure 4.5 are designed offline.

The experiment starts with the easiest curve, Curve 1, and typically curve changes are triggered when the patient performance reaches above a pre-determined threshold. In all of the implementations presented in this

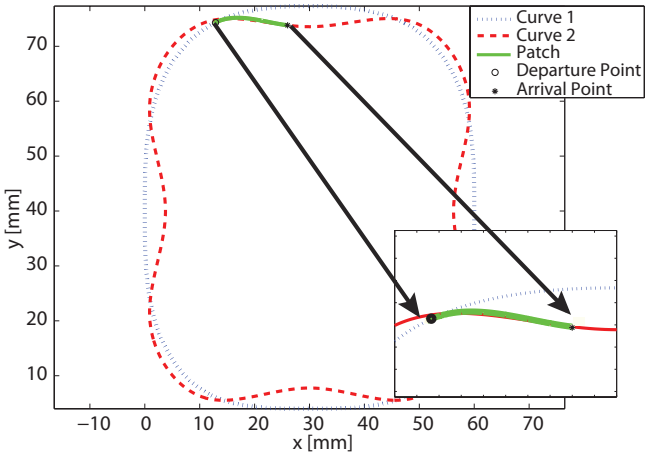

Figure 4.6: Transition from Curve 1 to Curve 2 with C^1 continuity

section, changes are triggered just after completing the first cycle on the closed contour, that is when $s = 0$, in order to simplify presentation. Once a curve change is triggered, a patch curve is generated between the current and the target curves in order to connect these two curves without breaking C^1 continuity of the path being followed by the users. Figure 4.6 presents such a curve patch generated for continuous transition from Curve 1 to Curve 2. In this example, the parameter that locates the departure point on Curve 1 is chosen as $s^d = 0.3$, while the parameter that locates the arrival point on Curve 2 is set as $s^a = 0.4$.

Figure 4.7 depicts the energy plots of the system under two different test cases: in the first case (Figure 4.7(a)) no external forces are acting on the system, while in the second case (Figure 4.7(b)) the user applies external forces through the end-effector of the device. For both cases, system is initialized with a fixed amount of initial energy. For the first case, the kinetic energy of the augmented system is expected stay lower than this initial energy at all times, while in the second case, the energy increase is expected to stay less than the work done by the external forces, since PVFC

guarantees passivity with respect to externally applied forces. Moreover, no discontinuities should be observed in the system energy due the change of curves.

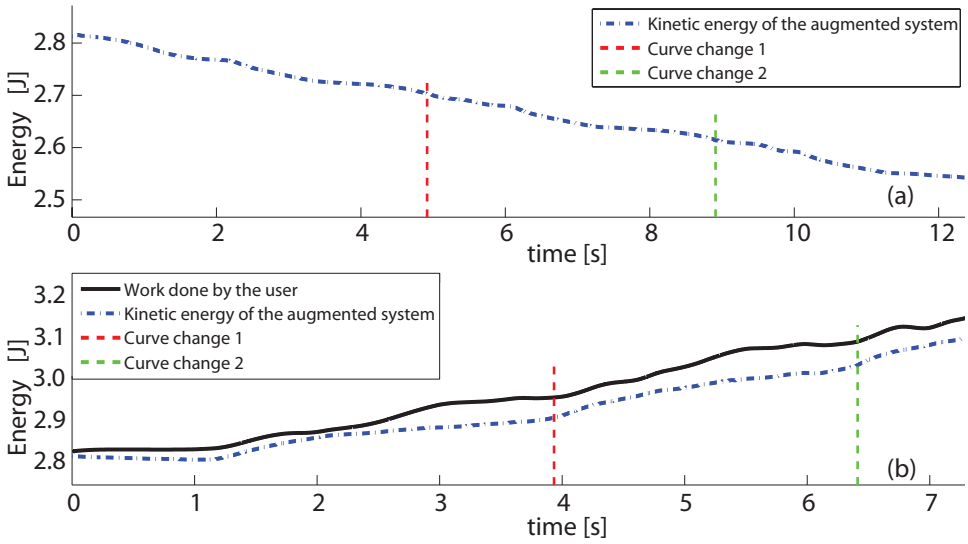

Figure 4.7: Kinetic energy of the augmented system while changing the shape of the desired contour. a) Without external forces b) With external forces

Figure 4.7(a) demonstrates that energy of the overall system k_a is continuous and does not exceed the initial energy on the system as anticipated. In fact, k_a decreases gradually due to the negative work done by the friction forces inherent to the haptic interface. One can observe from Figure 4.7(b) that although the kinetic energy of the augmented system increases, this increase remains bounded with the energy provided by the user. The work done by the user is larger than the kinetic energy increase of the augmented system, since some of the work done by the user is dissipated by the friction forces. The energy plots are continuous as expected. Hence, the experiments verify that the curve change for slacking prevention within the proposed control framework preserves passivity of the system with respect to externally applied forces, as predicted by the theory.

4.3.2 Regulating the Assistance Guiding towards the Contour

In this experiment, three different assistance levels are selected by using three different scalar parameters χ for the normal component of the velocity field. Note that changing this assistance value does not change the controller characteristics (passivity and convergence), as long as $\chi > 0$. The desired path is chosen to be Curve 1, the curve with the easiest difficulty level. In this experiment, the speed regulation term (Eqn. (4.10)) is added to the controller so that the pace of contour following and thus the energy of the overall system is modulated. Inclusion of the speed regulation term into the controller is necessitated in order to analyze the effect of the assistance change independent of the speed change in the system. As in the previous subsection, the kinetic energy of the augmented system is analyzed for two cases: with and without external forces. Due to the existence of the speed regulator term in the controller, overall energy of the system is expected to stabilize around the predetermined values in both cases. However, the work done by this extra term should be solely responsible for the energy of the augmented system for the first case, since there exists no external forces and controller should not generate additional energy, say due to a change in the normal component of the velocity field. In the latter case, it is expected that the kinetic energy of the overall system does not exceed the sum of work done by the user and by the speed regulator term.

Figure 4.8(a) shows that energy of the system is successfully modulated to the pre-defined value that is dictated by the speed regulator. Moreover, the change in the level of assistance along the normal direction neither injects additional energy at the trigger instances nor cause discontinuities. Therefore, the smoothness of control action and the passivity of the con-

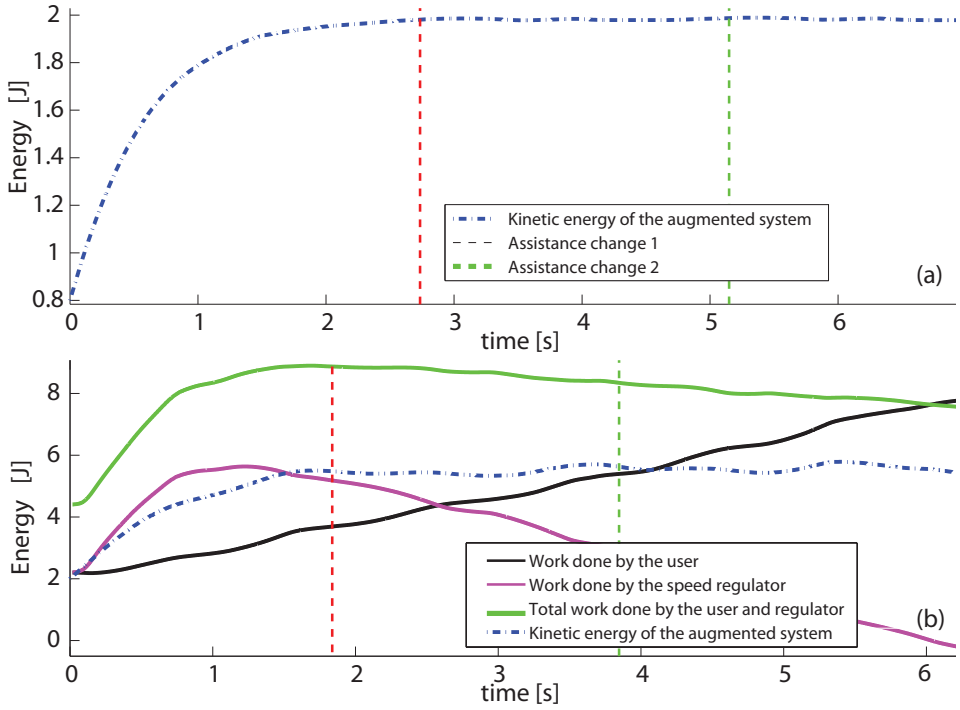

Figure 4.8: Kinetic energy of the augmented system while reducing the assistance guiding towards the contour. a) Without external forces b) With external forces

troller are preserved. Same conclusions are also valid for the second case in which external user forces act on the system. As depicted in Figure 4.8(b), in this case the energy of the overall system increases and stabilizes around the pre-defined value enforced by the speed regulator. In particular, the speed regulator injects additional energy or subtracts excess energy from the system in order to maintain the desired energy level throughout the trial. As expected, the overall energy remains bounded by the total work done by the user and the speed regulation term.

4.3.3 Modifying the Speed along the Contour

For the third method, three different task speeds are implemented by adjusting the speed coefficient term r of the speed regulator. Curve 1 is

utilized for the experiment and the assistance level is set to an adequate constant value. Figure 4.9(a) shows that although there is no external forces, speed regulator term can increase the energy of the overall system from zero to the desired level and after each instance of task speed change, the system converges to a new energy level. The kinetic energy of the augmented system always remains lower than the energy provided by the speed regulator. When there are external forces acting on the system, the speed regulation term can compensate for the energy provided by the user in order to keep the energy at desired levels for each speed level. Nevertheless, the kinetic energy of the overall system remains lower than the total energy input to the system.

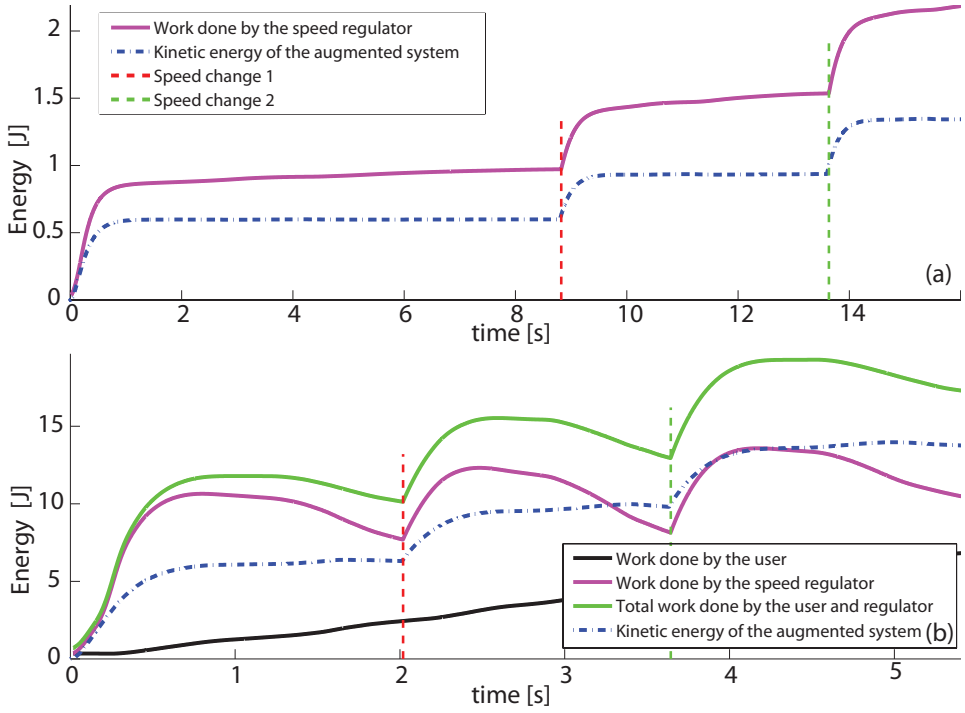

Figure 4.9: Kinetic energy of the augmented system while increasing the speed along the contour. a) Without external forces b) With external forces

4.4 Slacking Prevention User Study

In order to test the applicability and efficacy of the proposed slacking prevention framework, an additional experiment is conducted with healthy subjects, for the method of changing the shape of the desired contour. In this experiment, regulation of the speed of the task is left to the user. In that respect, the error metric is chosen as the scaled cumulative contour error, in which the sum of instantaneous errors over a loop on the curve is scaled by the average speed for that loop. Therefore, the user should, not only perform the contour following task with low contour errors, but also maintain adequate speeds in order to achieve enough progress in performance to trigger the slacking prevention. This requirement is imposed in order to keep the contour following task challenging enough for healthy subjects, even though the speed of the task may not be taken as a regulated parameter or may be supervised by the therapist during rehabilitation exercises. Assistance provided along the normal direction towards the contour is kept at an intermediate level so that the task remains challenging, yet achievable after a reasonable amount of cycles. Since the volunteers are expected to learn the task using only the force feedback provided, visual feedback is intentionally disabled during the healthy subject experiments. In order to limit the large deviations from the contour, virtual walls (with dead zones) are also implemented around the curve. Instructions given to the volunteers are to follow the contour embedded in the force field as closely as possible at a self-imposed pace and to increase their pace as they feel more comfortable with the task. Volunteers are allowed to explore the workspace to get familiar with the task before the experiment is administered.

Figure 4.10(a) presents the normalized cumulative contour error with

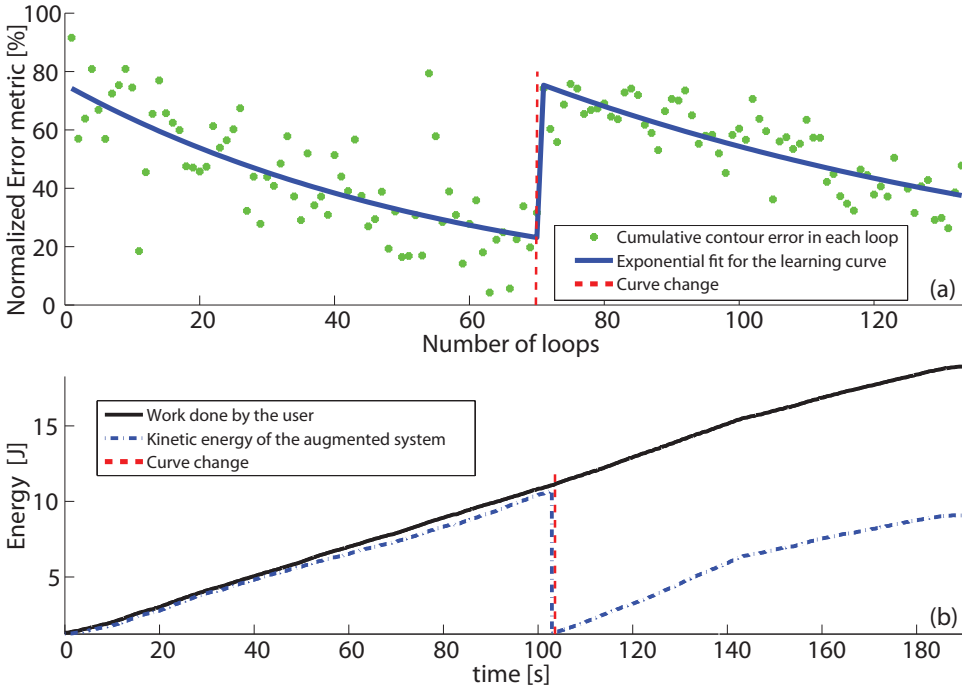

Figure 4.10: a) Normalized cumulative contour error with respect to the number of loops completed for a typical volunteer. Exponential curves are fit on the human subject data to help visualize the rate of learning. b) Kinetic energy of the augmented system together with the work done by the user.

respect to the number of loops completed for a typical volunteer. The instant when the curve change is triggered is also marked on the figure. As expected, the normalized cumulative contour error is large at the start of the task but decreases rapidly as the volunteer learns how to complete the task. In Figure 4.10(a) exponential curves are fit on the human subject data to help visualize the rate of learning. Once the performance of the volunteer increases up to a pre-defined threshold, a curve change is triggered for slacking prevention and a sudden increase in the error can be observed just after this curve change. Once again, the volunteer easily adapts to the new contour and his learning is modeled by the second exponential learning curve in the figure. Even though only anecdotal at this point (a larger user study is currently ongoing), Figure 4.10(a) provides evidence that the slacking prevention by changing the contour to be followed can be effective by compensating for human learning to keep the user engaged throughout the exercise.

Figure 4.10(b) depicts the kinetic energy of the augmented system together with the work done by the user. In this experiment, at the instant of curve change, the energy in the system is deliberately reduced to enforce the user to exert same amount of effort while adapting to the new contour. Regardless of this modification, the user keeps on doing positive work on the system so that the speed of the task increases as more energy is injected to the system. It can be observed from Figure 4.10(b) that the passivity of the controller; hence, the coupled stability of the overall system is preserved throughout the trial.

Chapter III

5 Effects of Haptic Feedback in Adaptation of Human Motor Control System

Abilities of biological motor system are impressive looking from a purely control perspective and mimicking the performance of human motor control for planning and execution of movements is still challenging. The main challenge is the problematic properties of the plant to be controlled due to biological properties of human that possess high dimensionality, noise, redundancy, uncertainty, continuously changes and time delays. Human motor system seems to be capable to cope with this control problem seamlessly, repetitively and in an optimal manner. Identifying the principles behind this superior human motor control system is still an open question which would greatly benefit implementing control systems that can be used in rehabilitation protocols. If the methodology behind motions of humans can be discovered, exercises which are more natural to patients can be implemented. Then the aim would be to shape the motion of the patient such that it converges to the motion of an optimal features of an healthy person. Moreover, information obtained from these studies can be used for diagnosis metrics of patients by using the distance of the performance with respect to a pre-calculated optimal.

In literature, the quest for understanding human motor system starts with classification of the human motion with redundancies. In reaching

movements, even if the torso is strapped to a chair, human arm presents a seven degree of freedom kinematic chain with three degree of freedoms in shoulder joint, one degree of freedom in elbow, one degree of freedom in forearm and lastly two degree of freedoms at wrist joint. This alone is a challenging problem when we are dealing with tasks in three dimensional space. However, human motor system is capable of controlling thousands of degree of freedoms when the motion of a single degree of freedom is broken down into two pairs of muscles (agonist/antogonist) and further into the neurons that control these muscles. Moreover, when humans make point-to-point movements in free space, there is, in principle, an infinite choice of trajectories. However, many studies have shown that human subjects tend to choose unique trajectories with invariant features.

In [143], experiments are conducted for writing equivalences. Subjects write, blindfolded, a given word group with their dominant and non-dominant hands, both straight and mirrored. Although neatness of the letters differs with the difficulty of the task, all examples have similar structure and shapes for each patient. A second experiment is conducted which also validates similarities of handwriting when the subject is assigned to write their names using only their hand or arm. These two conditions have high similarities with each other as well as the unconstrained signature. In other words, writing with different muscles, different speeds and in absence of visual feedback preserves characteristics of writer. Therefore, this demonstration is an evidence: action is planned and executed in terms of the goal, not of specific muscle contractions. To that end researchers assumed redundancy is eliminated by adding internal constraints. Investigation of these phenomenon are validated through prior experiments in which tasks are made of simple visual stimulus and

successful point-to-point reaching movements. These experiments show that movements tend to be straight (or, slightly curved) and smooth and the velocity profile of the hand trajectory is bell-shaped. From that point researches on this topic started to yearn for optimal control theory for finding the models that can represents invariant features of the human motion in detail. It is proposed that biological system evolved to find optimal solutions beforehand and uses them online to move to a point in space. More generally, in the optimization approaches, the trajectory is predicted by minimizing a cost functional J, over the movement time T, subject to zero boundary conditions imposed on start and end points, corresponding to the rest states at each end. The performance index can be formulated in the joint space, in the task space normally associated with the human hand, or in the task space of object coordinates if there exists a nonrigid coupling between hand and the object. Various studies are proposed in order to define the correct cost functional in that structure so that unconstrained point-to-point reaching movements can successfully predicted. Generally the challenge has been to try to reverse-engineer the cost function from observed movement patterns and perturbation studies.

These approaches can be divided into three major categories. First category is to use cost functions generated from kinematic quantities such as jerk [144] or acceleration [145]. These controllers use n^{th} derivatives of the position function for the cost to minimize. Note that these position values may be the joint space coordinates or task space coordinates as mentioned above. Among these methods Minimum Jerk Model is widely accepted through various experimental validations. It provides an explanation to the constraint problem for redundancy of the hand muscle system and is consistent with the experimental results which produce approximately

straight bell-shaped tangential velocity profiles. Minimum jerk model further generalized for curved motions such as opening a door [146] and for tracing a sphere with the end-effector of a robot [147]. In the latter studies, Lagrangian multiplier are integrated to the cost function in order to deal with geometric constraints of the objects. Before going into the details of other models, a quick note regarding the reference [148] should be highlighted. In this study, authors show that smoothness of the motion of the patients are degrading and with successful rehabilitation exercises in time, patients regain some of the smooth characteristics of healthy subjects. Therefore, it is claimed that jerk of the motion can be used for progress metric. This hypothesis alone supports the motivation for investigating the human motor system in order to increase the outcomes of a rehabilitation.

Experiments with minimum jerk models show that although for horizontal motions the characteristic for the human motion can be predicted, for vertical movements, results are not satisfactory. The reason is motivated to be the gravity and work done against it. Therefore, Uno *et al.* proposed that cost to be minimized can't simply be described with only kinematic quantities [149]. They proposed Minimum Commanded Torque Change Model, which minimized the commanded torque in each joint which is calculated with a muscle model and dynamic equation of a simplified two link manipulator. For movements within the horizontal and sagittal planes, the minimum commanded torque change model was shown to reproduce the spatial characteristics of measured trajectories; the magnitudes and directions of curvatures, better than kinematic based models models while comparing the correlation of the experimental data and the simulations of the models. On the other hand, another experiment is conducted in [150], where visual feedback of hand position was altered so as

to increase the perceived curvature of the movement. As expected, this experiment supports kinematic based models when compared to dynamic cost function methods, in particular minimum jerk, since the disturbance is kinematic based. Therefore, each model has the advantages against each other when the situation in each task is differentiated accordingly. Moreover, questions such as how central nervous system benefits from having smooth movements and how complex quantities, such as jerk or torque change, and then integrate them over the duration of a trajectory could be estimated, is still unknown.

Third category is benefiting from stochastic optimal control theory, based on the single physiological assumption which is more biologically plausible approach for central nervous system : The neural control signals are corrupted by noise whose variance increases with the size of the control signal [151]. In the presence of such signal-dependent noise, the shape of a trajectory is selected to minimize the variance of the arm position over a post-movement time interval. Without a comparison over the previous models, it has been shown that empirical and predicted trajectories fit with similar velocity profiles. In [152], implementation of this is generalized to continuous time and they look into the limit cases of this post-movement time, showing that minimum variance model prohibits same characteristics with minimum effort models when the post-movement time is large enough. Todorov also pointed out the similarities of signal-dependent noise to cosine tuning, or in other words minimizing squared force, in the isometric case based on average activity over agonist bursts [153]. However, the minimum variance in force focuses only on the average activity over agonist bursts, and can explain neither the spatiotemporal characteristics of redundant muscle recruitment nor the characteristics of trajecto-

ries. According to Haruno and Wolpert, [154], spatiotemporal information would provide insight for not only studying the amplitude-graded pattern of EMG, but also investigating both agonist and antagonist peak of the cosine for each muscle's activity and the trajectory overshooting. Overall, such an optimization problem based on stochastic optimal control can be conducted by either a feedforward controller such as the two models mentioned above or with an optimal feedback controller that is combined with a predictive forward model [155]. An effort penalty term which is quadratically increasing with the magnitude of the control signal is added to performance metric in order to model the lazy and sloppy characteristics of human behaviors. Furthermore, according to Todorov and Jordon redundancy is not a problem, on the contrary, it is part of the solution to increase the task performance, since theocratical model reduces the variance of the dimension that was critical for task performance, whereas the variance of other redundant dimension could increase to compensate for this.

Above models in three categories give valuable insights for human reaching movements with positional constraints, however, rhythmic tasks where user is told to perform a rhythmic operation such as drawing circles is shown to be covered by different characteristics. In [156], using a human functional neuroimaging experiment, it is shown that compared to the areas activated in rhythmic movements, discrete movements contains several higher cortical planning areas including the areas that are valid for rhythmic movements. Therefore, rhythmic movements needs a separate neurophysiological and theoretical treatment. Early studies on handwriting and drawing movements observed that there is a systematic relationship between the velocity of the end-effector trajectory and the geometric

path that it describes. From that observations, Lacquaniti *et al.* , [157], came up with the 2/3 Power Law, which states that the angular velocity of the endpoint is proportional to the curvature of the end-effector path by satisfying the power relation of 2/3. This formula is shown to be valid for circular drawing experiments in horizontal planes, however, Schaal *et al.* shows that it is not valid for elliptical trajectories which contain nonlinear effects in vertical planes. Subjects rather employed smooth oscillatory pattern generators in joint space to realize the required movement patterns [158]. On the contrary, in [159] authors use another central pattern generators named as 'The Matsuoka Oscillator' which can be used for rhythmic movements as well as discrete motions with feeding central pattern generator with an exponentially decaying phasic input. However, results in this study only validates that similar velocity profiles for discrete movements can be obtained with a pattern generator. In general, all of the mentioned studies in rhythmic movements focus on a subset of answers; satisfying some of the properties of human motor system. An explanation is still necessary on how human motor system get use of these models, or how parameters that are calculated with regression in generators are neurophysiologically decided in real time.

Another direction towards the generalization of the optimal models would be analyzing the behavior of human motor system under some perceptual and mechanical perturbations by artificially manipulating different parameters (e.g., inertia, stiffness, damping, etc.) of the arm. For example, in [160], authors design reaching experiments in a rotating room, and subjects perform substantial movement curvature and miss desired target position by a large amount, but after 10 reaches, subjects adopts completely and move in straight lines. After disturbance is canceled, sub-

jects again make errors, this time opposite to the direction of rotation. However, they were able to wash out the after-effects in time. Another method for artificial disturbance generation is to use force fields with the help of manipulators [161, 162]. These experiments are also in favor of the hypotheses that motor controller was gradually composing a model of the force field, a model which the nervous system used to predict and compensate for the forces imposed by the environment. In particular, it has been argued that there were after-effects in workspace regions where no exposure to the field had taken place. This shows that there was transfer beyond the boundary of the training data which suggests adaptation was not via composition of a look-up table, on the contrary, subjects modeled the force field by a combination of computational elements [162].

These experiments may be classified by parametric perturbations since they do not alter the fundamental structure of the arm (e.g., the number of joints, muscles, etc.). Therefore they do not alter the number or type of state variables used to characterize the arm's equations of motion. This may be the reason of humans eventually returning to making stereotypical smooth movements after some learning period. Further analysis can be made when interactions with non-rigid objects are also taken into account which is most of the case in activities of daily livings. Manipulating non-rigid objects poses a fundamentally different control problem. New state variables (the position and velocity of the object) are added to the combined system, arm and object, being controlled. This then fundamentally alters the structure of the governing equations of motion: entirely new equations must be defined for each new state variable. Such tasks therefore constitute structural perturbations to the system being controlled. Preliminary work in structural perturbations proposes that after some time is passed for

learning, human learns inverse models for the new dynamic system [163], however, minimum jerk principle applied on hand or mass position is not capable of describing the motion characteristics for such a system [164]. Therefore, authors proposed Optimally Smooth Transport (OST) model which derives the motions of the hand that achieve the maximally smooth motion of the transported object, compatible with the constraints of the hand-object interaction. This model is capable of creating the bi-phasic velocity profile of the hand velocities as well as uni-phasic characteristics of the velocity profile of the object observed in experiments. On the other hand, Svinin *et al.* pointed out that the trajectories found by this model does not depend on the stiffness of the spring between hand and object [165], although one should expect convergence of minimum jerk models with OST when there is a rigid coupling between hand and the object ($k \rightarrow \infty$). They proposed that minimum hand jerk models can still be used for systems under structural perturbations if dynamic constraints defined by the dynamic model of the object are also integrated [166].

Analysis of rhythmic movements when dealing with structural perturbations is still an open question, and adaptation of human motor system with changing dynamical system parameters would give an insight on how human cope with these instant changes. It is a well known fact that if a system parameter is changed after adapting to a predefined system, users tend to over/undershoot the given task but after some time human are capable of adapting to the new system with altered parameters. [167, 168].

In this chapter, the adaptation properties of human motor control system on rhythmic dynamic tasks is analyzed, in particular, non-rigid oscillating tasks under structural disturbances without any positional end-point constraints. Characteristics of human motor control system over rhythmic

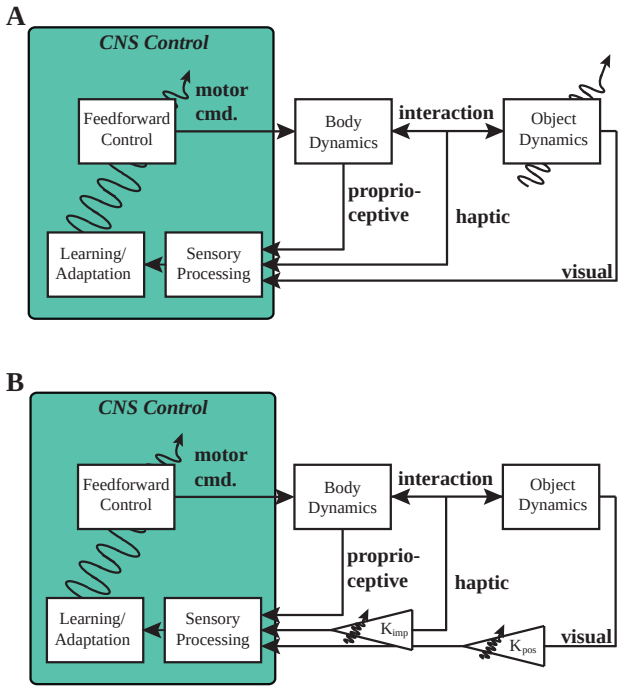

Figure 5.1: Parameter changes shown in online feedback tuning/parameter modification. A shows the setup for first for Seatings, while B shows the setup for equivalent transfer functions, Seatings 5 and 6.

movements is shown to be variant than reaching motion in literature, and analysis with dynamic tasks would help identifying the necessary conditions for virtual reality implementations in robot aided rehabilitation. To this end, an experiment is conducted in order to investigate the effects of dynamic parameters on human motor adaptation to a manually excited virtual second-order system with a within trial "catch" procedure. Psychophysical analysis of human interactions with particular parameter sets on the human motor controller is performed over the steady state frequency error after catch and rate of adaptation to the new frequency value. Further analyses are carried out using equivalent systems with identical position or impedance transfer functions. It should be noted that the specified task is fundamentally different from stiff object manipulation and free reaching

movements, since, there exists no proprioceptive feedback between hand and the dynamic object [169]. Remaining possible feedbacks of the task are either visual or haptic information which represent the trajectory of the dynamic object and the force observed from the end-effector of the device, respectively. Figure 5.1.a represents the Seatings initially performed (from 1 to 4) where catch parameter sets fundamentally modifies the dynamic of the system affecting both information channels. Equivalent transfer functions approach, on the other hand, can modify each information channel respectively, therefore provides a unique perspective in the analysis of the human motor control system, as illustrated in Figure 5.1.b.

5.1 Experimental Methods

In order to examine the rate of human adaptation to parameter variations of dynamic systems, A preliminary experiment is designed with a dynamic virtual reality environment. Experiments are conducted using a haptic device, a two degrees-of-freedom (DoF) planar manipulator, where one of the translational axes is used in order to excite the second order virtual system. Hypothesis tested, details of the mechanical system, the equation of motion governing the virtual system dynamics and the experiment design are detailed in this subsection.

5.1.1 Hypothesis

It is hypothesized that increasing the gain will help subjects better perceive the system dynamics, but at a cost of larger power input required to complete the task. Increasing damping is expected to have a stabilizing effect on human motor control, while perception of the natural frequency is diminished, thereby slowing adaptation.

It is hypothesized that damping would provide a stabilizing effect in the haptic interaction, however, at the cost of losing distinct frequency characteristics due to the high damping values. Moreover, it is expected that setting the target frequencies after catch would not introduce extrinsic influence in the statistical analysis whether they are fixed according to the natural or damped natural frequency values.

It is hypothesized that the use of equivalent transfer functions can help identify the dominant feedback modality during a rhythmic dynamic task. In particular, given the fast pace of the rhythmic task, it is expected that force feedback would be more dominant in rate of adaptation than visual cues, therefore, motion provided to the users are scaled to fit the virtual representation although, dynamic effects of physical parameters are kept truthful. In other words, the first part of implemented experiments are used in order to find the effects of magnitudes of haptic feedback over the adaptation a dynamic task. In this case, impact of different individual or bundled set of second order system parameters to the performance can be analyzed. It is hypothesized that the main contributing factor would be the magnitude of the haptic cue which would presumably decrease the performance due to effort requirements.

5.1.2 Experimental Setup and Virtual Environment

The experimental setup consisted of a 2 DoF planar haptic device (Pantograph by Quanser Inc.) as shown in Figure 5.2. The visual cues were updated at a rate of 50 Hz on the screen while the haptic rate was set at 500 Hz. Participants wore noise cancellation headphones playing pink noise to mask possible auditory cues from the environment and the hardware.

During the experiment, two rectangular masses were displayed on

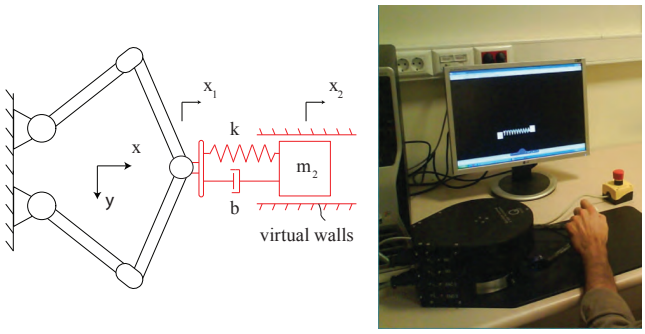

Figure 5.2: Experiment setup and the virtual environment

the screen. The motion of one mass, m_1, was directly coupled with the motion of the end-effector, while the second mass, m_2, was connected to m_1 by a virtual spring and damper resulting an indirect control over m_2. The instantaneous states (position, velocity and acceleration) of m_2 were calculated by the following second-order dynamic equation using Euler's method of numerical integration

$$m_2\,\ddot{x}_2 + b\,\dot{x}_2 + k\,x_2 = G\,(b\,\dot{x}_1 + k\,x_1) \tag{5.1}$$

where $\dot{x}_1$ and x_1 are the velocity and displacement of m_1, respectively and $\ddot{x}_2$, $\dot{x}_2$ and x_2 are acceleration, velocity and displacement of m_2. G is the gain, b is the damping between two masses, while k represents the spring that attaches two masses together. The natural frequency and damping ratio of the second-order system can be calculated as $\omega_n = \sqrt{\frac{k}{m_2}}$ and $\zeta = \frac{b}{2\,\omega_n}$, respectively. The physical mass, damping and friction of the force feedback device are assumed to be negligible, since the pantograph mechanism is a high-fidelity impedance-type haptic interface. Hence, throughout the discussion, the human is assumed to be a perfect position source for the haptic device. The force F applied through the motors of the haptic device

was calculated as

$$F = b\,(\dot{x}_2 - G\,\dot{x}_1) + k\,(x_2 - G\,x_1) \tag{5.2}$$

The displacement transfer function between human position input and virtual mass position output is given as

$$\frac{X_2}{X_1} = \frac{G\,(2\,\zeta\,\omega_n\,s + \omega_n^2)}{s^2 + 2\,\zeta\,\omega_n\,s + \omega_n^2}. \tag{5.3}$$

The impedance transfer function between human position input and virtual force output is calculated as

$$\frac{F}{X_1} = \frac{G\,m_2\,s^2\,(2\,\zeta\,\omega_n\,s + \omega_n^2)}{s^2 + 2\,\zeta\,\omega_n\,s + \omega_n^2}. \tag{5.4}$$

Note that the impedance transfer function is scaled by $m_2 s^2$ when compared with the position transfer function.

5.1.3 Participants

Seven healthy students of Sabancı University (six male, one female, 23–27 years old, average 24.7 years) participated in the study. All participants had prior experience with haptic devices. No participant reported any sensory or motor impairment. All participants signed informed consent forms approved by the University Research Ethics Council of Sabancı University.

5.1.4 Procedure

Participants sat in front of the monitor and held the haptic device with their dominant hand. Each trial was initiated with the mechanism and the two-mass system positioned at the neutral center of the workspace. The

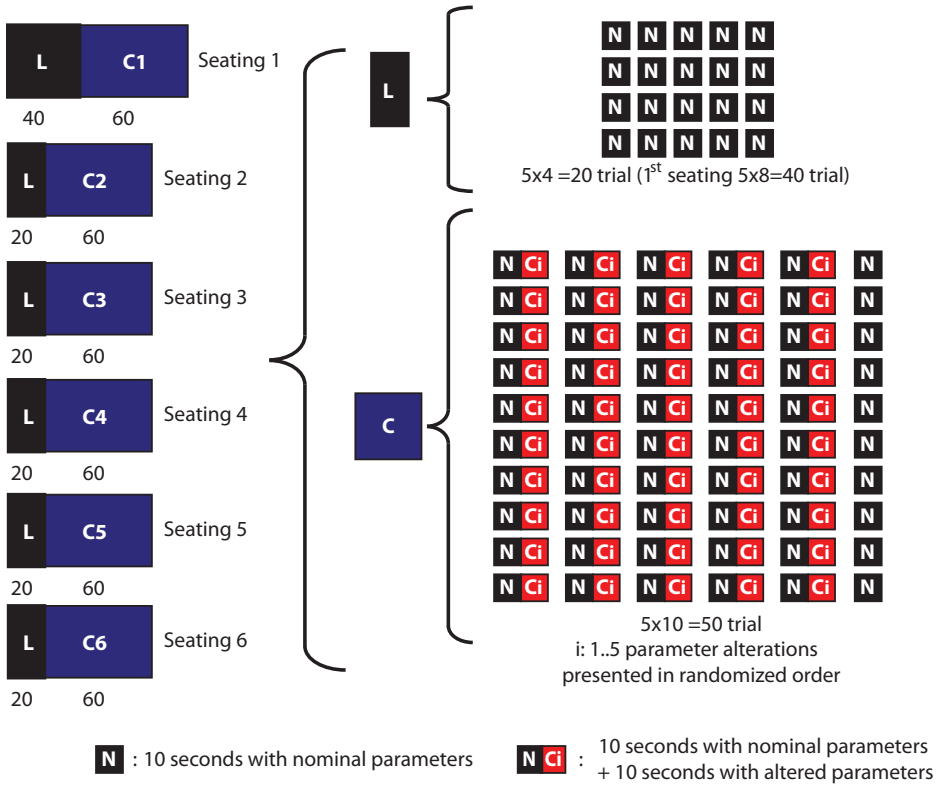

Figure 5.3: Experiment has six seatings, each with learning and catch sessions. In each seating, five different parameter sets are administered with catch trials. Each parameter set is randomly presented once in a catch trial block (five consecutive trials) and every block is repeated ten times.

end-effector of the device was coupled with m_1 and users were provided with the occurring forces of the virtual second order system. The goal was to oscillate the virtual system at its natural frequency along the x-axis in a sinusoidal manner. Motion on the y-axis was constrained with a damped-cubic-stiffness force field. Participants were told that if the excitation was at the natural frequency of the virtual second-order system, the amplitude of oscillations of m_2 would be largest for constant amplitude excitation of the end-effector. Participants were also instructed to excite the system in using smooth natural movements of their hand.

Table 5.1: Experiment seatings, effect levels, nominal and target system parameters and the location of the related Bode plots

Seating	Task	Effect Levels	System Parameters	Related Figure
Low Freq. Nominal	-	-	$m_2 = 1kg$, $b = 2.4Ns/m$, $k = 40N/m$, $G = 0.272$ and $\omega_n = 1.066$	Low Freq. with Legend (0) in Figure 5.4
Seating 1	Gain Change	High Freq. Nominal	$m_2 = 0.8kg$, $b = 2.4Ns/m$, $k = 64N/m$, $G = 0.32$ and $\omega_n = 1.423$	Legend (1) in Figure 5.4
		G Lowest	$m_2 = 0.8kg$, $b = 2.4Ns/m$, $k = 64N/m$, $G = 0.128$ and $\omega_n = 1.423$	Legend (2) in Figure 5.4
		G Lower	$m_2 = 0.8kg$, $b = 2.4Ns/m$, $k = 64N/m$, $G = 0.224$ and $\omega_n = 1.423$	Legend (3) in Figure 5.4
		G Higher	$m_2 = 0.8kg$, $b = 2.4Ns/m$, $k = 64N/m$, $G = 0.416$ and $\omega_n = 1.423$	Legend (4) in Figure 5.4
		G Highest	$m_2 = 0.8kg$, $b = 2.4Ns/m$, $k = 64N/m$, $G = 0.512$ and $\omega_n = 1.423$	Legend (5) in Figure 5.4
Seating 2	Damping Change	High Freq. Nominal	$m_2 = 0.8kg$, $b = 2.4Ns/m$, $k = 64N/m$, $G = 0.32$ and $\omega_n = 1.423$	Legend (1) in Figure 5.4
		Damp Lower	$m_2 = 0.8kg$, $b = 2Ns/m$, $k = 64N/m$, $G = 0.32$ and $\omega_n = 1.423$	Legend (6) in Figure 5.4
		Damp Lowest	$m_2 = 0.8kg$, $b = 1.8Ns/m$, $k = 64N/m$, $G = 0.32$ and $\omega_n = 1.423$	Legend (7) in Figure 5.4
		Damp Higher	$m_2 = 0.8kg$, $b = 3.6Ns/m$, $k = 64N/m$, $G = 0.32$ and $\omega_n = 1.423$	Legend (8) in Figure 5.4
		Damp Highest	$m_2 = 0.8kg$, $b = 5.2Ns/m$, $k = 64N/m$, $G = 0.32$ and $\omega_n = 1.423$	Legend (9) in Figure 5.4
Seating 3	Gain and Damping Change	High Freq. Nominal	$m_2 = 0.8kg$, $b = 2.4Ns/m$, $k = 64N/m$, $G = 0.32$ and $\omega_n = 1.423$	Legend (1) in Figure 5.4
		Low Damp/High G	$m_2 = 0.8kg$, $b = 1.2Ns/m$, $k = 64N/m$, $G = 0.512$ and $\omega_n = 1.423$	Legend (10) in Figure 5.4
		High Damp/High G	$m_2 = 0.8kg$, $b = 5.1Ns/m$, $k = 64N/m$, $G = 0.512$ and $\omega_n = 1.423$	Legend (11) in Figure 5.4
		Low Damp/Low G	$m_2 = 0.8kg$, $b = 1.2Ns/m$, $k = 64N/m$, $G = 0.128$ and $\omega_n = 1.423$	Legend (12) in Figure 5.4
		High Damp/Low G	$m_2 = 0.8kg$, $b = 5.1Ns/m$, $k = 64N/m$, $G = 0.128$ and $\omega_n = 1.423$	Legend (13) in Figure 5.4
Seating 4	Common Peak Magnitude with Different Damping	High Freq. Nominal	$m_2 = 0.8kg$, $b = 2.4Ns/m$, $k = 64N/m$, $G = 0.32$ and $\omega_n = 1.423$	Legend (1) in Figure 5.4
		Lowest	$m_2 = 0.8kg$, $b = 1.2Ns/m$, $k = 64N/m$, $G = 0.16$ and $\omega_n = 1.423$	Legend (14) in Figure 5.4
		Lower	$m_2 = 0.8kg$, $b = 1.8Ns/m$, $k = 64N/m$, $G = 0.24$ and $\omega_n = 1.423$	Legend (15) in Figure 5.4
		Higher	$m_2 = 0.8kg$, $b = 3.0Ns/m$, $k = 64N/m$, $G = 0.40$ and $\omega_n = 1.423$	Legend (16) in Figure 5.4
		Highest	$m_2 = 0.8kg$, $b = 3.6Ns/m$, $k = 64N/m$, $G = 0.48$ and $\omega_n = 1.423$	Legend (17) in Figure 5.4
Seating 5	Equivalent Position TF	High Freq. Nominal	$m_2 = 0.8kg$, $b = 2.4Ns/m$, $k = 64N/m$, $G = 0.32$ and $\omega_n = 1.423$	Legend (1) in Figure 5.4
		Lowest Imp. Gain	$m_2 = 0.2kg$, $b = 0.6Ns/m$, $k = 16N/m$, $G = 0.32$ and $\omega_n = 1.423$	Legend (18) in Figure 5.4
		Lower Imp. Gain	$m_2 = 0.4kg$, $b = 1.2Ns/m$, $k = 32N/m$, $G = 0.32$ and $\omega_n = 1.423$	Legend (19) in Figure 5.4
		Higher Imp. Gain	$m_2 = 1.0kg$, $b = 3.0Ns/m$, $k = 80N/m$, $G = 0.32$ and $\omega_n = 1.423$	Legend (20) in Figure 5.4
		Low Imp. Gain	$m_2 = 0.6kg$, $b = 1.8Ns/m$, $k = 48N/m$, $G = 0.32$ and $\omega_n = 1.423$	Legend (21) in Figure 5.4
Seating 6	Equivalent Impedance TF	High Freq. Nominal	$m_2 = 0.8kg$, $b = 2.4Ns/m$, $k = 64N/m$, $G = 0.32$ and $\omega_n = 1.423$	Legend (1) in Figure 5.4
		Lowest Pos. Gain	$m_2 = 3.2kg$, $b = 9.6Ns/m$, $k = 256N/m$, $G = 0.08$ and $\omega_n = 1.423$	Legend (22) in Figure 5.4
		Lower Pos. Gain	$m_2 = 1.6kg$, $b = 4.8Ns/m$, $k = 128N/m$, $G = 0.16$ and $\omega_n = 1.423$	Legend (23) in Figure 5.4
		Higher Pos. Gain	$m_2 = 0.4kg$, $b = 1.2Ns/m$, $k = 32N/m$, $G = 0.64$ and $\omega_n = 1.423$	Legend (24) in Figure 5.4
		Highest Pos. Gain	$m_2 = 0.2kg$, $b = 0.6Ns/m$, $k = 16N/m$, $G = 1.28$ and $\omega_n = 1.423$	Legend (25) in Figure 5.4

A catch-trial experiment was conducted to test the effect of system parameters on rate of human adaptation. To do so, participants were overtrained with a nominal system of 1 Hz natural frequency and their adaptation to 1.4 Hz target natural frequency was tested, so that the experiments are compatible with the existing literature on human motor control of second order dynamic systems [170, 171]. Details of the experiment design are presented in Figure 5.3 and Table 5.1.

The experiment consisted of six seatings, each of which focused on a different set of parameter variations at the target frequency. Figure 5.4 presents the magnitude Bode plots of the position and impedance transfer functions for each seating. In particular, the gain value G of the transfer functions was changed in Seating 1, while the damping coefficient ζ was altered in Seating 2. In Seating 3, both the gain and damping parameters were changed simultaneously to check coupled effects. In Seating 4, the parameters were adjusted such that the peaks of the magnitude Bode plots

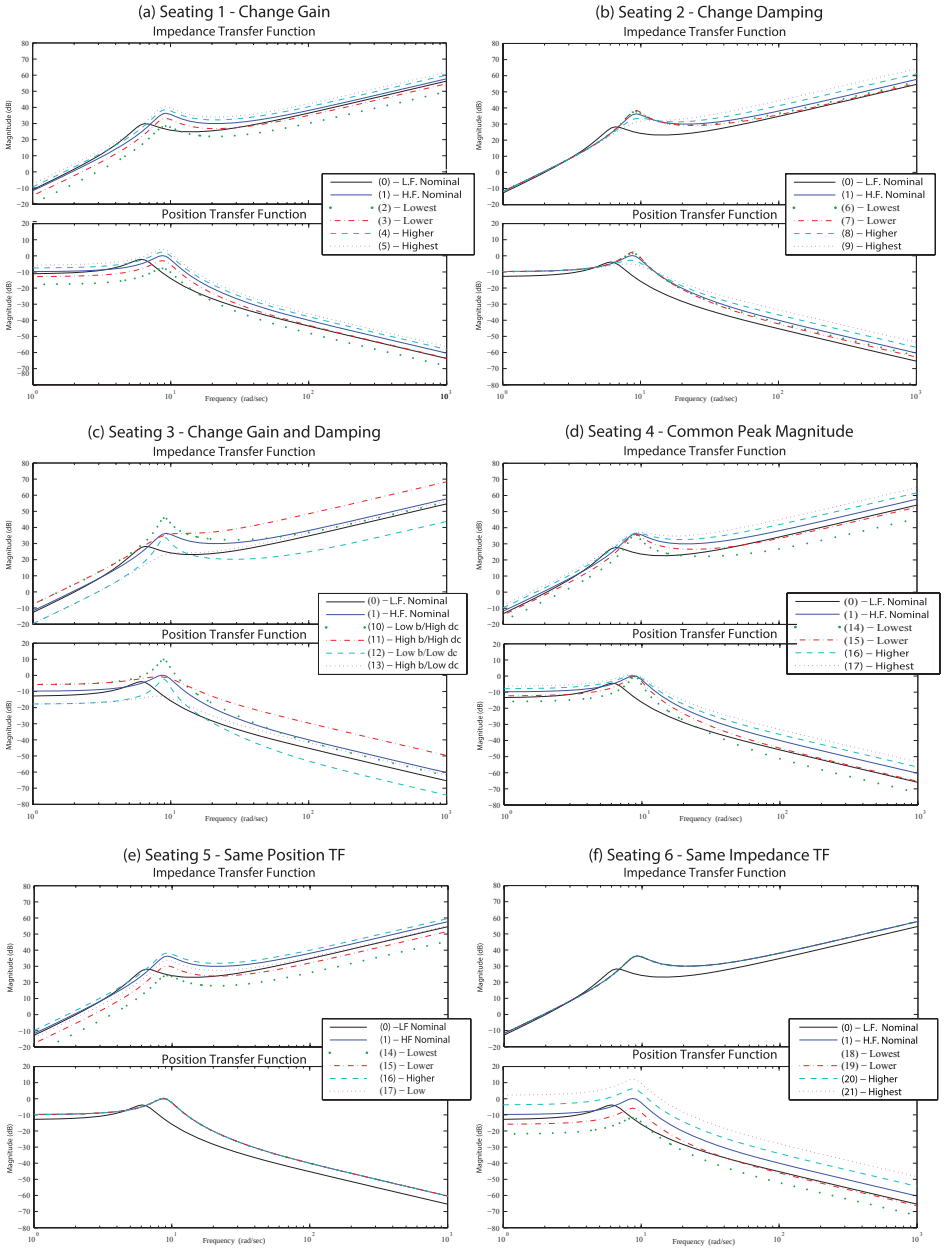

Figure 5.4: Magnitude Bode plots of the virtual systems used in the experiment. Impedance transfer functions of each system are plotted with the parameters given in Table 5.1.

were matched while the different damping ratios were set to investigate effect of different slopes on the magnitude plot.

All these four sets include the variation of either single parameter (gain value, damping) or both of these parameters, while remaining two seatings get use of equivalent systems for position and impedance transfer functions by modifying multiple variable (gain value, damping, stiffness and mass) at once. In particular, in Seating 5 parameters are modified such that impedance transfer function (Eqn. (5.4)) is varied while position transfer function while position transfer function (Eqn. (5.3)) is kept the same and exact opposite is applied in Seating 6. Note that the use of modified equivalent transfer functions for force and vision feedback provides a unique advantage over using visual only and haptic only test procedures. In particular, implemented virtual exercise resembles a task in daily life activities which inherits both of the haptic and visual feedbacks, while quantitative effect factors of each feedback can be analyzed separately due to varying feedback values. Table 5.1 lists each seating, the effect levels, the system parameters used to implement the virtual systems and the location of the related magnitude Bode plots of position and impedance transfer functions (Eqns. (5.3) and (5.4), respectively).

Our purpose in this study is to analyze the behavior of human motor control system on a catch-based rhythmic dynamic task while system parameters are changed to have different characteristics in terms of their impedance transfer functions. In that regard, all six Seatings designed such that not only possible cross-validations can be performed, the major factor on overlapping effects in a Seating can also be identified. Two parameter sets are chosen identical in each Seating, normal and high frequency nominals, and remaining parameter deviations are set relatively close throughout each Seating while maintaining as large parameter variations as possible limited by the physical hardware.

At the start of each seating, participants were trained with an intense learning session (denoted with L in Figure 5.3) before catch trials were administered. On the first day, the learning session consisted of 40 trials of 10 seconds each with the nominal second order system of 1 Hz natural frequency, while on the later days of testing, 20 learning trials were completed, since it was sufficient to reach the same performance level achieved at the end of the first day. However, if the excitation frequencies for 8 out of last 10 trials were not within the 5-percent performance range, then the participants were asked to complete 10 more trials until the performance goal was met. All participants understood the task in the first 10 to 20 trials and were consistently exciting the nominal system at its natural frequency. Feedback about the performance of the participant was provided at every trial in learning session to correct any possible bias in the adaptation procedure. To provide feedback, frequency of excitation of the participant was compared with the natural frequency of the 1 Hz nominal system. A message indicating if oscillation frequency was greater than, lower than or within 5 percent of the system natural frequency was displayed so that the participant could increase, decrease or maintain their input frequency.

At each seating, following the completion of the learning session L, participants attended catch trial sessions (shown as $C1$ to $C6$ in Figure 5.3). There existed 5 different parameter sets in each seating, which were randomly presented to the user within a block (five consecutive catch trials) of the experiment. These parameter sets are indicated by the five frequency response plots in each panel of Figure 5.4. Repetition of this block for ten times in every catch session resulted in 50 trial sets. Between every block, a learning set trial was administered to the user with feedback provided, in order to help wash out the effects of catch trials. Each catch trial lasted

20 seconds; for the first 10 seconds the participants excited the nominal system at 1 Hz. After this, the virtual system parameters were changed to one of the randomly selected parameter sets of the appropriate seating with a natural frequency of 1.4 Hz. The participants adapted to the new dynamics at 1.4 Hz and excited this new system within the next 10 seconds of the catch trial.

5.1.5 Data Analysis

Displacement and velocity data of end effector (m_1) and m_2 were collected at 500 Hz during every trial. For 20 seconds of trials, a total of 10000 data points are acquired for each parameter set for every catch session. The hand excitation data was processed in Matlab using time-frequency scripts[2]. The preprocessed data was down sampled to 50 Hz and then passed through a 129-point Hamming window. The spectrogram (time-frequency trajectories) profiles were obtained and the frequencies with the maximum power content at each instant of time were extracted. A plot of frequency as a function of the duration of a catch trial is given in Figure 5.5. One can observe the variation of hand excitation frequency while adapting from the 1 Hz nominal system to the 1.4 Hz target system.

The goal of each catch session is to evaluate the effect of particular parameter sets on adaptation of hand excitation frequency between nominal and target system, primarily focusing on rate of adaptation and steady state error. Since each set of parameters was provided to participants for ten times in a catch session, average value of the recorded data for each set was taken after calculating frequencies with maximum power content at every time instant. Subsequently, an exponential fit with three parameters (L_0,

[2]Available at http://tftb.nongnu.org/ for download

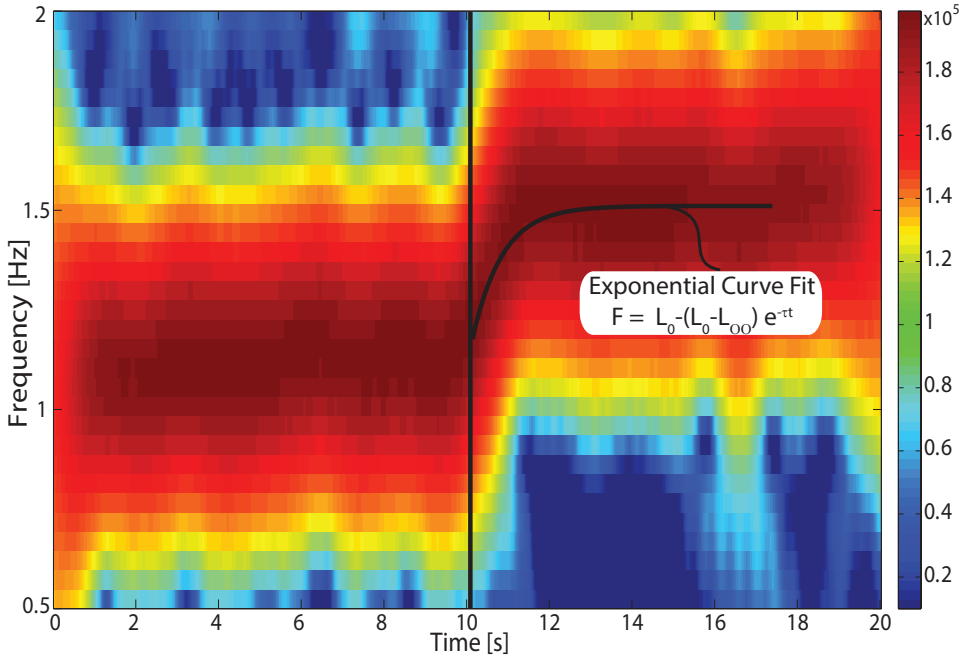

Figure 5.5: Frequency spectrum as a function of time for a sample catch trial. Exponential fit for the trial is also presented.

L_∞ and τ) was performed according to the formula: $F = L_0 - (L_0 - L_\infty)\, e^{-\tau\, t}$. In this equation, L_0 represents the starting frequency, L_∞ is the steady state value after adaptation, while τ (the time constant of the exponential function) models the rate of adaptation. Since the change in parameters were administered at the 10th second of a catch trial, the exponential curves were fitted on the data starting from this instant. To determine the L_0 parameter, the average frequency of excitation between the 8th and 10th seconds of the catch trial were used. Remaining two parameters are used in order to determine the performance metrics in the experiment. Steady state error shows the deviation from the given damped natural frequency after catch, while rate of adaptation parameter is directly τ.

One factor repeated measure ANOVAs (Analysis of Variance) were used to determine significant differences ($\alpha = 0.05$) among the five sys-

tems in each seating conditions. Multiple pair wise comparisons were performed by using Bonferroni Confidence interval adjustments.

5.2 Results

For ten seconds in every trial, the parameter set for low frequency was used which was overtrained by the participant. After these ten seconds, a catch occurred where the system parameters were altered to present a system with higher frequency response. Data acquired from all sessions were processed as detailed in subsection 5.1.5, and performance measures were analyzed in order to examine the human response to system dynamics alteration; the rate of adaptation is (τ) and the steady state excitation frequency for the catch system (L_∞). A third variable L_0 measures the steady state excitation frequency for the overtrained 1 Hz nominal system dynamics. For each of the catch trials, L_0 values were observed to be within the JND value of 1 Hz (within ±4% of 1 Hz).

5.2.1 Seating 1 – Varying Gain

In Seating 1, the effects of changing gain G on human adaptation was studied. Two target systems with higher and two target systems with lower gain values than the high frequency nominal system were tested. The parameters for the four target systems are summarized in Table 5.1. The Bode plots of target systems are given in Figure 5.4 (a).

It was hypothesized that increasing the gain will decrease steady state error while increasing the time of convergence. Results indicate that the change of gain G has no statistically significant effect on the steady state frequency values, L_∞ $[F(4, 24) = 0.9; p = 0.47]$. However, the rates of adaptation are significantly affected by altered gain values.

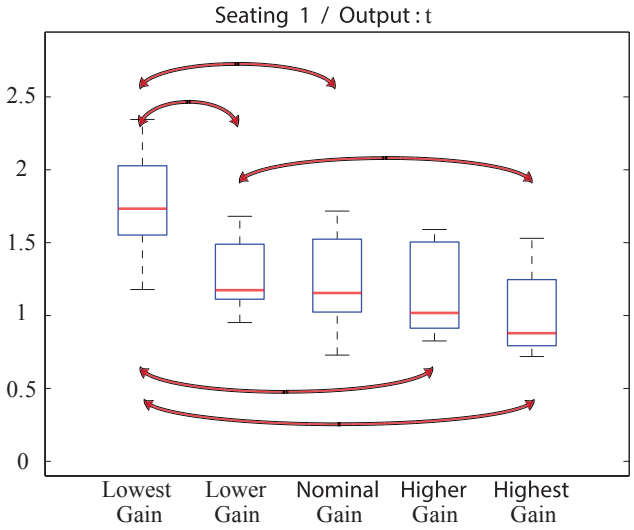

Figure 5.6: Box plots for Seating 1 for varying gain G values. Statistically significant pairs with $p < 0.05$ are marked.

Figure 5.6 presents the rate of adaptation results for Seating 1. In particular, box plots of τ values are shown for each level of gain parameter and statistically significant interactions with $p < 0.05$ are marked. There is a significant difference in the adaptation rates for 'lowest' gain level and all other gain levels. There are also significant differences in the adaptation rates between 'lower' and 'highest' gain levels. Systems with intermediate gain values were not significantly different from each other in terms of adaptation rates; however, there exists an overall trend for the mean values indicating a monotonic decrease of adaptation rates as the gain is increased.

The fact that the change in gain does not effect L_∞ values is in agreement with the recent findings in the literature [170] which state that humans can robustly identify the natural frequency of a second order system and excite it at this natural frequency even when the magnitude cues are changed. On the other hand, the adaptation rate is significantly affected in such a way

that the rate of adaptation decreases as the gain is increased. Since, when the gain is increased, the required effort to complete the task increases, the decrease in adaptation rate can be attributed to the inherent trade-off between task performance and effort in human motor control.

5.2.2 Seating 2 – Varying Damping

The second seating studied effects of the changing the damping ratio b of the system. Two target systems with higher and two target systems with lower damping ratios than the high frequency nominal system were tested. The parameters for the four target systems are summarized in Table 5.1. The Bode plots of target systems are given in Figure 5.4 (b).

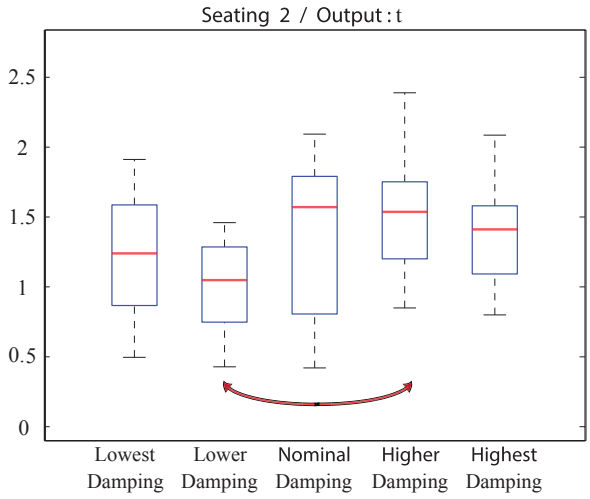

Figure 5.7: Box plots for Seating 2 for varying damping ζ values. Statistically significant pairs with $p < 0.05$ are marked.

It was hypothesized that increasing the damping will have a stabilizing effect on human motor control, while perception of the natural frequency will be diminished. Results indicate that all of steady state frequency values L_∞ except for the 'highest' damping level are within the JND at 1.4 Hz. There exists a statistically significant difference with $p < 0.05$ in

the L_∞ value for 'highest' damping set and all other sets. In particular, participants overshoot the target frequency with an average error of 0.16 Hz with the 'highest' damping level.

Figure 5.7 depicts the rate of adaptation results for Seating 2. In particular, box plots of τ values are shown for each level of damping parameter and statistically significant interactions with $p < 0.05$ are marked. There exists a statistically significant difference between adaptation rates with 'lower' and 'higher' damping levels, indicating faster adaptation with the increased damping level. The mean values of adaptation rates exhibit a monotonically increasing trend as the damping is increased from 'lower' to 'higher' level. The adaptation rates seem to saturate out of these levels, that is, the monotonic trend flattens at extremes. In particular, the means of 'lowest' and 'lower' levels and the means of 'highest' and 'high' levels stay close to each other.

The steady state frequency overshoot with the 'highest' damping level may be attributed to decreased human perception due to the diminished peak of the magnitude Bode transfer function. The increase of the rate of adaptation as the damping is increased within a certain range may be attributed to the stabilizing effects of damping beneficially affecting the human excitation.

5.2.3 Seating 3 – Varying Gain & Damping

Seating 3 investigated aggregated effects of simultaneous changes in damping and the gain parameters of the system. In addition to the high frequency nominal parameter set, the test conditions included lower damping, higher gain (low b / high G); higher damping, higher gain (high b / high G); lower damping, lower gain (low b / low G) and higher damping,

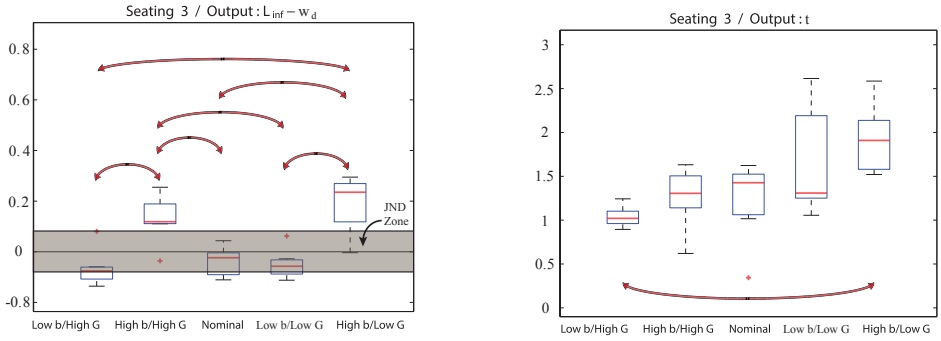

Figure 5.8: Box plots for Seating 3 for varying gain G and damping ζ parameters simultaneously. Statistically significant pairs with $p < 0.05$ are marked.

lower gain (high b / low G) systems. The parameters for the four target systems are summarized in Table 5.1. The Bode plots of target systems are given in Figure 5.4 (c).

Figure 5.8 depicts steady state frequency and the rate of adaptation results for Seating 3. In particular, box plots of L_∞ and τ values are shown for each level of damping parameter and statistically significant interactions with $p < 0.05$ are marked. The experiment results indicate that the steady state frequency for the nominal parameter set and the parameter sets with 'low' damping values fall within JND at 1.4 Hz. However, the parameter sets with 'high' damping values overshoot the steady state frequency regardless of the value of the gain parameters. The difference among the 'low' and 'high' damping sets are statistically significant. The rate of adaptation results indicate a statistically significant difference between opposite pairs of parameters, with 'low damping-high gain' parameter set exhibiting a lower rate of adaptation than 'high damping-low gain' set. There also exists a trend among 'low' gain and 'high' gain parameter sets, indicating lower adaptation rates for high gain systems when compared to low gain ones.

The steady state frequency results are consistent with Seating 2, and the overshoot may be attributed to the effect of damping on the magnitude transfer function and impact on human perception. The adaptation rate results are consistent with Seating 1, confirming that as the gain (required effort for the task) increases, the task performance decreases.

5.2.4 Seating 4 – Common Peak Magnitude

In Seating 4, the parameters were adjusted such that the peaks of the magnitude Bode plots were matched at the natural frequency of the target systems, while different damping ratios were set to test effect of different slopes on the magnitude plots. Two target systems with 'higher' and two target systems with 'lower' damping (slope) than the high frequency nominal system were tested. The parameters for the four target systems are summarized in Table 5.1. The Bode plots of target systems are given in Figure 5.4 (d).

Results indicate that all of steady state frequency values L_∞ are within the JND at 1.4 Hz. Similarly, there exists no statistically significant difference in the τ values among the parameter sets [$F(4, 24) = 0.19; p = 0.94$].

These results are consistent with the previous results, providing evidence that the gain of the Bode magnitude plots is an important factor effecting the rate of adaptation. The results also indicate that when the gains of the systems are normalized around the operating point (natural frequency of the target system), the effect of damping parameter is insignificant for the tested range of damping values.

5.2.5 Seating 5 – Equivalent Position TF

In Seating 5, the effect of the haptic feedback is examined as parameter changes occur such that position transfer function is kept the same while the impedance transfer functions are scaled. This experiment condition is equivalent to testing a single set of visual feedback with several levels of force feedback. The parameters for the four target systems are summarized in Table 5.1. The Bode plots of target systems are given in Figure 5.4 (e).

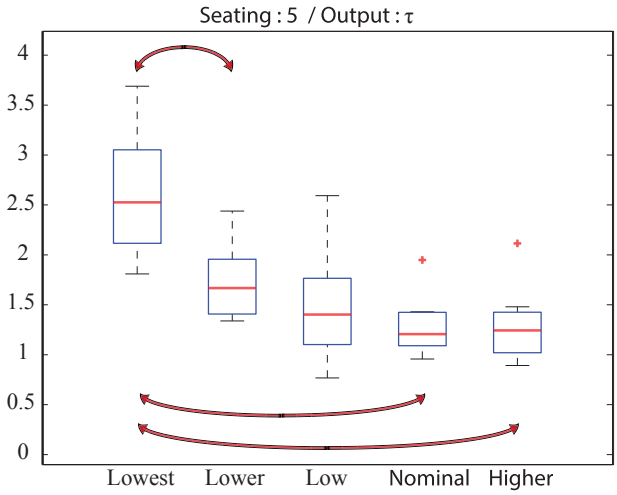

Figure 5.9: Box plots for Seating 5 for varying impedance transfer function. Statistically significant pairs with $p < 0.01$ are marked.

Outcomes of Seating 1 provides inside to the possible results of changing impedance value. It is expected to observe decreased efficiency with increasing impedance value especially in rate of adaptation due to increased effort, however, steady state results are expected to be indifferent. However, results of this seating is prone to additional analysis over the dominant factor since equivalent transfer function for position feedback is used.

Results indicate that steady state frequency values L_∞ fall within the

JND similar to Seating 4 and rate of adaptation performance is given in Figure 5.9.For rate of adaptation performance, there exist a statistically significant trend with $F(4, 24) = 18.433$, $p < 0.01$ such that performance decreases with increased impedance transfer function as predicted. If the experiments continued with higher impedance values (not applicable due to hardware limitations and actuator saturations), there should be more significant results between lower, nominal and parameter sets stronger than 'Higher'. This decrease in adaptation rate can be attributed to the inherent trade-off between task performance and effort in human motor control since the required effort to complete the task increases. This result is more strong than outcomes of Seating 1, since the effect of visual cues are normalized thanks to use of systems with equivalent position transfer functions.

5.2.6 Seating 6 – Equivalent Force TF

In Seating 6, parameters of the system are changed such that impedance transfer function is kept constant while different position transfer functions are applied. In contrast to Seating 5, this experiment condition is equivalent to testing a single level of rendered forces for scaled levels of visual feedback. The values of the parameter sets are summarized in Table 5.1 with bode plots given in Figure 5.4 (f).

Results indicate that there exist no statistically significance for steady state frequency values L_∞ $F(4, 24) = 0.879$; $p = 0.491$ with all values fall within the JND at 1.4 Hz and for rate of adaptation with $F(4, 24) = 1.142$; $p = 0.361$.

The adaptation rate is not significantly affected by visual scaling, which indicates that haptic feedback is the dominant factor in determining rate of

adaptation. Seatings 5 and 6 propose that state information obtained from visual feedback is not main factor of adaptation in fast rhythmic tasks, although it has been expected to be the most dominant information for adapting a point to point reaching dynamic task in [169].

5.3 Remarks and General Discussion

The experiments focus on adaptation (capabilities or rate) with a within trial catch experiments in a rhythmic dynamic exercise. In such a task, choice of a performance metric is highly important. It should be noted that the nature of the assignment does not involve positional constraints, on the contrary, participants are asked to excite the system at its natural frequency, therefore, this approach remains different than cyclic exercises where deviation from desired contour becomes an important metric.

5.3.1 Rate of adaptation

Information obtained from rate of adaptation metric can be extended to be used in haptic interaction which facilitates fast adaptation between states. Use of similar metrics can be observed in previous works in other between trials catch experiments [172, 173, 174]. In particular, error correction rate along trials or the time constant of dis-adaptation for subjects in a perpendicular field environment are thoroughly analyzed for parametrically perturbed reaching exercise.

This study provides a unique perspective over some of the underlying principles of human motor control system over the effects of haptic and position feedbacks in adaptation to a dynamics rhythmic task. In that regard, equivalent system trials are implemented in Seating 5 and 6 which gradually changes only one of the feedback type, keeping the information

obtained from the other channel constant. This approach provides unique advantages such as enabling quantitative measurements on the use of each feedback separately, therefore, resulting a better comparison possibility over the dominance of haptic or visual feedback. Moreover, it inherits resemblance to real life applications which would naturally have both stimuli.

In details, visual cues of the object can only be obtained from the simulation environment provided, therefore, modification in position transfer functions maps one to one to the position and velocity information of the object obtained by the user. In this regard, result of Seating 6 indicates that when the force feedback provided to the user is kept constant, change in the position transfer function, in other words, modification of visual cues, do not significantly affect the performance of the user in a fast paced repetitive dynamic task. On the other hand, adaptation rate values on Seating 1 with increased Gain parameter and in Seating 5 with varying impedance transfer function, point out a effort-performance trade-off with result of Seating 5 being more strong due to the use of equivalent transfer functions. In literature, it has been previously shown that haptic feedback is essential for learning a similar dynamic task [175], however, our results indicates that dominance of this feedback should be monitored due the significantly diminished performance with increased levels.

This trade-off is previously analyzed for reaching tasks in literature. For example, in [176] an algorithm based on concurrent optimization of stability, error, and activation at the muscle level is shown to be capable of representing the adaptation stage of CNS in a perturbed task under velocity-dependent and divergent force fields. It is discussed that perseverance of energy consumption levels by reducing feedforward commands

of this learning scheme after errors fall below a threshold shows the capability of the model to inherit the trade-off between performance and cost of muscle activations. Similarly, in [177], complex hand velocity profiles and nearly smooth object trajectory are modeled based on this trade-off between effort and accuracy which is shown to be capable of providing accurate features of dynamic point-to-point reaching movement.

When each Seating is considered, not only Seating 1 and 5 but results of relevant experiments are not conflicting, on the contrary, they are supporting each other. For example, this effort/performance trade-off is existent in Seatings with increased magnitudes in force transfer functions around operating frequency, however, changing the slope of the responses while keeping the same peak (Seating 4) does not affect the performance of the participant. In order to support the outcomes of frequency based analysis, further data processing based on the magnitudes force applied to the user and position of the hand after catch is performed. Power applied to the system after catch in Seatings 1 and 5 is demonstrated in Figure 5.10. They are ordered from lowest force gain to highest around operating frequency.

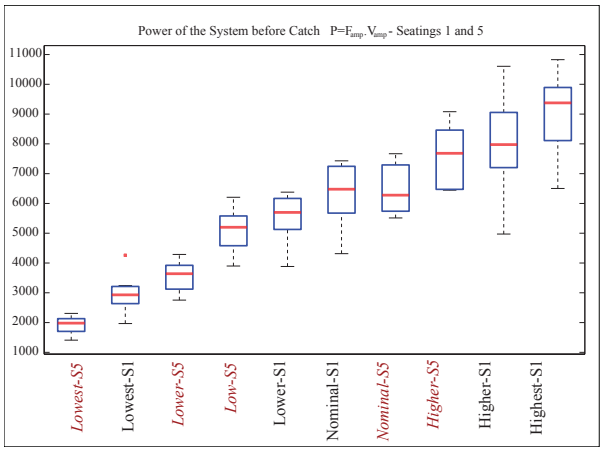

Figure 5.10: Box plots of power magnitudes for Seatings with major force gain change.

Power magnitudes results for each parameter set given in 5.10 shows that they are inversely correlated with the rate of adaptation values for respective sets. In particular, with increased power magnitude after catch for each parameter set, rate of adaptation to the new frequency value at that trial is worsened.

5.4 Steady State Error

Steady state error with respect to the desired frequency value is a generally used metric to evaluate the performance of the participant in frequency domain [175, 171, 170]. Therefore with the use of this metric, not only we can quantify the robustness of human motor control system under different parameter set variations, it also provides a comparison medium with previous literature. Similar to their results, participants are capable of successfully accomplishing the given assignment; performing system identification and then exciting the virtual dynamic system near its resonant frequency within just-noticeable-difference (JND) band, where experiment results show that there is no statistically significant steady state error in Seatings beside a few cases with high damping ratios.

Regarding the Seatings with high damping ratio deviations, it should be noted that this trend is consistent within Seatings 2 and 3, therefore providing a strong evidence for a characteristic behavior rather than a glitch. However, this behavior is not existent in a common peak system (Seating 4) where transfer functions have a common peak with varying slopes, or in Seating 1, where they have same slope with varying peak values. Further discussions can be made after a quick peek at relevant literature over the effects of high damping parameters in adaptation or learning. To our regret, damping characteristic is either omitted or implemented with low

damping ratio in dynamic task studies. Moreover, most of these experiments are dynamic reaching exercises where the performance metrics are chosen as the spatial error from the desired end-effector location, in which case subjects tend to overshoot stationary point to point reaching exercise targets while they are under the influence of high damping values [177]. Most similar case is the previous work in [170] which also indicates an overshoot at frequency value with high damping environment compared to the damped natural frequency, although the damping ratio is lower than the highest damping ratios in this study ($\zeta_{High} = 0.2$ in [170], while $\zeta_{Highest} = 0.356$ and $\zeta_{High} = 0.251$ in our study). Based on the fact that priory JND experiments doesn't include effects of the damping ratio over the perception of the natural/damped frequency, this overshoot behavior may be attributed to a new concept damped JND, which consists of a modified JND related to the magnitude of the damping in the environment. Although further analysis is required for a concrete evidence, based on the magnitude bode plots of the Seatings 2 and 3 and steady state errors in corresponding parameter sets, it can be argued that system characteristics become vaguer with high damping values making it harder to identify the desired frequency value. Consequently for higher damping ratio user overshoot the desired value by stopping at a comfortable frequency after inaccurate identification and for lower damping values there exists slight undershooting where it starts to get hard enough to climb up the desired value on force transfer function peak.

To elaborate the results of the damping change experiments, it can be argued that participants are not comfortable with higher or lower damping ratios in the task. In particular, in a band where ratio is near the nominal values, performance of the user at rate of adaptation increases

with increased values because of decreased force requirements with high damping and more stable interaction. However, at cases where there exist high steady state errors, rate of adaptation is also worsened. For high damping values, participants disregard effort considerations for successful completion of task with higher impedance, while at lower damping ratio parameter sets, they loosen their grip in order to compensate for the instability of the system.

Chapter V

6 Conclusions and Future Work

In this thesis, an optimal exoskeleton design and effective human-in-the-loop control frameworks are presented. The overall process is divided to four major stages; optimal design of the mechanism, implementation of safe human-in-the-loop controllers, introduction of a framework for the execution of each therapy sessions, and human subject experiments in order to help designing effective treatment protocols.

During the design process that is exemplified on a forearm-wrist exoskeleton, imperative design requirements of a rehabilitation system are determined as safety and ergonomy of the patient. In particular, during the type selection, since passive coincidence of robot axes and human joint axes is emphasized, a 3R$\underline{\text{P}}$S-$\underline{\text{R}}$ kinematic structure is chosen. In order to increase the performance of the mechanism under human-in-the-loop controllers while facilitating usability and ease of attachment, a multi-criteria optimization is performed. Choice of design variables, which are ratio of radii of two platforms and joint placement angle, becomes as significant as the performance criteria to be optimized. In addition to their obvious effects to kinematic and dynamic performance of exoskeleton, these two variables play a crucial part in the singularity-free workspace volume of the mechanism. Especially making the system asymmetric results in additional singular configurations based on the Grassmann conditions which are not

geometrically possible in the symmetric case. Once the Pareto-optimal design configuration is determined, an additional workspace optimization is conducted that minimizes the physical limitations of the spherical joints to the workspace volume of the mechanism while staying in the singularity free boundary of the optimal design dimensions. The experimental characterization of the implemented device shows 27% larger workspace volume, 32% lower GDI, and 17% increased AII.

The controllers for 3R$\underline{P}$S-$\underline{R}$ mechanism are implemented according to the workspace of the robot which lies in Riemannian manifold $\mathbf{SO}(3)$, using appropriate error metric between desired and actual orientations. Local controllers are utilized based on each stage of a typical rehabilitation treatment. Starting with stricter trajectory position controllers when human is passive, which may be useful to execute the patients movements at early stages of rehabilitation, followed by open loop impedance controllers which can be utilized for administering virtual walls around the forbidden region and providing haptic feedback for virtual environment interactions. Inside these virtual walls, assistance is provided with a controller that favors coordination and synchronization of complex movements rather than the exact timing along the desired path. In particular, for decoupled assistance of task and pace of tracking, a contour tracking controller Passive Velocity Field Control, is utilized that guarantees coupled stability of the robot-patient system. Implementations of each controller is experimentally verified. Moreover, a multi-lateral controller architecture is utilized which is based on local impedance controllers that can provide an environment for multiple agents to interact with altering dominance over the same task. Controller gains of tele-operation system is chosen based on passivity rather than full transparency and experimental validations are

performed. It is shown that this system is a possible candidate for implementing remote therapies, group therapies, remote assistance and bilateral interaction with dynamic virtual environments.

Following the implementation and experimental verification of local controllers, a systematic framework which delivers effective therapeutic exercises is proposed. The major advantage this framework brings is the ability to modify task parameters on the fly, while guaranteeing coupled stability of the patient and robot system. Seamlessly changing the shape of the desired contour, assistance level provided in the contour error direction and speed of contour tracking concurrently or individually during the task execution enables the implementation of repetitive tasks without repeating the same task. Experimental evidence is provided towards the applicability of this system for assist-as-needed based slacking prevention scheme in a systematic and safe manner.

Lastly, due to the similarities of motor learning of a new task with recovery occurring during rehabilitation, to help designing effective treatment protocols, a healthy subject experiment is performed which identifies adaptation properties of human motor control system on rhythmic dynamic tasks. With the use of equivalent transfer functions in catch trials, statistical evidence is provided that haptic feedback is the dominant modality rather than visual feedback. However, determining the level of haptic feedback is essential if faster adaptation rates is desired, since, with increased effort, performance of the volunteers decrease statistically.

For the future, it is planned to extent the results provided in this thesis with comparative healthy subject experiments that investigates the effects of proposed control framework to the long-term learning. Moreover, randomized clinical trials are to be conducted for better validation of the

proposed framework for effective delivery of therapeutic exercises. Outcomes of these experiments would provide valuable information when incorporated into existing rehabilitation treatment protocols.

Appendix A

A Implementation of Grassmann Line Geometry on 3RPS Mechanism

In this appendix, solution of Grassmann conditions are detailed for non-symmetric 3RPS mechanism. Since a grid based search is utilized throughout the design process, intersection detection for conditions with lower dimensions was carried out using a least square based calculation. In particular, for each grid point in the workspace, distance of two line is calculated in order to find if these lines are intersecting in 3D space, regardless of the intersection points.

A.1 Intersection of n Lines in a Least Square Sense

Given a point on lines Pa = $[\mathbf{Pa_1}; \mathbf{Pa_2}; \mathbf{Pa_3}; ...\mathbf{Pa_n}]$ and the direction of unit vectors Si = $[\mathbf{Si_1}; \mathbf{Si_2}; \mathbf{Si_3}; ...\mathbf{Si_n}]$, one can easily calculate a point closest to the given curves in least square sense. Without going into details, the solution of the closest point for n lines can be calculated:

$$P_{int} = \left(\sum (\mathrm{I} - (\mathrm{Si}\,\mathrm{Si}^T)\right)^{-1} * \left(\sum ((\mathrm{I} - (\mathrm{Si}\,\mathrm{Si}^T))\,\mathrm{Pa})\right) \qquad \text{(A-1)}$$

where I is the identity matrix, while Pa and Si are conjoined n by 3 matrices which include three dimensional information for all the lines. Once the closest point is calculated, distance from this point to n line can trivially computed and if this distance value is zero, n lines is shown to be intersecting at the same point P_{int}.

A.2 Dimension 1

Only Plücker lines that can degenerate to a point are the ones that are associated with the prismatic joints ($\mathbf{P_1}$, $\mathbf{P_2}$, $\mathbf{P_3}$), which means link lengths becomes zero. However, in the case of 3RPS-R mechanism, this is not possible due the physical design since the minimum translational value of each link is defined by the motor attachment which is 30 *mm*.

A.3 Dimension 2

A.3.1 Two or more lines form a planar pencil of lines (2b)

This can be achieved when the end-effector plane is parallel to the plane formed by either two of the leg Plücker vectors. In this case, $\mathbf{P_1}$, $\mathbf{P_2}$ and $\mathbf{P_6}$ lines intersect at s_3 point forming a planar pencil of lines. This is also valid of other combinations of two leg vectors and opposing constraint vector; ($\mathbf{P_1}$, $\mathbf{P_3}$, $\mathbf{P_5}$) and ($\mathbf{P_2}$, $\mathbf{P_3}$, $\mathbf{P_4}$).

Following the terminology in subsection A.1, intersection points of three lines can be checked for each triple combinations of Plücker vectors. For example, **Pa** and **Si** vectors in first case would be:

$$\mathrm{Pa} = \begin{bmatrix} \mathbf{r}^{o\,s_1}\,\mathbf{n_1} & \mathbf{r}^{o\,s_1}\,\mathbf{n_2} & \mathbf{r}^{o\,s_1}\,\mathbf{n_3} \\ \mathbf{r}^{o\,s_2}\,\mathbf{n_1} & \mathbf{r}^{o\,s_2}\,\mathbf{n_2} & \mathbf{r}^{o\,s_2}\,\mathbf{n_3} \\ \mathbf{r}^{o\,s_3}\,\mathbf{n_1} & \mathbf{r}^{o\,s_3}\,\mathbf{n_2} & \mathbf{r}^{o\,s_3}\,\mathbf{n_3} \end{bmatrix} \tag{A-2}$$

$$\mathrm{Si} = \begin{bmatrix} \mathbf{P1}\,\mathbf{n_1} & \mathbf{P1}\,\mathbf{n_2} & \mathbf{P1}\,\mathbf{n_3} \\ \mathbf{P2}\,\mathbf{n_1} & \mathbf{P2}\,\mathbf{n_2}s & \mathbf{P2}\,\mathbf{n_3} \\ \mathbf{P6}\,\mathbf{n_1} & \mathbf{P6}\,\mathbf{n_2} & \mathbf{P6}\,\mathbf{n_3} \end{bmatrix} \tag{A-3}$$

A.4 Dimension 3

A.4.1 Find four lines which are on the same regulus (3a)

With the defined Plücker vectors, whatever the configuration of the mechanism, every leg line intersects with corresponding constraint line, while all constraint lines intersects with each other. There can be no forth line within the same regulus [71, 72].

A.4.2 Four lines constitute two flat pencils in distinct planes with a common line (3b)

Not possible since only flat pencil can be generated with the condition 2b, for example with $\mathbf{P_1}$, $\mathbf{P_2}$ and $\mathbf{P_6}$ vectors, where other lines are either coplanar with end-effector ($\mathbf{P_4}$ and $\mathbf{P_5}$) or intersecting at the same point ($\mathbf{P_3}$).

A.4.3 All four lines goes trough the same point (3c)

In configurations where condition 2b is valid, a forth line (remaining leg Plücker vector $\mathbf{P_3}$) is always intersecting three lines of planar pencil at a common point which justifies the condition (3c). Therefore, singular configurations due to 3c is identical to (2b).

A.4.4 All four lines are coplanar (3d)

In order to realize this condition, translational movement of the mechanism should be zero, which is not possible with 3R$\underline{\text{P}}$S-$\underline{\text{R}}$ mechanism.

A.5 Dimension 4

A.5.1 Among the four lines, none of them intersects the regulus created by the other three lines in a proper point (4a)

In 3RPS-R mechanism, the skew line sets can be generated with the leg vectors ($\mathbf{P_1}$, $\mathbf{P_2}$ and $\mathbf{P_3}$). Each of the remaining lines ($\mathbf{P_4}$, $\mathbf{P_5}$ and $\mathbf{P_6}$) intersects at least one of these leg vectors, therefore, we cannot find four vectors that meet the required condition, similar to (3a).

A.5.2 Five lines must pass through two skew lines (4b)

When the Plücker vectors of the mechanism are considered, it is trivial to find a line which intersects four of the given vectors. If the quadruplet of ($\mathbf{P_1}$, $\mathbf{P_4}$, $\mathbf{P_2}$ and $\mathbf{P_5}$) is considered, two lines can be identified which intersects these vectors. The first line β is coplanar to the vector $\mathbf{r}^{s_1\,s_2}$ and passes through corresponding spherical joint centers, while the second line γ is the intersection of planes spanned by the couple of Plücker vectors on each leg. Mathematically,

$$\wp_{14} : \mathbf{P_1}, \mathbf{P_4}$$

$$\wp_{25} : \mathbf{P_2}, \mathbf{P_5}$$

$$\gamma = \wp_{14} \cap \wp_{25}$$

Plane equations for $\wp_{14}$ and $\wp_{14}$ can be written with the normal vectors of each couple of lines ($\mathbf{N_{14}} = \mathbf{P_1} \perp \mathbf{P_4}$, $\mathbf{N_{25}} = \mathbf{P_2} \perp \mathbf{P_5}$) and the intersection point of these two lines which are the spherical joint points $\mathbf{r}^{o\,s_1}$ and $\mathbf{r}^{o\,s_2}$, respectively. Line equation of γ, which is at the intersection of these two

planes can be calculated in two steps. First of all, the direction of the line should be found with cross product of two normal plane equations $\vec{\gamma} = \mathbf{N_{14}} \times \mathbf{N_{25}}$. Afterwards, a point which is common in two planes $M = [M_x, M_y, M_z]$ is to be determined. This point can be chosen as the intersection of these two planes with the base plane created with the point O and the normal vector $\mathbf{n_3}$.

In the end, condition (4b) can be satisfied if $\mathbf{P_3}$ vector intersects with β and γ. This case can be generalized for each leg vector $\mathbf{P_1}$ and $\mathbf{P_2}$ with remaining quadruple of leg and constraint vectors.

Intersection of γ and $\mathbf{P_3}$

Two lines intersects if and only if distance between the two lines is equal to zero which can be calculated bases on subsection A.1:

$$\mathbf{Pa} = \begin{bmatrix} M_x & M_y & M_z \\ \mathbf{r^{O\,S_3}}\,\mathbf{n_1} & \mathbf{r^{O\,S_3}}\,\mathbf{n_2} & \mathbf{r^{O\,S_3}}\,\mathbf{n_3} \end{bmatrix} \tag{A-4}$$

$$\mathbf{Si} = \begin{bmatrix} \vec{\gamma}\,\mathbf{n_1} & \vec{\gamma}\,\mathbf{n_2} & \vec{\gamma}\,\mathbf{n_3} \\ \mathbf{P3}\,\mathbf{n_1} & \mathbf{P3}\,\mathbf{n_2} & \mathbf{P3}\,\mathbf{n_3} \end{bmatrix} \tag{A-5}$$

Intersection of β and $\mathbf{P_3}$

Two lines intersects if and only if distance between the two lines is equal to zero which can be calculated bases on subsection A.1:

$$\mathbf{Pa} = \begin{bmatrix} \mathbf{r^{O\,S_1}}\,\mathbf{n_1} & \mathbf{r^{O\,S_1}}\,\mathbf{n_2} & \mathbf{r^{O\,S_1}}\,\mathbf{n_3} \\ \mathbf{r^{O\,S_3}}\,\mathbf{n_1} & \mathbf{r^{O\,S_3}}\,\mathbf{n_2} & \mathbf{r^{O\,S_3}}\,\mathbf{n_3} \end{bmatrix} \tag{A-6}$$

$$\mathbf{Si} = \begin{bmatrix} \mathbf{r^{\vec{S_1S_2}}}\,\mathbf{n_1} & \mathbf{r^{\vec{S_1S_2}}}\,\mathbf{n_2} & \mathbf{r^{\vec{S_1S_2}}}\,\mathbf{n_3} \\ \mathbf{P3}\,\mathbf{n_1} & \mathbf{P3}\,\mathbf{n_2} & \mathbf{P3}\,\mathbf{n_3} \end{bmatrix} \tag{A-7}$$

where $\mathbf{r}^{\vec{s_1 s_2}}$ is the normalized vector.

In order to examine the configurations which are singular according to (4b), both distances should be zero simultaneously.

A.5.3 All lines belong to union of three planar pencil of lines in different planes with a common line (4c)

When the (3b) condition is reviewed, it can be seen that this condition cannot be met for the 3RPS-R device.

A.5.4 All five lines are on a plane, or pass through one point of this plane (4d)

This case has multiple possibilities. Fist one is the five coplanar lines. From the device geometry, it is obvious that we cannot have five coplanar lines. Next condition is four coplanar lines and one line with a certain point on that plane. This case is identical to (3d) and can be only valid for zero translation, which is not possible. The last case is the three coplanar lines and two lines intersecting a point on the plane. We know that the three constraint vectors are coplanar, however, the intersection point for each couple of leg vectors can be on this plane only for zero translation value where end-effector plane is identical with the base plane. This is also valid for coplanar leg vectors and it is not realizable in 3RPS-R. If the two constraint lines and one leg line are chosen as coplanar, for example $\mathbf{P_1}$, $\mathbf{P_4}$ and $\mathbf{P_5}$, two vectors can be found which intersects this plane at the same point ($\mathbf{P_3}$ and $\mathbf{P_6}$ intersecting at s_3). However this case is identical to the condition (2b) in this mechanism.

A.6 Dimension 5

A.6.1 Six lines span a general complex (5a)

Four planes are to be constructed for this condition. The first three planes are spanned by couple Plücker vectors, ($\wp_{14}$: $\mathbf{P_1}$, $\mathbf{P_4}$),($\wp_{25}$: $\mathbf{P_2}$, $\mathbf{P_5}$) and ($\wp_{36}$: $\mathbf{P_3}$, $\mathbf{P_6}$), while last plane is the plane of the moving platform ($\wp_E$). Moreover, lets denote the intersection of moving platform plane with each planes as $\mathbf{l_1}$,$\mathbf{l_2}$ and $\mathbf{l_3}$, where

$$\mathbf{l_1} = \wp_{14} \cap \wp_E$$

$$\mathbf{l_2} = \wp_{25} \cap \wp_E$$

$$\mathbf{l_3} = \wp_{36} \cap \wp_E$$

If six lines belong to a non-singular complex, then lines $\mathbf{l_1}$,$\mathbf{l_2}$ and $\mathbf{l_3}$, which belongs to the pencil of lines that are spanned by the lines of the complex, should also belong to this complex with a common point on the moving platform. Note that this case is identical to the methodology in [74] where twist motion of the end-effector is analyzed while all the active pairs are locked. Three velocities of the three points not at a common line defines a twist if intersection point of the three normal planes of these velocity vectors lies in the plane determined by the three points. In other words, if the intersection of the three normal planes of the velocity vectors for the s_i points lies on the plane defined by these connection points(end-effector plane), these positions/orientations of the mechanism are singular. In other words, if the intersection of the three normal planes of the velocity vectors for the s_i points lies on the plane defined by these connection points(end-effector plane), these positions/orientations of the mechanism are singular.

In the case of the 3R$\underline{\text{P}}$S-$\underline{\text{R}}$ mechanism, normal plane equations of the

velocity vectors can be formed from the general plane equation from a normal vector as:

$$0 = \boldsymbol{\eta_i}\,(\mathrm{R} - \mathbf{r}^{\mathbf{o}\,\mathbf{s_i}}) \tag{A-8}$$

where $\boldsymbol{\eta_i}$ is the unit vector in the direction of the velocity of the each limb, while R is the set of all points which satisfies the plane equations. Another representation would be:

$$\begin{aligned} 0 = \boldsymbol{\eta_i}\,\mathbf{n_1}\,[\mathrm{X} - (\mathbf{r}^{\mathbf{o}\,\mathbf{s_i}}\ \mathbf{n_1})] + \boldsymbol{\eta_i}\,\mathbf{n_2}\,[\mathrm{Y} - (\mathbf{r}^{\mathbf{o}\,\mathbf{s_i}}\ \mathbf{n_2})] \\ + \boldsymbol{\eta_i}\,\mathbf{n_3}\,[\mathrm{Z} - (\mathbf{r}^{\mathbf{o}\,\mathbf{s_i}}\ \mathbf{n_3})] \end{aligned} \tag{A-9}$$

X, Y, and Z are the coordinates of R set in each coordinate axes of Newtonian frame. Note that scalar multiplications define the corresponding measure number of the vectors for each axes.

After normal plane equations of the velocity vectors are formed, next step is to find the intersection of these planes and search for the points that takes this intersection point on the plane formed on the end-effector with the formula given below:

$$0 = \begin{vmatrix} X - x_1 & Y - y_1 & Z - z_1 \\ x_2 - x_1 & y_2 - y_1 & z_2 - z_1 \\ x_3 - x_2 & y_3 - y_2 & z_3 - z_2 \end{vmatrix} \tag{A-10}$$

where

$$x_1 = (\mathbf{r}^{\mathbf{o}\,\mathbf{s_1}}\ \mathbf{n_1}),\ x_2 = (\mathbf{r}^{\mathbf{o}\,\mathbf{s_2}}\ \mathbf{n_1}),\ x_3 = (\mathbf{r}^{\mathbf{o}\,\mathbf{s_3}}\ \mathbf{n_1})$$

$$y_1 = (\mathbf{r}^{\mathbf{o}\,\mathbf{s_1}}\ \mathbf{n_2}),\ y_2 = (\mathbf{r}^{\mathbf{o}\,\mathbf{s_2}}\ \mathbf{n_2}),\ y_3 = (\mathbf{r}^{\mathbf{o}\,\mathbf{s_3}}\ \mathbf{n_2})$$

$$z_1 = (\mathbf{r}^{\mathbf{o}\,\mathbf{s_1}}\ \mathbf{n_3}),\ z_2 = (\mathbf{r}^{\mathbf{o}\,\mathbf{s_2}}\ \mathbf{n_3}),\ z_3 = (\mathbf{r}^{\mathbf{o}\,\mathbf{s_3}}\ \mathbf{n_3})$$

Eqn. (A-10) shows the singularity equation of the system and is a third degree function of p_3 which states that for each orientation of the mechanism in the workspace, in other words for each ψ_1 and ψ_2 values, there exists three singular position depending on the translational generalized coordinate. These three equations can be solved either with a symbolic manipulator such as Maple or using numerical methods. Numerical method is chosen in this study since it has higher synergy with the grid search over each configuration of the mechanism in the workspace.

A.6.2 Six lines cross the same line in space (5b)

This condition dictates that there exist a line which pass thorough six vectors. Therefore, condition (4b) can provide basis for analysis where it is shown that two lines γ and β can be identified which can intersect corresponding four Plücker vectors ($\mathbf{P_1}$, $\mathbf{P_4}$, $\mathbf{P_2}$ and $\mathbf{P_5}$). Moreover, if the intersection point of one set of lines such as $\mathbf{P_2}$ and $\mathbf{P_5}$ with s_2 point does not lie on the plane spanned by the remaining couple of lines $\wp_{14}$, which is the case in 3R$\underline{\text{P}}$S-$\underline{\text{R}}$ mechanism, a unique line can be found which can intersect all four lines [70]. For that purpose, in order to check the singular configurations according to this special complex, the intersection of the two possible lines γ and $\boldsymbol{\beta}$ with the remaining Plücker vectors $\mathbf{P_3}$ and $\mathbf{P_6}$ should be analyzed.

γ line intersecting with $\mathbf{P_3}$ and $\mathbf{P_6}$

Intersecting conditions of γ with P_3 are already determined in (4b). Intersection of γ and $\mathbf{P_6}$ should be checked similar to the methods in (4b); two lines intersects if and only if distance between the two lines is equal

to zero:

$$Pa = \begin{bmatrix} M_x & M_y & M_z \\ \mathbf{r}^{\mathbf{o}\,\mathbf{s_3}}\,\mathbf{n_1} & \mathbf{r}^{\mathbf{o}\,\mathbf{s_3}}\,\mathbf{n_2} & \mathbf{r}^{\mathbf{o}\,\mathbf{s_3}}\,\mathbf{n_3} \end{bmatrix} \tag{A-11}$$

$$Si = \begin{bmatrix} \vec{\gamma}\,\mathbf{n_1} & \vec{\gamma}\,\mathbf{n_2} & \vec{\gamma}\,\mathbf{n_3} \\ \mathbf{P6}\,\mathbf{n_1} & \mathbf{P6}\,\mathbf{n_2} & \mathbf{P6}\,\mathbf{n_3} \end{bmatrix} \tag{A-12}$$

In order to realize the singularity conditions of (5b) both Eqns. (A-4) and (A-11) should be satisfied.

$\boldsymbol{\beta}$ line intersecting with $\mathbf{P_3}$ and $\mathbf{P_6}$

Intersecting conditions of $\boldsymbol{\beta}$ with P_3 are already determined in (4b). For the analysis of $\mathbf{P_6}$ line, it has been discussed in literature [70] that for a symmetric mechanism, intersection of $\boldsymbol{\beta}$ vector with the $\mathbf{P_6}$ line can only be satisfied in a highly twisted configuration which can not be achieved with the physical structure of 3RPS-R. However, since the implementation is using an asymmetric design with 105.8° connection angle, intersection of not only $\boldsymbol{\beta} = \mathbf{r}^{\mathbf{s_1}\,\mathbf{s_2}}$ with $\mathbf{P_6}$ but also $\mathbf{r}^{\mathbf{s_1}\,\mathbf{s_3}}$ with $\mathbf{P_5}$ is possible for all configuration at asymmetric attached joints. However, this is not possible for the reference leg, where $\mathbf{r}^{\mathbf{s_2}\,\mathbf{s_3}}$) and $\mathbf{P_4}$ only intersects in a unique orientation which is not possible in physical device. However, when translational DoF is increased, singular values are at twisted orientations of the mechanism which are not within the predefined workspace. For lower translational DoF which are not between 125 and 160 there are singular configurations. Therefore, although it irrelevant in our case, one should be careful before using an asymmetric design of 3RPS mechanism due to this condition.

References

[1] Nestor A. Bayona, Jamie Bitensky, Katherine Salter, and Robert Teasell. The role of task-specific training in rehabilitation therapies. Topics in Stroke Rehabilitation, 12(3):58–65, June 2005.

[2] Gert Kwakkel, Robert C Wagenaar, Jos WR Twisk, Gustaaf J Lankhorst, and Johan C Koetsier. Intensity of leg and arm training after primary middle-cerebral-artery stroke: a randomised trial. The Lancet, 354(9174):191 – 196, 1999.

[3] Cathrin Bütefisch, Horst Hummelsheim, Petra Denzler, and Karl-Heinz Mauritz. Repetitive training of isolated movements improves the outcome of motor rehabilitation of the centrally paretic hand. Journal of the Neurological Sciences, 130(1):59 – 68, 1995.

[4] A Sunderland, D J Tinson, E L Bradley, D Fletcher, R Langton Hewer, and D T Wade. Enhanced physical therapy improves recovery of arm function after stroke. a randomised controlled trial. Journal of Neurology, Neurosurgery and Psychiatry, 55(7):530–535, 1992.

[5] Joan M. McDowd, Diane L. Filion, Patricia S. Pohl, Lorie G. Richards, and William Stiers. Attentional abilities and functional outcomes following stroke. The Journals of Gerontology Series B: Psychological Sciences and Social Sciences, 58(1):P45–P53, 2003.

[6] J. Furusho, T. Kikuchi, K. Oda, Y. Ohyama, T. Morita, N. Shichi, Y. Jin, and A. Inoue. A 6-DoF rehabilitation support system for upper limbs including wrists "Robotherapist" with physical therapy. In Proceedings of the IEEE, Netherlands, June 2007. 10th International Conference on Rehabilitation Robotics.

[7] Junji Furusho, Chengqiu Li, Xinghao Hu, Naoto Shichi, Takehito Kikuchi, Akio Inoue, Kenji Nakayama, Yuhei Yamaguchi, and Ushio Ryu. Development of a 6-DoF force display system using ER actuators with high-safety. In VRCIA '06: Proceedings of the 2006 ACM international conference on Virtual reality continuum and its applications, pages 405–408, 2006.

[8] L. Dovat, O. Lambercy, Y. Ruffieux, D. Chapuis, R. Gassert, H. Bleuler, C.L. Teo, and E. Burdet. A haptic knob for rehabilitation of stroke patients. In Proceedings of the 2006 IEEE/RSJ, China, October 2006. International Conference on Intelligent Robots and Systems.

[9] O. Lambercy, L. Dovat, V. Johnson, B. Salman, S. Wong, R. Gassert, T. Milner, T.C Leong, and E. Burdet. Development of a robot-assisted rehabilitation therapy to train hand function for activities of daily living. In Proceedings of the 2007 IEEE, Netherlands, June 2007. International Conference on Rehabilitation Robotics.

[10] J.-C. Metzger, O. Lambercy, Dominique Chapuis, and R. Gassert. Design and characterization of the rehapticknob, a robot for assessment and therapy of hand function. In Intelligent Robots and Systems (IROS), 2011 IEEE/RSJ International Conference on, pages 3074–3080, Sept 2011.

[11] J.-C. Metzger, O. Lambercy, and R. Gassert. High-fidelity rendering of virtual objects with the rehapticknob - novel avenues in robot-assisted rehabilitation of hand function. In Haptics Symposium (HAPTICS), 2012 IEEE, pages 51–56, March 2012.

[12] P. Lammertse, E. Frederiksen, and B. Ruiter. The HapticMaster, a new high-performance haptic interface. In Proceedings of Eurohaptics 2002, Edinburgh, UK, 2002.

[13] M.J. Johnson, K.J. Wisneski, J. Anderson, D. Nathan, and R.O. Smith. Development of ADLER: The Activities of Daily Living Exercise Robot. The First IEEE/RAS-EMBS International Conference on Biomedical Robotics and Biomechatronics, 2006. BioRob ., pages 881–886, 2006.

[14] R U I Loureiro, Farshid Amirabdollahian, Michael Topping, Bart Driessen, and W S Harwin. Upper Limb Robot Mediated Stroke Therapy - GENTLE / s Approach. Autonomous Robots, pages 35–51, 2003.

[15] Stefan Hesse, Gotthard Schulte-tigges, Matthias Konrad, Anita Bardeleben, M Konrad, A Bardeleben, and C Werner. Robot-Assisted Arm Trainer for the Passive and Active Practice of Bilateral Forearm and Wrist Movements in Hemiparetic Subjects. Arch Phys Med Rehabil, 9993(02):915–920, 2003.

[16] Stefan Hesse, C Werner, M Pohl, S Rueckriem, J Mehrholz, and M L Lingnau. Computerized arm training improves the motor control of the severely affected arm after stroke: a single-blinded randomized trial in two centers. Stroke; a journal of cerebral circulation, 36(9):1960–6, September 2005.

[17] Mina Arab Baniasad and A Mechanical Desgin. Wrist-RoboHab : A Robot for Treatment and Evaluation of Brain Injury Patients. Mechanical Engineering, 2011.

[18] Jakob Oblak, Imre Cikajlo, and Zlatko Matjacić. Universal haptic drive: a robot for arm and wrist rehabilitation. IEEE transactions on neural systems and rehabilitation engineering : a publication of the IEEE Engineering in Medicine and Biology Society, 18(3):293–302, June 2010.

[19] J Oblak, I Cikajlo, and Z Matjacic. A universal haptic device for arm and wrist rehabilitation. In Rehabilitation Robotics, 2009. ICORR 2009. IEEE International Conference on, pages 436–441, 2009.

[20] M. Takaiwa and T. Noritsugu. Development of Wrist Rehabilitation Equipment Using Pneumatic Parallel Manipulator. Proceedings of the 2005 IEEE International Conference on Robotics and Automation, (April):2302–2307, 2005.

[21] M. Takaiwa and T. Noritsugu. Wrist rehabilitaion equipment using pneumatic parallel manipulator. In World Automation Congress (WAC), 2010, pages 1 –6, sept. 2010.

[22] T. Nef, M. Mihelj, G. Colombo, and R. Riener. ARMin - robot for rehabilitation of the upper extremities. In Robotics and Automation, 2006. ICRA 2006. Proceedings 2006 IEEE International Conference on, pages 3152–3157, May 2006.

[23] L.Q. Zhang, H.S. Park, and Y. Ren. Developing an intelligent robotic arm for stroke rehabilitation. In Proceedings of the IEEE, Netherlands, June 2007. 10th International Conference on Rehabilitation Robotics.

[24] Yupeng Ren, Sang Hoon Kang, Hyung-Soon Park, Yi-Ning Wu, and Li-Qun Zhang. Developing a multi-joint upper limb exoskeleton

robot for diagnosis, therapy, and outcome evaluation in neurorehabilitation. Neural Systems and Rehabilitation Engineering, IEEE Transactions on, 21(3):490–499, 2013.

[25] H.I. Krebs, B.T. Volpe, M.L Aisen, and N. Hogan. Increasing productivity and quality of care: Robot-aided neuro-rehabilitation. Journal of Rehabilitation Research and Development, 37(6):639–652, November/December 2000.

[26] H.I. Krebs, N. Hogan, M.L Aisen, and B.T. Volpe. Robot-aided neurorehabilitation. IEEE Transactions on Rehabilitation Engineering, 6(1):75–87, March 1998.

[27] J. J. Palazzolo, M. Ferraro, H. I. Krebs, B.T. Volpe D. Lynch, and N. Hogan. Stochastic estimation of arm mechanical impedance during robotic stroke rehabilitation. IEEE Transactions on Neural Systems and Rehabilitation Engineering, 15(1):94–103, March 2007.

[28] N. Rijnveld and H. I. Krebs. Passive wrist joint impedance in flexion - extension and abduction - adduction. In Proceedings of the 2007 IEEE, Neteherlands, June 2007. 10th International Conference on Rehabilitation Robotics.

[29] S. Ueki, H. Kawasaki, S. Ito, Y. Nishimoto, M. Abe, T. Aoki, Y. Ishigure, T. Ojika, and T. Mouri. Development of a hand-assist robot with multi-degrees-of-freedom for rehabilitation therapy. Mechatronics, IEEE/ASME Transactions on, 17(1):136–146, 2012.

[30] E Rocon, J M Belda-Lois, a F Ruiz, M Manto, J C Moreno, and J L Pons. Design and validation of a rehabilitation robotic exoskeleton for tremor assessment and suppression. IEEE transactions on neural

systems and rehabilitation engineering : a publication of the IEEE Engineering in Medicine and Biology Society, 15(3):367–78, September 2007.

[31] J. He, Edward J Koeneman, R.S. Schultz, H. Huang, J. Wanberg, D.E. Herring, Thomas G Sugar, and R. Herman. Design of a Robotic Upper Extremity Repetitive Therapy Device. 9th International Conference on Rehabilitation Robotics, 2005. ICORR 2005., pages 95–98, 2005.

[32] Thomas G Sugar, Jiping He, Edward J Koeneman, Richard Herman, H Huang, Robert S Schultz, D E Herring, J Wanberg, Sivakumar Balasubramanian, Pete Swenson, and Jeffrey a Ward. Design and control of RUPERT: a device for robotic upper extremity repetitive therapy. IEEE transactions on neural systems and rehabilitation engineering : a publication of the IEEE Engineering in Medicine and Biology Society, 15(3):336–46, September 2007.

[33] Stephen J Ball, Ian E Brown, and Stephen H Scott. A planar 3DOF robotic exoskeleton for rehabilitation and assessment. Conference proceedings : ... Annual International Conference of the IEEE Engineering in Medicine and Biology Society. IEEE Engineering in Medicine and Biology Society. Conference, 2007:4024–7, January 2007.

[34] R.a.R.C. Gopura and K. Kiguchi. A human forearm and wrist motion assist exoskeleton robot with EMG-based Fuzzy-neuro control. 2008 2nd IEEE RAS & EMBS International Conference on Biomedical Robotics and Biomechatronics, pages 550–555, October 2008.

[35] Ranathunga a. R. Chandra Gopura and Kazuo Kiguchi. EMG-based control of an exoskeleton robot for human forearm and wrist mo-

tion assist. 2008 IEEE International Conference on Robotics and Automation, pages 731–736, May 2008.

[36] Kazuo Kiguchi. Electromyography (EMG) -signal based fuzzy-neuro control of a 3 degrees of freedom (3doF) exoskeleton robot for human. Science, 37(4):241–248, 2009.

[37] Mohammad H. Rahman, Maarouf Saad, Jean P. Kenne, and Phil Archambault. Modeling and control of a 7DOF exoskeleton robot for arm movements. 2009 IEEE International Conference on Robotics and Biomimetics (ROBIO), pages 245–250, December 2009.

[38] M H Rahman, M Saad, J P Kenné, and P S Archambault. Modeling and Development of an Exoskeleton Robot for Rehabilitation of Wrist Movements. Source, 2010.

[39] N G Tsagarakis and Darwin G Caldwell. Development and Control of a 'Soft-Actuated' Exoskeleton for Use in Physiotherapy and Training. Autonomous Robots, pages 21–33, 2003.

[40] André Schiele and Frans C T van der Helm. Kinematic design to improve ergonomics in human machine interaction. IEEE transactions on neural systems and rehabilitation engineering : a publication of the IEEE Engineering in Medicine and Biology Society, 14(4):456–69, December 2006.

[41] A.U. Pehlivan, Sangyoon Lee, and M.K. O'Malley. Mechanical design of ricewrist-s: A forearm-wrist exoskeleton for stroke and spinal cord injury rehabilitation. In Biomedical Robotics and Biomechatronics (BioRob), 2012 4th IEEE RAS EMBS International Conference on, pages 1573–1578, 2012.

[42] Lorenzo Masia, Maura Casadio, Psiche Giannoni, Giulio Sandini, and Pietro Morasso. Performance adaptive training control strategy for recovering wrist movements in stroke patients: a preliminary, feasibility study. Journal of neuroengineering and rehabilitation, 6:44, January 2009.

[43] Lorenzo Masia, Nestor Nava Rodriguez, Maura Casadio, Pietro Morasso, Giulio Sandini, and Psiche Giannoni. Adaptive Training Strategy of DistalÂ Â Movements by Means of a Wrist-Robot. 2009 Second International Conferences on Advances in Computer-Human Interactions, pages 227–233, February 2009.

[44] J.C. Perry, J. Rosen, and S. Burns. Upper-limb powered exoskeleton design. Mechatronics, IEEE/ASME Transactions on, 12(4):408–417, Aug. 2007.

[45] a. Frisoli, F. Rocchi, S. Marcheschi, a. Dettori, F. Salsedo, and M. Bergamasco. A New Force-Feedback Arm Exoskeleton for Haptic Interaction in Virtual Environments. First Joint Eurohaptics Conference and Symposium on Haptic Interfaces for Virtual Environment and Teleoperator Systems, pages 195–201, 2005.

[46] S. Marcheschi, a. Frisoli, C.a. Avizzano, and M. Bergamasco. A Method for Modeling and Control Complex Tendon Transmissions in Haptic Interfaces. Proceedings of the 2005 IEEE International Conference on Robotics and Automation, (April):1773–1778, 2005.

[47] A Frisoli, L Borelli, A Montagner, S Marcheschi, C Procopio, F Salsedo, M Bergamasco, M C Carboncini, and B Rossi. Robot-mediated arm rehabilitation in Virtual Environments for chronic

stroke patients: A clinical study. In Robotics and Automation, 2008. ICRA 2008. IEEE International Conference on, pages 2465–2470, May 2008.

[48] Yoon Sang Kim, J. Lee, Sooyong Lee, and Munsang Kim. A force reflected exoskeleton-type masterarm for human-robot interaction. Systems, Man and Cybernetics, Part A: Systems and Humans, IEEE Transactions on, 35(2):198–212, March 2005.

[49] G. Yang, H.L. Ho, W. Chen, W. Lin, S.H. Yeo, and M.S. Kurbanhusen. A haptic device wearable on a human arm. In Proceedings of the 2004 IEEE, Singapore, December 2004. Conference on Robotics, Automation and Mechatronics.

[50] G. Yang, W. Lin, M.S. Kurbanhusen, C.B. Pham, and S.H. Yeo. Kinematic design of a 7-DoF cable-driven humanoid arm: a solution-in-nature approach. In Proceedings of the 2005 IEEE/ASME, California, July 2005. International Conference on Advanced Intelligent Mechatronics.

[51] A. Gupta, M.K. O'Malley, V. Patoglu, and C. Burgar. Design, control and performance of RiceWrist: A force feedback wrist exoskeleton for rehabilitation and training. IEEE Transactions on Robotics Research, 27(2):233–251, February 2008.

[52] A. Sledd and M.K. O'Malley. Performance enhancement of a haptic arm exoskeleton. In Haptic Interfaces for Virtual Environment and Teleoperator Systems, 2006 14th Symposium on, pages 375–381, March 2006.

[53] A. Gupta and M.K. O'Malley. Design of a haptic arm exoskeleton for training and rehabilitation. IEEE/ASME Transactions on Mechatronics, 11(3):280–289, June 2006.

[54] Andrew K. Palmer, Frederick W. Werner, Dennis Murphy, and Richard Glisson. Functional wrist motion: A biomechanical study. The Journal of Hand Surgery, 10(1):39 – 46, 1985.

[55] Jaiyoung Ryu, William P. Cooney III, Linda J. Askew, Kai-Nan An, and Edmund Y.S. Chao. Functional ranges of motion of the wrist joint. The Journal of Hand Surgery, 16(3):409 – 419, 1991.

[56] G. Brigstocke, A. Hearnden, and G. Whatling. The functional range of movement of the human wrist. Journal of Hand Surgery (European Volume), 2012.

[57] N. Tsagarakis, D. G. Caldwell, and G. A. Medrano-Cerda. A 7-DoF pneumatic muscle actuator powered exoskeleton. In IEEE International Symposium on Robot and Human Interactive Communication, pages 327–333, 1999.

[58] J.P. Merlet. Parallel Robots. Springer, second edition, 2006.

[59] X. Kong and C. M. Gosselin. Type synthesis of 3-DoF spherical parallel manipulators based on screw theory. In ASME Design Engineering Technical Conferences, 2002.

[60] M. Karouia and J. M. Herve. A family of novel orinetational 3-DoF parallel robots. In CISM-IFToMM Symposium on Robot Design, Dynamics, and Control, pages 359–368, 2002.

[61] R. Di Gregorio. Kinematics of a new spherical parallel manipulator with three equal legs: The 3-URC wrist. Journal of Robotic Systems, 18(5):213–219, 2001.

[62] I. A. Bonev and C. M. Gosselin. Singularity loci of spherical parallel mechanisms. In IEEE International Conference on Robotics and Automation, pages 2957–2962, 2005.

[63] K. M. Lee and D. K. Shah. Kinematic analysis of a three degrees-of-freedom in-parallel actuated manipulator. IEEE Transactions on Robotics and Automation, 4(3):354–360, 1988.

[64] C. H. Liu and S. Cheng. Direct singular positions of 3RPS parallel manipulators. ASME Journal of Mechanical Design, (126):1006–1016, 2004.

[65] A. Gupta and M. K. O'Malley. Design of a haptic arm exoskeleton for training and rehabilitation. IEEE Transactions on Mechatronics, 11(3):280–289, 2006.

[66] A. Gupta, V. Patoglu, M. K. O'Malley, and C. M. Burgar. Design, control and performance of RiceWrist: A force feedback wrist exoskeleton for rehabilitation and training. International Journal of Robotics Research, Special Issue on Machines for Human Assistance and Augmentation, to appear.

[67] Masahiro Takaiwa and Toshiro Noritsugu. Development of Wrist Rehabilitation Equipment Using Pneumatic Parallel Manipulator - Acquisition of P . T .' s Motion and Its Execution for Patient. Computer, 2:34–39, 2009.

[68] Jaime Gallardo, Horacio Orozco, and José Rico. Kinematics of 3-rps parallel manipulators by means of screw theory. The International Journal of Advanced Manufacturing Technology, 36:598–605, 2008.

[69] Thomas R. Kane, Peter W. Likins, and David A. Levinson. Spacecraft Dynamics. McGraw Hill, 1983.

[70] Alexei Sokolov and Paul Xirouchakis. Singularity analysis of a 3-dof parallel manipulator with r-p-s joint structure. Robotica, 24:131–142, 1 2006.

[71] Jean-Pierre Merlet. Parallel manipulators. Part 2 : Theory. Singular configurations and Grassmann geometry. Rapport de recherche RR-0791, INRIA, 1988.

[72] Jean-Pierre Merlet. Singular configurations of parallel manipulators and grassmann geometry. The International Journal of Robotics Research, 8(5):45–56, 1989.

[73] Sameer A. Joshi and Lung-Wen Tsai. Jacobian Analysis of Limited-DOF Parallel Manipulators. Journal of Mechanical Design, 124, 2002.

[74] Yanwen Li, Zhen Huang, and Lumin Wang. The singularity analysis of 3-rps parallel manipulator. ASME Conference Proceedings, 2006(42568):949–955, 2006.

[75] Z. Huang, L. H. Chen, and Y. W. Li. The singularity principle and property of stewart parallel manipulator. Journal of Robotic Systems, 20(4):163–176, 2003.

[76] A. Erdogan, A.C. Satici, and V. Patoglu. Design of a reconfigurable force feedback ankle exoskeleton for physical therapy.

In Reconfigurable Mechanisms and Robots, 2009. ReMAR 2009. ASME/IFToMM International Conference on, pages 400 –408, june 2009.

[77] Ahmetcan Erdogan and Volkan Patoglu. Passive velocity field control of a forearm-wrist rehabilitation robot. In International Conference on Rehabilitation Robotics (ICORR2011), 2011.

[78] Aykut Cihan Satici, Ahmetcan Erdogan, and Volkan Patoglu. A multi-lateral rehabilitation system. Turk. J. Elec. Eng. and Comp. Sci, 19(5):715–723, 2011.

[79] R. Unal and V. Patoglu. Optimal dimensional synthesis of a dual purpose haptic exoskeleton. In Lecture Notes in Computer Science, Springer, 2008.

[80] Nick Colonnese, Sean M. Sketch, and Allison M. Okamura. Closed-loop stiffness and damping accuracy of impedance-type haptic displays. In Haptics Symposium (HAPTICS), 2014 IEEE, pages 97–102, Feb 2014.

[81] I. Nisky, S. Patil, M. H. Hsieh, and A. M. Okamura. Kinematic analysis of motor performance in robot-assisted surgery: A preliminary study. In Medicine Meets Virtual Reality (Studies in Health Technology and Information), volume 184, pages 302–308, 2013.

[82] L. Stocco. Robot design optimization with haptic interface applications.

[83] H. Lipkin and J. Duffy. Hybrid twist and wrench control for a robotic manipulator. Trans. ASME J. Mech. Transm. Automation Design, 110:138–144, 1988.

[84] M. Tandirici, J. Angeles, and F. Ranjbaran. The characteristic point and the characteristic length of robotic manipulators. In Robotics, Spatial Mechanisms, and Mechanical Systems (DE Vol 45), pages 203–208. ASME, September 1992.

[85] O. Ma and J. Angeles. Optimum architecture design of platform manipulators. In Advanced Robotics, 1991. 'Robots in Unstructured Environments', 91 ICAR., Fifth International Conference on, pages 1130–1135 vol.2, 1991.

[86] Mechanism design for global isotropy with applications to haptic interfaces, Dallas, Texas, 1997. Cited By (since 1996): 5.

[87] L.J. Stocco, S. E. Salcudean, and F. Sassani. On the use of scaling matrices for task-specific robot design. Robotics and Automation, IEEE Transactions on, 15(5):958–965, 1999.

[88] Indraneel Das and J. E. Dennis. Normal-boundary intersection: A new method for generating the pareto surface in nonlinear multicriteria optimization problems. SIAM J. on Optimization, 8:631–657, March 1998.

[89] Thomas R. Kane. DYNAMICS: Theory and Application. McGraw-Hill, 1985. pp. 223.

[90] F. Janabi-Sharifi, V. Hayward, and C.-S.J. Chen. Discrete-time adaptive windowing for velocity estimation. Control Systems Technology, IEEE Transactions on, 8(6):1003–1009, Nov 2000.

[91] L. Leonard, D. Sirkett, G. Mullineux, G.E.B Giddins, and A.W. Miles. Development of an in-vivo method of wrist joint motion analysis. Clinical Biomechanics, 20(2):166 – 171, 2005.

[92] Mohammad Esmaeili, Kumudu Gamage, Eugene Tan, and D. Campolo. Ergonomic considerations for anthropomorphic wrist exoskeletons: A simulation study on the effects of joint misalignment. In Intelligent Robots and Systems (IROS), 2011 IEEE/RSJ International Conference on, pages 4905–4910, Sept 2011.

[93] Z. Kadivar, J.L. Sullivan, D.P. Eng, A.U. Pehlivan, M.K. O'Malley, N. Yozbatiran, and G.E. Francisco. Ricewrist robotic device for upper limb training: Feasibility study and case report of two tetraplegic persons with spinal cord injury. International Journal of Biological Engineering, 2(4):27–38, 2012.

[94] R. Campa, K. Camarillo, and L. Arias. Kinematic modeling and control of robot manipulators via unit quaternions: Application to a spherical wrist. In Decision and Control, 2006 45th IEEE Conference on, pages 6474 –6479, 2006.

[95] J.S. Yuan. Closed-loop manipulator control using quaternion feedback. Robotics and Automation, IEEE Journal of, 4(4):434 –440, August 1988.

[96] Ricardo Campa and Hussein De La Torre. Pose control of robot manipulators using different orientation representations: a comparative review. In Proceedings of the 2009 conference on American Control Conference, ACC'09, pages 2855–2860, Piscataway, NJ, USA, 2009. IEEE Press.

[97] Fabrizio Caccavale, Bruno Siciliano, and Luigi Villani. The role of euler parameters in robot control. Asian Journal of Control, 1(1):25–34, 1999.

[98] F. Caccavale and L. Siciliano, B.and Villani. Quaternion-based impedance with nondiagonal stiffness for robot manipulators. In American Control Conference, 1998. Proceedings of the 1998, volume 1, pages 468 –472, June 1998.

[99] Krebs H.I. Rehabilitation robotics: Performance-based progressive robot-assisted therapy. Autonomous Robots, 15:7–20(14), July 2003.

[100] Lance L. Cai, Andy J. Fong, Chad K. Otoshi, Yongqiang Liang, Joel W. Burdick, Roland R. Roy, and V. Reggie Edgerton. Implications of assist-as-needed robotic step training after a complete spinal cord injury on intrinsic strategies of motor learning. J. Neurosci., 26(41):10564–10568, 2006.

[101] A. Duschau-Wicke, J. von Zitzewitz, A. Caprez, L. Lunenburger, and R. Riener. Path control: A method for patient-cooperative robot-aided gait rehabilitation. Neural Systems and Rehabilitation Engineering, IEEE Transactions on, 18(1):38 –48, 2010.

[102] Yanfang Li, Volkan Patoglu, and Marcia K. O'Malley. Negative efficacy of fixed gain error reducing shared control for training in virtual environments. ACM Trans. Appl. Percept., 6:3:1–3:21, February 2009.

[103] Matjaz Mihelj. A novel paradigm for patient-cooperative control of upper-limb rehabilitation robots. Advanced Robotics, 21:843–867(25), August 2007.

[104] Tsu-Chih Chiu. Coordination Control of Multiple Axes Mechanical System: Theory and Experiments. Ph.d. dissertation, Univ. of California,, Dept. of Mechanical Engineering, Berkeley, CA, 1994.

[105] Eugene David Tung. Identification and Control of High-Speed Machine Tools. Ph.d. dissertation, Univ. of California,, Dept. of Mechanical Engineering, Berkeley, CA, 1993.

[106] P.Y. Li and R. Horowitz. Control of smart exercise machines. i. problem formulation and nonadaptive control. Mechatronics, IEEE/ASME Transactions on, 2(4):237 –247, December 1997.

[107] P.Y. Li and R. Horowitz. Passive velocity field control of mechanical manipulators. Robotics and Automation, IEEE Transactions on, 15(4):751 –763, August 1999.

[108] P.Y. Li and R. Horowitz. Passive velocity field control (pvfc). part i. geometry and robustness. Automatic Control, IEEE Transactions on, 46(9):1346 –1359, September 2001.

[109] Dongjun Lee and P.Y. Li. Passive bilateral control and tool dynamics rendering for nonlinear mechanical teleoperators. Robotics, IEEE Transactions on, 21(5):936 – 951, October 2005.

[110] Dongjun Lee and P.Y. Li. Passive bilateral feedforward control of linear dynamically similar teleoperated manipulators. Robotics and Automation, IEEE Transactions on, 19(3):443 – 456, June 2003.

[111] J. Moreno-Valenzuela. On passive velocity field control of robot arms. In Decision and Control, 2006 45th IEEE Conference on, pages 2955 –2960, December 2006.

[112] Javier Moreno-Valenzuela. Velocity field control of robot manipulators by using only position measurements. Journal of the Franklin Institute, 344(8):1021 – 1038, 2007.

[113] Ahmetcan Erdogan and Volkan Patoglu. Online generation of velocity fields for passive contour following. In IEEE World Haptics Conference (WHC2011), 2011.

[114] Jean-Jacques Slotine and Weiping Li. Applied Nonlinear Control. Prentice Hall, October 1990.

[115] N. Sadegh and R.Horowitz. Stability and robustness analysis of a class of adaptive controllers for robotic manipulators. International Journal of Robotics Research, 9(3):74–92, June 1990.

[116] R. Ortega and M. Spong. Adaptive motion control of rigid bodies. Automatica, Nov 1989.

[117] E.B. Dam, M. Koch, and M. Lillholm. Quaternions, interpolation and animation. Technical Report DIKU-TR-98/5, pages 335–348, July 1998.

[118] Fabrizio Caccavale, Bruno Siciliano, , and Luigi Villani. The role of euler parameters in robot control. Asian Journal of Control, 1(1):25–34, March 199.

[119] B. Siciliano, L. Sciavicco, L. Villani, and G. Oriolo. Robotics: Modelling, Planning and Control. Springer, 2009.

[120] P.Y. Li and R. Horowitz. Passive velocity field control of mechanical manipulators. Robotics and Automation, IEEE Transactions on, 15(4):751 –763, aug 1999.

[121] P.Y. Li and R. Horowitz. Passive velocity field control (pvfc). part ii. application to contour following. Automatic Control, IEEE Transactions on, 46(9):1360 –1371, September 2001.

[122] Daniel E. Koditschek. Dynamics and Control of Multibody Systems, Contemporary Mathematics, volume 97, chapter The application of total energy as a Lyapunov function for mechanical control systems, pages 131–157. American Mathematical Society, 1989.

[123] D.E. Koditschek. Total energy for mechanical control systems, in dynamics and control of multibody systems. MS series on Contemporary Mathematics, 97(4):131–157, June 1982.

[124] D.R.J. Chillingworth, J.E. Marsden, and Y.H. Wan. Symmetry and bifurcation in three-dimensional elasticity, part i. Arch. Rational Mech. Analy, 1982.

[125] B. Khademian and K. Hashtrudi-Zaad. A four-channel multilateral shared control architecture for dual-user teleoperation systems. pages 2660–2666, 29 2007-Nov. 2 2007.

[126] Kim C. Stewart, James H. Cauraugh, and Jeffery J. Summers. Bilateral movement training and stroke rehabilitation: A systematic review and meta-analysis. Journal of the Neurological Sciences, 244(1-2):89 – 95, 2006.

[127] JustineLin BroderickHenderson MeredithHale Leigh Anne Latimer, Christopher PaulKeeling. The impact of bilateral therapy on upper limb function after chronic stroke: a systematic review. Disability and Rehabilitation, 32(15):1221 – 1231, 2010.

[128] C.G. Burgar, P.S. Lum, P.C. Shor, and H.F.M. Van der Loos. Development of robots for rehabilitation therapy : The Palo Alto VA/Stanford experience. Journal of Rehabilitation Research and Development, 37(6):663–673, November/December 2000.

[129] R.M. Mahoney, H.F.M. Van der Loos, P.S. Lum, and C.G. Burgar. Robotic stroke therapy assistant. Robotica, 21:33–44, 2003.

[130] Lorie G Richards, Claudia R Senesac, Sandra B Davis, Michelle L Woodbury, and Stephen E Nadeau.

[131] D.J. Reinkensmeyer, O.M. Akoner, D.P. Ferris, and K.E. Gordon. Slacking by the human motor system: Computational models and implications for robotic orthoses. In Engineering in Medicine and Biology Society, 2009. EMBC 2009. Annual International Conference of the IEEE, pages 2129 –2132, sept. 2009.

[132] E.T. Wolbrecht, V. Chan, D.J. Reinkensmeyer, and J.E. Bobrow. Optimizing compliant, model-based robotic assistance to promote neurorehabilitation. Neural Systems and Rehabilitation Engineering, IEEE Transactions on, 16(3):286 –297, june 2008.

[133] Lorenzo Masia, Maura Casadio, Psiche Giannoni, Giulio Sandini, and Pietro Morasso. Performance adaptive training control strategy for recovering wrist movements in stroke patients: a preliminary, feasibility study. Journal of NeuroEngineering and Rehabilitation, 6:44+, December 2009.

[134] Elena Vergaro, Maura Casadio, Valentina Squeri, Psiche Giannoni, Pietro Morasso, and Vittorio Sanguineti. Self-adaptive robot training of stroke survivors for continuous tracking movements. Journal of neuroengineering and rehabilitation, 7:13+, March 2010.

[135] Javier Moreno and Rafael Kelly. On manipulator control via velocity fields. In Proc. of the 15th IFAC World Congress, Barcelona, Spain, July 2002.

[136] I. Cervantes, R. Kelly, J. Alvarez-Ramirez, and J. Moreno. A robust velocity field control. Control Systems Technology, IEEE Transactions on, 10(6):888 – 894, November 2002.

[137] Ming-Yang Cheng and Ying-Hui Wang. Velocity field construction for contour following tasks represented in nurbs form. Automatic Control, IEEE Transactions on, 54(10):2405 –2410, 2009.

[138] V. Patoglu and R. B. Gillespie. Extremal distance maintenance for parametric curves and surfaces. In Proc. 2002 IEEE International Conference on Robotics and Automation, pages 2817–2823, 2002.

[139] V. Patoglu and R. B. Gillespie. Haptic rendering of parametric surfaces using a feedback stabilized extremal distance tracking algorithm. In Proc. IEEE International Conference on Haptic Interfaces for Virtual Environment and Teleoperator Systems, volume 3, pages 391 – 399, 2004.

[140] V. Patoglu and R. B. Gillespie. Feedback stabilized minimum distance maintenance for convex parametric surfaces. IEEE Transactions on Robotics, 21(5):1009– 1016, 2005.

[141] M. C. Lin and J. F. Canny. A fast algorithm for incremental distance calculation. In IEEE International Conference on Robotics and Automation, pages 1008–14. Sacramento, California, 1991.

[142] B. Mirtich. V-Clip: Fast and robust polyhedral collision detection. ACM Transactions on Graphics, 17(3):177–208, 1998.

[143] K.S. Lashley. The problem of cerebral organization in vision. Biological Symposia, 7:301–322, 1942.

[144] Tamar Flash and Neville Hogans. The coordination of arm movements: An experimentally confirmed mathematical model. Journal of neuroscience, 5:1688–1703, 1985.

[145] Shay Ben-Itzhak and Amir Karniel. Minimum acceleration criterion with constraints implies bang-bang control as an underlying principle for optimal trajectories of arm reaching movements. Neural Comput., 20:779–812, March 2008.

[146] K.J. Wisneski and M.J. Johnson. Trajectory planning for functional wrist movements in an adl-oriented, robot-assisted therapy environment. In Robotics and Automation, 2007 IEEE International Conference on, pages 3365 –3370, april 2007.

[147] D. H. Sha, James L. Patton, and Ferdinando A. Mussa-Ivaldi. Minimum jerk reaching movements of human arm with mechanical constraints at endpoint. Int. J. Comput. Syst. Signal, 7(1):41–, 2006.

[148] Brandon Rohrer, Susan Fasoli, Hermano Igo Krebs, Richard Hughes, Bruce Volpe, Walter R. Frontera, Joel Stein, and Neville Hogan. Movement smoothness changes during stroke recovery. J Neurosci, 22:8297–8304, 2002.

[149] E Nakano, H Imamizu, R Osu, Y Uno, H Gomi, T Yoshioka, and M Kawato. Quantitative examinations of internal representations for arm trajectory planning: minimum commanded torque change model. Journal of Neurophysiology, 81(5):2140–2155, 1999.

[150] Daniel M. Wolpert, Zoubin Ghahramani, and Michael I. Jordan. Are arm trajectories planned in kinematic or dynamic coordinates? an

adaptation study. Experimental Brain Research, 103:460–470, 1995. 10.1007/BF00241505.

[151] Christopher M. Harris and Daniel M. Wolpert. Signal-dependent noise determines motor planning. Nature, 394(6695):780–784, August 1998.

[152] Mikhail Svinin and Motoji Yamamoto. A mathematical analysis of the minimum variance model of human-like reaching movements. In Intelligent Robots and Systems (IROS), 2011 IEEE/RSJ International Conference on, pages 4386 –4391, sept. 2011.

[153] Emanuel Todorov. Cosine tuning minimizes motor errors. Neural Comput., 14:1233–1260, June 2002.

[154] M. Haruno and D.M Wolpert. Optimal control of redundant muscles in step-tracking wrist movements. Journal of Neurophysiology, 94:4244–4255, December 2005.

[155] Todorov and M Jordan. Optimal feedback control as a theory of motor coordination. Nat Neurosci, pages 1226 – 1235, 2002.

[156] Stefan Schaal, Dagmar Sternad, Rieko Osu, and Mitsuo Kawato. Rhythmic arm movement is not discrete. Nature Neuroscience, 7(10):1137–1145, October 2004.

[157] Francesco Lacquaniti, Carlo Terzuolo, and Paolo Viviani. The law relating the kinematic and figural aspects of drawing movements. Acta Psychologica, 54(1-3):115–130, October 1983.

[158] S Schaal and D Sternad. Origins and violations of the 2/3 power law in rhythmic three-dimensional arm movements. Experimental Brain Research, 136(1):60–72, 2001.

[159] Renaud Ronsse, Dagmar Sternad, and Philippe Lefèvre. A computational model for rhythmic and discrete movements in uni- and bimanual coordination. Neural Computation, 21(5):1335–1370, 2009.

[160] P. Dizio and J. R. Lackner. Motor adaptation to Coriolis force perturbations of reaching movements: Endpoint but not trajectory adaptation transfers to the non-exposed arm. Journal of Neurophysiology, 74(4):1787–1792, 1995.

[161] J Randall Flanagan, Philipp Vetter, Roland S Johansson, and Daniel M Wolpert. Prediction precedes control in motor learning. Current Biology, 13(2):146–150, 2003.

[162] Reza Shadmehr and O A. Mussa-ivaldi. Adaptive representation of dynamics during learning of a motor task. Journal of Neuroscience, 14:3208–3224, 1994.

[163] Jonathan B. Dingwell, Christopher D. Mah, O A. Mussa-ivaldi, J Neurophysiol, K. M. Mosier, R. A. Scheidt, S. Acosta, F. A. Mussa-ivaldi, T. D. Sanger, J. B. Dingwell, C. D. Mah, F. A. Mussa-ivaldi, J Neurophysiol, C. D. Mah, F. A. Mussa-ivaldi, Jonathan B. Dingwell, Christopher D. Mah, Ferdinando, and A. Mussa-ivaldi. Manipulating objects with internal degrees of freedom: Evidence for model-based control. The Journal of Neurophysiology, 88:222–235, 2002.

[164] Jonathan B. Dingwell, Christopher D. Mah, O A. Mussa-ivaldi, K. A. Thoroughman, W. Wang, D. N. Tomov, J Neurophysiol, K. A. Thor-

oughman, J Neurophysiol, Jonathan B. Dingwell, Christopher D. Mah, and O A. Mussa-ivaldi. Experimentally confirmed mathematical model for human control of a non-rigid object, 2003.

[165] M. Svinin, I. Goncharenko, Zhi-Wei Luo, and S. Hosoe. Reaching movements in dynamic environments: how do we move flexible objects? Robotics, IEEE Transactions on, 22(4):724 –739, aug. 2006.

[166] Shigeyuki Hosoe Igor Goncharenko, Mikhail Svinin and Sven Forstmann. On the influence of hand dynamics on motion planning of reaching movements in haptic environments. Advances in Haptics, InTech, 2010.

[167] Ahmetcan Erdogan, Ali Israr, Marcia K. O'Malley, and Volkan Patoglu. Rate of human motor adaptation under varying system dynamics. In IEEE World Haptics Conference (WHC2011), 2011.

[168] F. Huang, R.B. Gillespie, and A. Kuo. Haptic feedback and human performance in a dynamic task. In Haptic Interfaces for Virtual Environment and Teleoperator Systems, 2002. HAPTICS 2002. Proceedings. 10th Symposium on, pages 24 –31, 2002.

[169] Jonathan B. Dingwell, Christopher D. Mah, and Ferdinando A. Mussa-Ivaldi. Experimentally Confirmed Mathematical Model for Human Control of a Non-Rigid Object. Journal of Neurophysiology, 91(3):1158–1170, 2004.

[170] A. Israr, H. Kapson, V. Patoglu, and M.K. O'Malley. Effects of magnitude and phase cues on human motor adaptation. In EuroHaptics conference, 2009 and Symposium on Haptic Interfaces for Virtual

Environment and Teleoperator Systems. World Haptics 2009. Third Joint, pages 344 –349, March 2009.

[171] Ali Israr, Yanfang Li, Volkan Patoglu, and Marcia K. O'Malley. Passive and active discrimination of natural frequency of virtual dynamic systems. IEEE Transactions on Haptics, 2:40–51, 2009.

[172] Nikhil Bhushan and Reza Shadmehr. Computational nature of human adaptive control during learning of reaching movements in force fields. Biological Cybernetics, 81(1):39–60, 1999.

[173] Robert A. Scheidt, David J. Reinkensmeyer, Michael A. Conditt, W. Zev Rymer, and Ferdinando A. Mussa-Ivaldi. Persistence of motor adaptation during constrained, multi-joint, arm movements. Journal of Neurophysiology, 84(2):853–862, 2000.

[174] E.J. Lai, A.J. Hodgson, and T.E. Milner. Influence of interaction force levels on degree of motor adaptation in a stable dynamic force field. Experimental Brain Research, 153(1):76–83, 2003.

[175] Felix C. Huang, R. Brent Gillespie, and Arthur D. Kuo. Visual and haptic feedback contribute to tuning and online control during object manipulation. Journal of Motor Behavior, 39(3):179 – 193, 2007.

[176] David W. Franklin, Etienne Burdet, Keng Peng Tee, Rieko Osu, Chee-Meng Chew, Theodore E. Milner, and Mitsuo Kawato. Cns learns stable, accurate, and efficient movements using a simple algorithm. The Journal of Neuroscience, 28(44):11165–11173, 2008.

[177] Arne J. Nagengast, Daniel A. Braun, and Daniel M. Wolpert. Optimal control predicts human performance on objects with internal degrees of freedom. PLoS Comput Biol, 5(6):e1000419, 06 2009.